Single-channel physiology in small compartments

Madeleine R. Howell 03-17-2026

Copyright © [*2026*] [*Madeleine R. Howell*] All rights reserved.

Dissertation Advisor: Prof. Adam E. Cohen Madeleine R. Howell

Single-channel physiology in small compartments

Cellular membranes are replete with integral transport proteins which regulate key processes from biochemical and electrical signaling to osmotic homeostasis. Bulk transport measurements obscure kinetic details due to ensemble averaging. Fluorescent reporters of ions and small molecules provide sensitive readouts of solute concentrations but rapid diffusion and clearance of solute fluxes in the bulk limits the scope of transporters which can be measured. In this dissertation, we use experiment and theory to explore how small membrane-derived compartments can be leveraged for highly sensitive *in cellulo* transport measurements and distinct electrophysiology of native nanoscale structures.

Native densities of membrane transport proteins (e.g. ion channels, transporters, pumps) in a neuron vary by ~four orders of magnitude. Transport rates through integral proteins (e.g. solute molecules s^{-1}) vary by ~nine orders of magnitude. It follows that there exist membrane area and lumen volume regimes where transporter numbers are small and single-unit flux alters lumenal solute concentrations. In fact, biology is replete with nanoscopic structures including thin filopodia (area ~10 μm^2, volume ~1.5 fL), dendritic spines (~1 μm^2, ~0.1 fL), the primary cilium (~2.5 μm^2, ~0.1 fL), and synaptic vesicles (~5×10^{-3} μm^2, ~30 zL). Membrane compartments of similar scales can be created in living cells on-demand using physical (e.g. micromanipulation) and optogenetic tools. The electrophysiology of native and membrane-derived compartments is accessible using advanced optogenetic techniques to measure electrolyte and voltage dynamics.

In Chapter Two we leverage membrane tethers – tubes of membrane extracted from cells – for optical recordings of Ca^{2+} flux through single voltage-gated Ca^{2+} channels. Tethers are a facile means of isolating individual channels from the bulk membrane. Tether radii are subdiffraction-sized such that Ca^{2+} transported into the tether lumen remains within the microscope focus. Ca^{2+} transported into the lumen is isolated from bulk membrane transport because the quasi-1D tether geometry restricts diffusion of transported solute. Despite low channel conductance (<2 pS) and estimates of high lumenal Ca^{2+} buffering, membrane tethers enabled the detection of single-channel Ca^{2+} transport via a genetically encoded Ca^{2+} indicator. Comparison of event statistics to stochastic single-channel simulations suggest that tether Ca^{2+} indicators are sensitive to as little as ~0.4 fC or ~1250 transported Ca^{2+} ions. This

corresponds to as few as 6-13 free Ca^{2+} ions under typical buffering conditions. In Chapter Four we discuss how tether-based transport measurements might generalize to other integral proteins and solutes.

In membrane tethers, single-channel gating measurably perturbs lumenal ionic concentrations but voltage remains well clamped by the cell body. However, many nanoscopic structures (e.g. synaptic vesicles, dendritic spines, endocytic vesicles, and microbes) are electrically and biochemically isolated. In Chapter Three we use stochastic single-channel and ensemble simulations in model membranes to identify compartment size and channel density regimes in which membrane noise becomes a dominant driver of membrane voltage and lumenal electrolyte fluctuations. Within these regimes, we explore the qualitatively distinct dynamics which emerge when voltage and electrolyte fluctuations feedback onto voltage-dependent channel gating. We identify regimes which alter effective voltage-gated channel kinetics and produce patterns of single-channel and ensemble channel activity which cannot be described using deterministic conductance-based models. We provide several predictions for nanoscale electrophysiology which are experimentally testable using the tools of optical electrophysiology.

Nanoscale structures support patterns of electrical activity which differ substantially from the electrophysiology of large cells. The experimental and computational work described herein provides a glimpse into how nanoscale electrophysiology can be leveraged for sensitive studies of membrane transport and interpreted in native contexts.

Table of Contents

Acknowledgements

Many people have been instrumental in helping me do the work described in the following pages. First, I want to express my sincere gratitude to my PhD advisor, Prof. Adam E. Cohen. I started in the lab fresh from my Chemistry undergrad with a bit of engineering experience and I've come out the other side a (sort of) biophysicist. I have learned so much from your physics intuition, technical expertise, and scientific outlook. Thank you for always keeping a pen and paper handy to teach me a concept or sketch out an idea. Thank you for letting me "steal" these pages to study afterwards – they would no doubt fill a book longer than this dissertation. Thank you for your kind mentorship, patience, and guidance over the past 5 and ½ years.

I want to express my gratitude to my committee members, Prof. Rachelle Gaudet and Prof. Xiaowei Zhuang for their helpful feedback and scientific insights over the years.

I would like to thank the Department for providing the organizational and facilities support to do this work. Special thanks to Josh Cox, Kathy Oakley and Joe Lavin for making sure I remained sane, in good academic standing, and funded throughout my PhD. Thank you to the NSF GRFP for financial support.

To my labmates, many of whom are also my friends, thank you for making the lab a fun and intellectually stimulating place to learn and do research. Our office banter, hallway conversations, afternoon runs, and volleyball games were a great place to discuss new ideas, get help on experiments or data analysis, or just chat. Extra special thanks go to all the incredible people – past and present – who keep the lab running – Shahin, Maggie, Hillary, Elsa, Camila, Megan, and Andrew. Thank you for your organizational (and occasionally emotional) support.

To my friends, especially Kristen, Nicole, and Griffin, thank you for helping me to lead a fun, supported, and adventure-filled life outside of the lab. I am so grateful to have met you all here. In spite of my initial misgivings about the city, you've made Cambridge a really special place.

To my family (that includes you, Tyler), I could not have done this without your love and support. Special thanks to my Aunt Sue and the Uvannis for their hospitality over many impromptu visits to Pittsburgh, PA and Rome, NY.

To my husband, Trevor, even though you were six hundred miles away for most of my PhD it was like you never left my side. Thank you for seeing me through it all.

To my family.

List of Figures

List of Tables

1 Introduction

Membranes are not passive barriers. They are replete with integral proteins (i.e. channels, transporters, and receptors) which regulate the flow of information – ions, small molecules, peptides, etc. – between luminal and extraluminal spaces. Integral proteins are key players in electrical and biochemical signaling pathways. Upon binding of a ligand, substrate, or a change in the electric field across the membrane, integral proteins can passively or actively transport ions and small molecules. These transmembrane flows control osmotic balance, excitability, and biochemical signaling networks.

Much of our understanding about the dynamics of integral proteins come from biochemical assays which measure flux through all the proteins in a membrane simultaneously (i.e. the “roar of the crowd”). However, much work suggests that integral proteins behave stochastically: ion channels flicker open and close, enzymatic turnover times vary, and transporters interconvert between kinetic modes. Stochasticity in integral proteins dominate membrane dynamics as system size shrinks.

Nanoscopic membrane-bound structures are ubiquitous in biology and include dendritic spines, filopodia, endocytic vesicles, primary cilia, synaptic vesicles, tunneling nanotubes, and small diameter neurites and asperities. Furthermore, typical densities of integral proteins span roughly four orders of magnitude[1–3]. Thus, there are compartment size and density regimes which result in only a few copies of a given integral protein per compartment[4,5]. How does stochasticity in membrane transport affect the physiology of nanoscopic structures? Conversely, can such structures be leveraged for single-molecule resolved flux measurements?

We answer these questions through a combination of experimental and theoretical studies. First, we explore experimentally how membrane tubes extracted from intact cells can be leveraged for fluorescence detection of small single-channel fluxes. Then, we explore computationally the distinct electrophysiological dynamics which emerge in small membrane compartments due to their labile membrane voltage and ionic gradients. This introductory chapter provides the reader with background regarding (1) the statistical origins and physiological effects of membrane noise, and (2) electrophysiological and optical tools to measure transmembrane flux. Chapter Two discusses our use of membrane-derived tethers to measure Ca^{2+} flux through single voltage-gated Ca^{2+} channels in intact cells. Chapter Three discusses our computational work towards modeling electrophysiology in nanoscale

compartments. Chapter Four summarizes this body of work and its utility to the fields of electrophysiology, membrane biology, and organelle physiology.

This work presents a new method for measuring single-channel dynamics and a theoretical framework for interpreting and predicting the role of such fluctuations in the electrophysiology of small compartments.

1.1 Membrane noise

The permeability of cellular membranes to electrolytes and small molecules is controlled by the dynamics of the channels, pumps, and transporters they express. Historically, only population average dynamics have been experimentally accessible. Bulk biochemical methods (e.g. analyte sensitive dyes or radiometric uptake of substrates) and whole-cell electrophysiology average the dynamics of many transport proteins within an ensemble and across time[6,7]. Ensemble-averaged measurements are useful for coarse-grained models of transport (e.g. Hodgkin-Huxley-type kinetic descriptions of whole-cell currents) but have limited utility for generating mechanistic models (e.g. Markov model of channel microstates). This is especially true when the transporter ensemble contains rare subpopulations that exhibit stationary differences in dynamics (perhaps from alternative splicing or posttranslational modifications) or dynamic rate disorder (e.g. mode-switching from slow conformational fluctuations)[8–10]. Single-molecule-resolved measurements of protein dynamics (e.g. flux, catalysis, conformation, etc.) can provide unambiguous insight into protein microstates and kinetics. Recent single-molecule-resolved measurements suggest that static and dynamic disorder may be a general feature of ion channels, transporters and pumps[10,11]. In addition to providing physiological insights, single-molecule measurements can help uncover the mechanisms of protein dysfunction in disease and identify new means of pharmacological regulation[7,12].

Single-molecule dynamics are useful to the experimenter seeking mechanistic insights, but do downstream systems “hear” the roar of the crowd or individual proteins? Here, we discuss recent work which identifies several biological systems and size regimes where the dynamics of individual proteins dominate behavior. Consider a membrane which contains *N* independent, identical ion channels. The relative contribution of channel noise scales ~ $1/\sqrt{N}$. This scaling holds for many molecular processes with Poissonian statistics (i.e. channel on/off, enzyme with substrate bound/unbound, transporter outward

facing/inward facing). It follows that single-molecule effects become important as system size (*N*) shrinks. Thus, transport via individual membrane proteins dominates membrane flux as membrane area or transporter number decreases. Small compartments, including synaptic vesicles, lysosomes, and dendritic spines are known to contain low copy numbers of ion channels (1-20 voltage-gated Ca^{2+} channels/spine) and electrogenic pumps (~1.3 v-ATPase/synaptic vesicle and ~3-50 v-ATPase/lysosome) [13–15].

From an electrophysiological perspective, current noise can have global effects when it drives substantial voltage noise. Recent work shows that lysosomes and dendritic spines can undergo large changes in voltage in response to small current inputs [15,16]. For example, patch-clamp recordings in isolated lysosomes show large (~ -15 mV) and rapid (~ 10 ms) deflections in membrane potential upon opening of single Ca^{2+} activated K^+ channels [16]. This effect is not limited to nanoscopic compartments – patch-clamp recordings in small hippocampal neurons with high (GΩ) input resistance show that single-channel currents can be highly effective at recruiting other channels to produce an action potential[17]. Current noise is expected to cause substantial voltage fluctuations when passive membrane leaks and capacitance are low. From a biochemical perspective, membrane noise can substantially change concentration gradients of electrolytes and small molecules when volumes (either internal or external) are small and restorative mechanisms (e.g. active or passive extrusion, buffering, and diffusion) are slow. For example, in dendritic spines, Ca^{2+} influx through only a single $NMDA_R$ can lead to an ~10-fold change in free spine Ca^{2+}.[18] Proteomic profiling suggest that sensory cilia remain robust to concentration noise is by maintaining ~1000-fold abundance of effector proteins over their soluble substrates as well as fast substrate buffering and extrusion systems.[19]

Our work in Chapter Two uses membrane tethers to create a system in which single-channel currents dominate local membrane conductance and local electrolyte concentrations; enabling single-unit detection while preventing substantial voltage changes via electrical coupling to the cell body. Our work in Chapter Three explores the effects of removing this voltage clamp – allowing membrane current noise to feed through to voltage noise – and the ensuing self-action of voltage and electrolyte gradients on compartment electrophysiology.

1.2 Existing tools

A fundamental challenge in single-molecule resolved measurements is overcoming background signals. In electrophysiological measurements, these could be neighboring ion channels in a patch, a leaky seal, or head-stage electronics, among other sources[20]. Small electrode diameters and high-resistance seals physically and electrically isolate single channels[21]. In optical single-molecule measurements (i.e. fluorescence correlation spectroscopy (FCS[22]), single-molecule FRET (smFRET[23]), single-particle tracking (SPT), or single-molecule localization microscopy (SMLM[24])), background may consist of out of focus fluorescent molecules, or sample and substrate autofluorescence. Single-molecule techniques achieve background suppression in several ways. These include (1) sculpting of excitation volumes using total internal reflectance (TIRF) or confocal optics (2) turn-on of fluorescence from a subset of molecules at a time[24–26] (3) physical isolation in small volumes (i.e. trapping[27], nanoscopic wells[28,29], lipid vesicles[10–12,30], or otherwise tight spaces[31]). Or, choice of a system which *only contains* several copies of the proteins of interest (see transcription machinery of *S. cerevisiae* and *E. coli*[32]).

Of the above single-molecule techniques, single-channel electrophysiology is the most mature technique for measuring *current* flux through membranes. Since its development by Hamill and colleagues in 1981[33], single-channel recording has yielded a wealth of information about ligand- and voltage-gated ion channel dynamics which have shaped our understanding of electrical signaling in brain, heart, muscle, pancreas and other excitable systems[34]. Single-channel records can be made in a cell-attached or excised patch configuration both in plasma membrane and internal membranes of isolated organelles. Despite its utility, single-channel recording has its limitations. First, it is only applicable to channels with a net current of a detectable magnitude. But many integral membrane proteins (e.g. chloride and glucose transporters)[35,36] generate no net current or their transport rates are too slow (e.g. glutamate transporters transport 1-100 molecule/s)[37] to be detectable with single-channel patch. Noise in the seal and amplifier electronics limit the sensitivity of single channel patch to ~100 fA for brief channel openings (~500 μs)[20].

Alternatively, transmembrane flux of small molecules and ions can be detected using fluorescent reporters[38]. Fluorescent biosensors are available in many scaffolds, including synthetic dyes[39–41], proteins[42–46], and hybrid chemigenetic sensors[47–49]. Detectable analytes include, but are not limited to:

electrolytes (i.e. Ca^{2+}, Cl^{-}, Na^{+}, K^{+}, Mg^{2+}, Zn^{2+}, H^{+}), energy substrates (i.e. glucose, pyruvate, lactate, aspartate), neurotransmitters (acetylcholine, glutamate, dopamine, γ-aminobutyric acid, serotonin) and neuropeptides[38,50]. Genetically encoded biosensors have the advantage of being targetable to a specific cell type or subcellular location. The general scheme of many genetically encoded biosensors for ions and small molecules consist of a fluorescent protein fused to an analyte binding domain (e.g. CaM and M13 CaM-binding peptide in GCaMP). Binding of analyte induces a conformational change in the scaffold which directly (e.g. via change in chromophore environment)[51], or indirectly (i.e. via FRET)[52] modulates sensor fluorescence. Sensor fluorescence depends on the concentration of the analyte. The scaling of relative sensor fluorescence with analyte concentration is characterized by the sensor dynamic range, cooperativity (steepness of the binding curve), and binding affinity[53]. Many biosensors exhibit fluorescence which is nonlinear in analyte concentration. Recent efforts in the design and use of fluorescent sensors (both of chemical analytes discussed above, but also physical quantities such as voltage and mechanical loading rate) have yielded methods for absolute measurement of such quantities (i.e. calibrated signals in mM[54–59], mV[49,60,61], pN/s[62]). The following discussion details the use of fluorescent sensors in measuring flux through single molecules and in small compartments.

In proteoliposome-based single molecule recordings, a fluorescent sensor is encapsulated in a nanoscopic ($r \sim 50$ nm) lipid vesicle and a stoichiometry of one transmembrane protein (e.g. transporter or pump):vesicle is attained. The small volume of the vesicle concentrates the transported analyte, rendering even single substrate translocation events detectable by moderate affinity fluorescent sensors[10]. Further, proteoliposomes can be immobilized and arrayed on glass slides, enabling massively parallel measurements. This approach has been used to dissect the transport properties of primary transporters including glutamate transporters[10,63], cystic fibrosis transmembrane conductance regulator (CFTR)[12], H^{+}-ATPases[11] and Ca^{2+}-ATPases[30]. Transport measurements can be performed in parallel with FRET reporter labeling of key protein residues to visualize protein conformational rearrangements as they relate to translocation of substrate[64]. This powerful approach has several drawbacks; as in any reconstituted system, artifacts may be introduced under *in vitro* conditions that are difficult to control or account for (i.e. membrane tension induced by high curvature alters gating[65,66]; lack of regulatory systems including scaffolding and accessory proteins, etc.). Furthermore, clamping voltage and electrolyte

concentrations in submicron-sized vesicles is difficult and imprecise, requiring perturbations that alter native membrane permeability and/or lumenal buffering[11,30]. The consequences of a lack of voltage or concentration-clamp in small compartments are explored in Chapter Three, where we simulate the effects of rapidly changing voltage and concentration dynamics on individual and small ensembles of ion channels.

One of the key advantages of encapsulation-based approaches is that they restrict the diffusion of translocated substrate, raising its concentration into a regime detectable by fluorescent sensors. In Chapter Two we analyze the diffusion of transported molecules away from a source (e.g. channel) in a cell body. We show that steady-state substrate concentrations (assuming free diffusion) are reached quickly ~r^2 and decay sharply ~$1/r$ with distance, r, from the source. This imposes severe limitations on fluorescent reporter-based detection in intact cells: sensor must (1) have a high substrate affinity, (2) rapidly bind substrate, and (3) have excellent quantum yield[67]. Furthermore, background from out-of-focus or spatially overlapping events, or diffusion of signal from prior events, typically necessitates the use of optical sectioning techniques and sparse expression of transporter[68–71]. One strategy to enhance sensitivity and diminish substrate diffusion artifacts is to directly tether the sensor to the source. This has been implemented for optical single-channel flux measurements of N-type Ca^{2+} channels[72], Orai1[73], and Piezo1[74]. Notably, this constrains sensor design further – sensors must be sufficiently bright to render the detection of single sensor molecules feasible. In circumstances where unitary currents are large, single-channel detection is feasible even without tethering the sensor to the source. Much work from the Parker lab and others have made use of high-affinity and fast chemical and genetically-encoded Ca^{2+} sensors to record unitary events in plasma and endomembrane Ca^{2+} channels[67–69,75–77]. These approaches enable spatially-resolved recording of single-channel dynamics but offer minimal gain in sensitivity beyond patch-clamp.

In Chapter Two we build upon this prior work and apply the principles of single-molecule fluorescence techniques towards the development of tether-based optical single-channel recording in intact cells. We benchmark this technique using a recently developed Ca^{2+} sensor to detect unitary events from a low-conductance Ca^{2+} channel. In Chapter Three we show that tight coupling between single-channel currents and membrane voltage feedback onto channel behavior in small compartments – a finding that is

directly relevant to the interpretation of proteoliposome-based single-molecule measurements. This work highlights nonclassical phenomenon in small compartments which we expect to be experimentally tested with new classes of optical tools.

2 Optical single-channel recording via diffusional confinement in membrane tethers

2.1 Abstract

Single-channel electrophysiology probes ion channel gating, but how can one probe membrane transport when the single-unit current is undetectable? We pulled membrane tethers from live cells to isolate individual transmembrane proteins. The tether constrained diffusion of transported substrate to the tether axis, leading to ~1000-fold enhancement of substrate concentration and observation time compared to planar membranes. Fluorescent reporters inside the tether revealed individual transport events. We imaged unitary Ca^{2+} transport events in tethers containing the low-conductance T-type Ca^{2+} channel $Ca_V3.2$, and compared our results to ensemble electrophysiology and stochastic gating simulations. We detected events corresponding to as little as ~0.4 fC of transported charge, or only 6 – 13 free Ca^{2+} ions under typical buffering conditions. Tether-based single-channel recordings are a powerful tool to study dynamics of membrane transport.

Keywords: Single-molecule, Membrane Transport, Fluorescent Sensors, Signal Confinement, Live-cell Imaging

2.2 Introduction

The plasma membrane of eukaryotic cells is decorated by diverse ion channels, transporters, and membrane-associated enzymes which orchestrate electrical and chemical signaling, osmotic regulation, and aspects of metabolism.[7,78,79] The transport properties of these proteins are critical to their function. Single-channel electrophysiology[21,34,80,81] can reveal molecular mechanisms of ion channel gating and regulation, but many channels and transporters remain inaccessible to this technique because either they are not electrogenic, or the single-unit current is too small (< ~100 fA).[20,82]

Optical recordings of transmembrane flux using fluorescent reporters[38] can also probe single-channel transport. Optical recordings have measured Ca^{2+} flux through single voltage- and ligand-gated channels, using either fluorogenic Ca^{2+} dyes or a genetically-encoded Ca^{2+} indicator (GECI) tethered to the channel.[68–71,73,74,76,83] However, rapid dilution of transported ions into the cytoplasm limits the sensitivity of this approach. Isolation of single transporters in purified nanoscale proteoliposomes achieves single-channel sensitivity by preventing diffusive dilution of transported molecules.[10,63] However, this cell-free approach requires protein purification, loses the native cellular context, and restricts molecular or electrical access to the lumen of the liposomes.

Membrane tethers consist of thin (typically ~100 nm diameter) tubes of membrane which can be pulled from many cell types in culture.[84] The tether lumen remains in diffusive interchange with the cell body, while the tether membrane restricts diffusion along the two orthogonal axes. Thus, tethers are intermediate between intact cell membrane and purified proteoliposomes: they provide substantial diffusive confinement but retain much of the physiological context and provide molecular and electrical access to the lumen.

Here, we pulled membrane tethers from intact cells and used a fluorescent reporter to record single-molecule gating events within the tether (**Figure 2.1 A, B**). We recorded single-channel events from $Ca_V3.2$, a low-conductance (< 2 pS) and transiently activated voltage gated calcium channel (VGCC),[85,86] using a membrane-targeted genetically encoded calcium indicator (GECI).[42,87] Voltage-clamp in the parent cell controlled the gating of single channels. We related the single-channel gating properties to ensemble $Ca_V3.2$ currents, and used stochastic gating simulations to interpret our results.

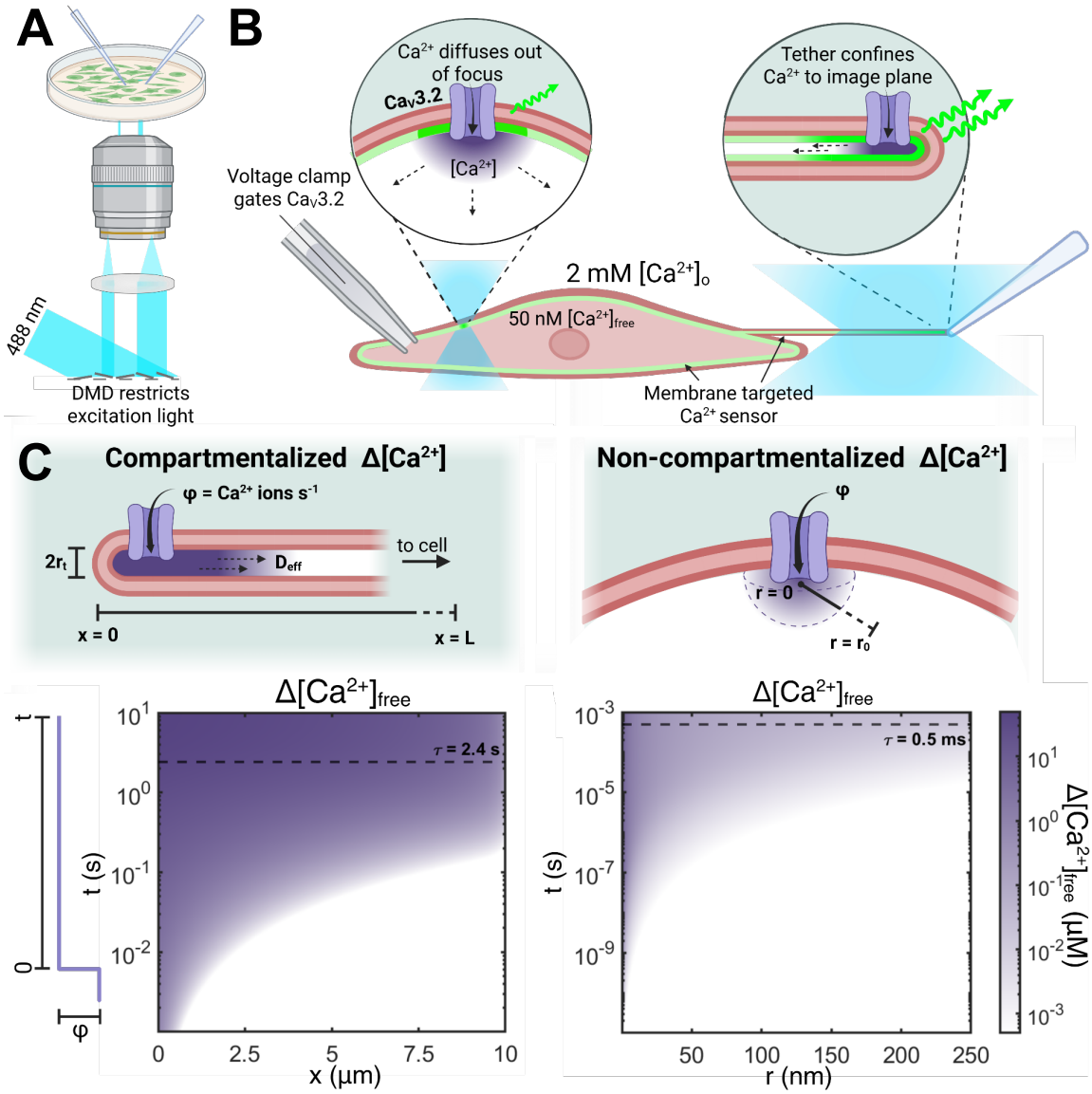

Figure 2.1 Single-channel recording in membrane tethers.
A. Experimental setup comprising patterned illumination from a digital micromirror device (DMD) and two pipettes controlled by micromanipulators. **B.** Schematic of the experiment. A HEK293 cell expressed $Ca_V3.2$ and a membrane-targeted Ca^{2+} indicator. One pipette applied voltage steps to gate the Ca_V channels. A second pipette pulled a membrane tether, which confined the Ca^{2+} influx from single Ca_V gating events. DMD-targeted illumination of the tether minimized background fluorescence and flare from the much brighter cell. **C.** Comparison of $Ca_V3.2$ channel residing in a tether (left) or the cell body (right). Bottom: simulated Ca^{2+} profiles for the depicted geometries, assuming a step opening of the channel at t = 0, a transport rate $\phi = 10^5$ Ca^{2+} ions/s,[86] an effective diffusion coefficient D_{eff} = 21 mm²/s,[88–90] and a buffering capacity (buffer-bound Ca^{2+} per free Ca^{2+})[18] κ = 200.[67,89] In the tether, the channel is assumed to reside at the distal end. For the channel in the cell body, the Ca^{2+} concentration is averaged over a hemisphere of radius r. Dashed lines indicate the Ca^{2+} residence time in a tether-delimited (left) and diffraction-limited (right) focal volume. See **Table A.2** for diffusion model parameters.

2.3 Results and Discussion

2.3.1 Theory of single-channel signal enhancement in membrane tethers

We first modeled Ca^{2+} transport for a single channel residing either within a tether or on the cell body membrane. Details of the model are in Appendix A.1 and **Table A.1**[18,67,88–90] We modeled the tether as a tube of radius r_t and length L, open to the cell body at its proximal end and sealed at its distal end (**Figure 2.1 C**). Tether radii were r_t ~ 50 nm, set by the balance of membrane rigidity and membrane tension[91] (Fig. A1), and lengths were L ~ 10 μm. We assumed rapid equilibrium of cytoplasmic Ca^{2+} buffers such that free Ca^{2+} flux, ϕ_{free}, scales inversely with buffer capacity, κ_B, following $\phi_{\mathrm{free}} = \phi/(1+\kappa_B)$, where f is the total flux through the channel.[92] The effective Ca^{2+} diffusion coefficient, D_{eff}, is a weighted average of free and buffer-bound Ca^{2+} diffusion coefficients (Eq. A7 in Appendix A.2).[93] We compared the Ca^{2+} concentration within a membrane-delimited tether volume to the mean Ca^{2+} concentration within a diffraction-limited confocal volume with radius r_0, centered on a channel in the cell body membrane.

If a Ca^{2+} channel opens and stays open at the distal end of the tether, the steady-state free $[Ca^{2+}]$ concentration has maximal increase at the location of the channel:

$$\Delta[Ca^{2+}]_{free} = \frac{\phi L}{D_{eff}\pi r_t^2(1+\kappa_B)}, \qquad 2.1$$

and a linear decrease down to $\Delta[Ca^{2+}]_{free} = 0$ at the junction with the cell body. The mean residence time of a Ca^{2+} ion in the tether is:

$$\tau = \frac{L^2}{2D_{eff}}. \qquad 2.2$$

For a channel opening in the membrane on the cell body, we model the geometry as a planar membrane opening into an infinite half-space. This approximation is valid over distances much smaller than the size of the cell. In this scenario, Ca^{2+} rapidly diffuses into the open half-space (**Figure 2.1 C**). The steady state increase, $\Delta[\mathrm{Ca}^{2+}]_{\mathrm{free}}$, decays with distance r from the channel as $1/r$. We modeled the resulting Ca^{2+} domain as an average of $\Delta[\mathrm{Ca}^{2+}]_{\mathrm{free}}$ over a diffraction-limited focal volume with radius r_0 centered on the channel, so:

$$\langle\Delta[\mathrm{Ca}^{2+}]_{\mathrm{free}}\rangle = \frac{3\phi}{4\pi D_{\mathrm{eff}} r_0(1+\kappa_B)}. \qquad 2.3$$

The mean residence time of a Ca^{2+} ion within this observation volume is:

$$\tau = \frac{r_0^2}{6D_{eff}}. \quad 2.4$$

Our model predicts that a tether of typical dimensions (100 nm diameter, 10 μm long) enhances the steady-state in-focus $\Delta[Ca^{2+}]_{free}$ near the channel by a factor of $r_0 L / r_t^2$ ~10^3 compared with diffraction-limited imaging of a Ca^{2+} channel in the membrane of the cell body (**Figure 2.1 C**, Appendix A.1). The time-resolution with which channel gating converts to changes in $\Delta[Ca^{2+}]_{free}$ is ~10^3-fold slower in the tether than for the channel in the soma membrane. These simple estimates suggest that membrane tethers can render even miniscule steady-state transmembrane flows ($\phi_{free} = 100\ s^{-1}$, D_{eff} = 200 μm²/s) detectable by a fluorescent reporter (K_D ~ 1 μM).

Dimensional scaling arguments can also predict the fluorescence decay rates for transiently active channels or pores (Appendix A.1). After a brief influx of Ca^{2+}, in a tether, the local concentration around the influx site decays as $t^{-1/2}$. In a cell, the local concentration decays as $t^{-3/2}$. Thus, tethers provide a longer observation window for detecting brief channel-gating events.

2.3.2 Tether fluorescence reports membrane Ca^{2+} influx with high fidelity

We tested whether Ca^{2+} compartmentalization in tethers permitted optical recordings of single-channel gating. In a HEK293 cell line stably expressing doxycycline-inducible $Ca_V3.2$ α1 subunit,[94] we titrated doxycycline to achieve an expression density of ~4 channels/μm² (**Figure A.1**, Section 2.5 Methods). We also expressed a membrane-targeted GECI, either lck-jGCaMP8f or GCaMP6s-CAAX.[42,87] A high-efficiency transfection protocol and strong promotor (CMV) drove dense GECI expression, so the GECI molecules were effectively continuous along the tethers (**Figure A.1**, Section 2.5 Methods). We used a patch pipette in whole-cell mode to modulate the membrane voltage and to record ensemble Ca_V currents, and a second pipette to extract tethers. Due to the sub-diffraction tether diameter, GECI fluorescence from the tether membrane was far dimmer than from the cell body membrane (**Figure A.1**). To record from both regions, we used a digital micromirror device (DMD) to target 488 nm excitation light onto the tether and onto a small patch of the cell body opposite the junction with the tether (**Figure 2.2 A**). This illumination strategy minimized the total excitation light, decreasing background autofluorescence and flare from the bright fluorescence of the cell body, which might otherwise have overwhelmed the dim signal from the tether. The tethers were too thin to determine their diameter via direct imaging, so we compared GECI fluorescence from the tether and from a patch of the cell membrane of defined area,

using the constant GECI fluorescence per-unit-surface-area to determine the ratio of these two areas (**Figure A.1**). These measurements were performed at a holding potential of -80 mV, where Ca_V channel activation is negligible, to ensure the results were not distorted by Ca_V-mediated Ca^{2+} fluxes.

We applied trains of depolarizing voltage pulses from a holding potential of -80 mV, and simultaneously recorded whole-cell currents and GECI-reported Ca^{2+} dynamics in the cell, $(\Delta F/F)^C$, and tether, $(\Delta F/F)^t$ **Figure 2.2 B-C**). The camera frame-rate was 50-200 Hz. The voltage steps induced transient inward whole-cell currents which typically returned to zero before the end of the t_V = 45 ms voltage step (**Figure 2.3 A**). The time constants of $Ca_V3.2$ activation and inactivation decreased for more depolarizing voltages, consistent with prior studies of this channel.[85]

Membrane depolarization evoked Ca^{2+} signals in the cell and tether (**Figure 2.2 B-C**). Both regions also showed occasional spontaneous Ca^{2+} dynamics (**Figure 2.2 B** light shading). Epochs with these spontaneous events were omitted from analysis (Section 2.5 Methods). An estimate of tether electrotonic length-constant, λ, based on whole-cell membrane conductance and tether geometry, gave λ ~ 110 µm (membrane resistivity $R_{\mathrm{m}} = 1.5 \times 10^6\ \mathrm{M\Omega\ \mu m^2}$; intracellular resistivity $R_i = 3.0\ \mathrm{M\Omega\ \mu m}$;[95] radius $r = 50\ \mathrm{nm}$), indicating that Ca_V channels throughout the tether experienced membrane voltages similar to the voltage at the cell body. The appearance of voltage-gated Ca^{2+} influx in the tether was consistent with this finding.

For both cell body and tether, the stimulus-evoked GECI fluorescence grew and decayed slowly compared to the patch-clamp recorded currents (**Figure 2.2 C, Figure 2.3 B**). The upstroke of the GECI fluorescence was much faster (~10 ms) than the recovery (~1.4 s), implying that the peak GECI fluorescence was proportional to the increase in Ca^{2+} concentration due to the voltage step:

$$\max\left(\frac{\Delta \mathrm{F}}{\mathrm{F}}\right) \propto \frac{1}{\Gamma}\int_0^{\mathrm{tv}} I_{\mathrm{Ca}}\,\mathrm{dt}, \qquad 2.5$$

where G is the volume into which the Ca^{2+} is diluted and I_{Ca} is the absolute value of the inward Ca^{2+} current.

For each voltage step, we calculated whole-cell charge influx, $Q_{\mathrm{Ca}}^{\mathrm{C}}$, via the integral of the voltage-clamp current recording. We estimated the surface areas of the tether and of the whole cell from the tether geometry (**Figure A.1**) and the whole-cell capacitance, respectively (**Figure A.2**). We initially assumed that channel density was approximately homogeneous across the cell and the tether, so we

predicted that the Ca^{2+} flux would be apportioned between the cell (Q_{Ca}^{C}) and the tether (Q_{Ca}^{t}) according to their relative surface areas.

We then checked the proportionality across voltage steps between tether Ca^{2+} signal, $(\Delta F/F)^t$, and the predicted tether charge concentration, $[Q_{Ca}^{t}]$. We observed a clear linear relationship within each tether (**Figure 2.3 C, Figure A.3**), but substantial variation in slope between tethers (**Figure 2.3 C** inset). The differing slopes likely reflected variation in tether channel density, perhaps due to inhomogeneous channel distributions across the cell leading to variations in the number pulled into each tether. We also observed trial-to-trial fluctuations in fluorescence responses within each tether, which we attribute to statistical fluctuations in channel activation within tethers (**Figure 2.3 C** inset). These fluctuations are expected, considering the small number (~2 - 12) of stochastically gating channels per tether (**Figure A.2**).

Unexpectedly, we found that the correlation between $(\Delta F/F)^t$ and Q_{Ca}^{C} was stronger than the correlation between $(\Delta F/F)^C$ and Q_{Ca}^{C} (**Figure 2.3 D**, **Figure A.3**), i.e. whole-cell charge and whole-cell fluorescence-reported Ca^{2+} influx were not well correlated. We speculate that the Ca^{2+} in the cell body may have had additional stochastic uptake and release from internal Ca^{2+} stores (e.g. in mitochondria and endoplasmic reticulum), whereas these organelles were excluded from the tether. Future experiments could explore this issue via pharmacological modulation of internal Ca^{2+} stores. Since we could not establish a robust relationship between Ca^{2+} influx, Ca^{2+} concentration, and GECI fluorescence in the cell body, we were unable to establish an absolute relation between $(\Delta F/F)^t$ and Q_{Ca}^{t}. Hence, subsequent measurements focused on analyzing relative changes in $(\Delta F/F)^t$.

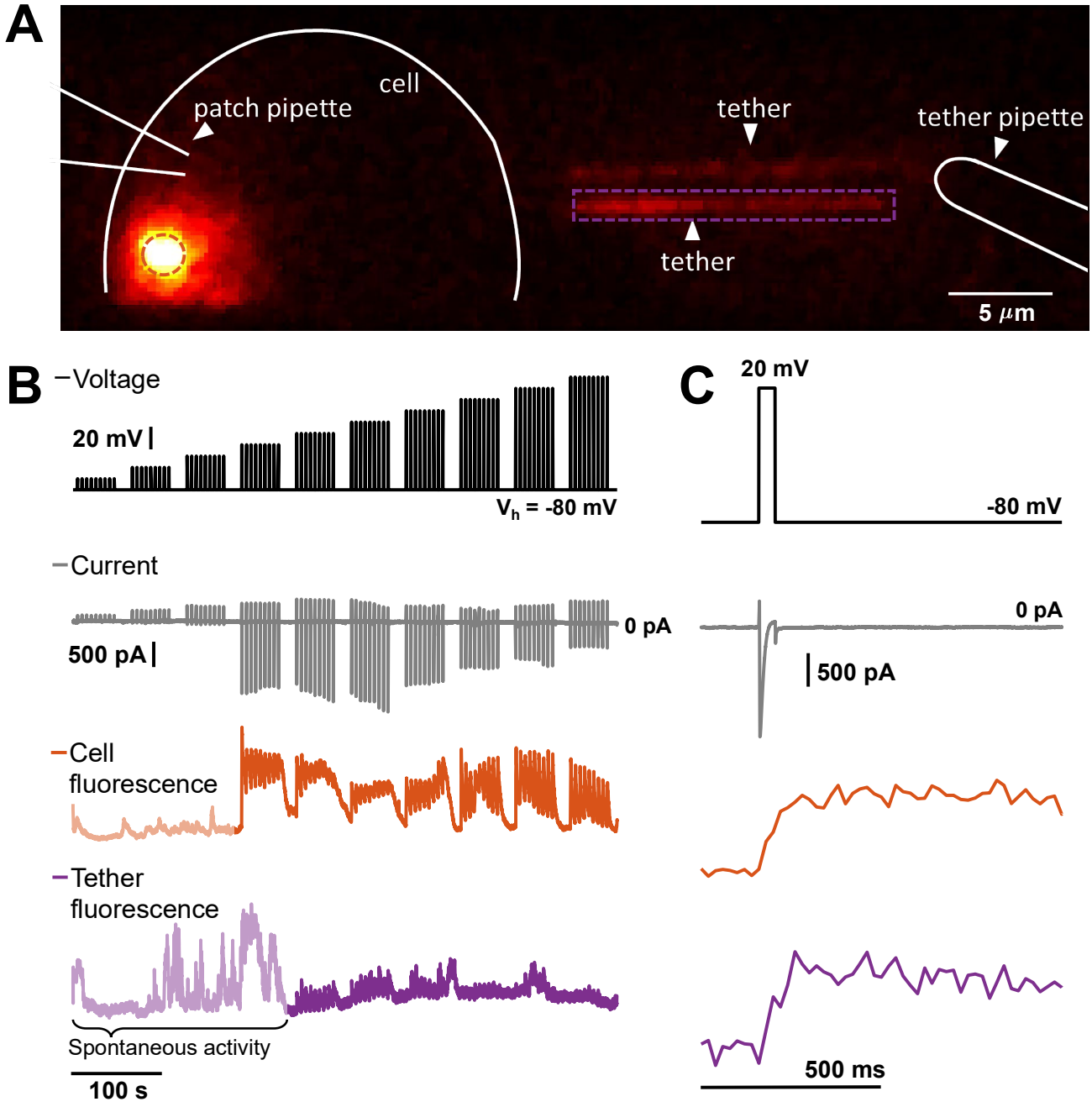

Figure 2.2 Simultaneous recording of tether and cell body Ca^{2+} dynamics.
A. $Ca_V3.2$ expressing HEK293 cell with localized excitation of a membrane-targeted GECI (GCaMP6s-CAAX) in the cell body (orange circle) and tether (purple rectangle). **B.** Concurrent patch-clamp recording of evoked currents (gray) and Ca^{2+}-dependent fluorescence in the cell body (orange) and tether (purple) in response to depolarizing voltage steps (black) of 10-100 mV from a holding potential of -80 mV. Light-shaded regions indicate epochs of spontaneous Ca^{2+} influx, which were excluded from analysis. **C.** Magnified view of traces in B. Trains of 9 repeats of 45 ms voltage pulses with a 5 s rest between pulses and a 15 s rest between pulse trains. Current and voltage traces were sampled at 100 kHz. Cell body and tether fluorescence were recorded at 50-200 Hz.

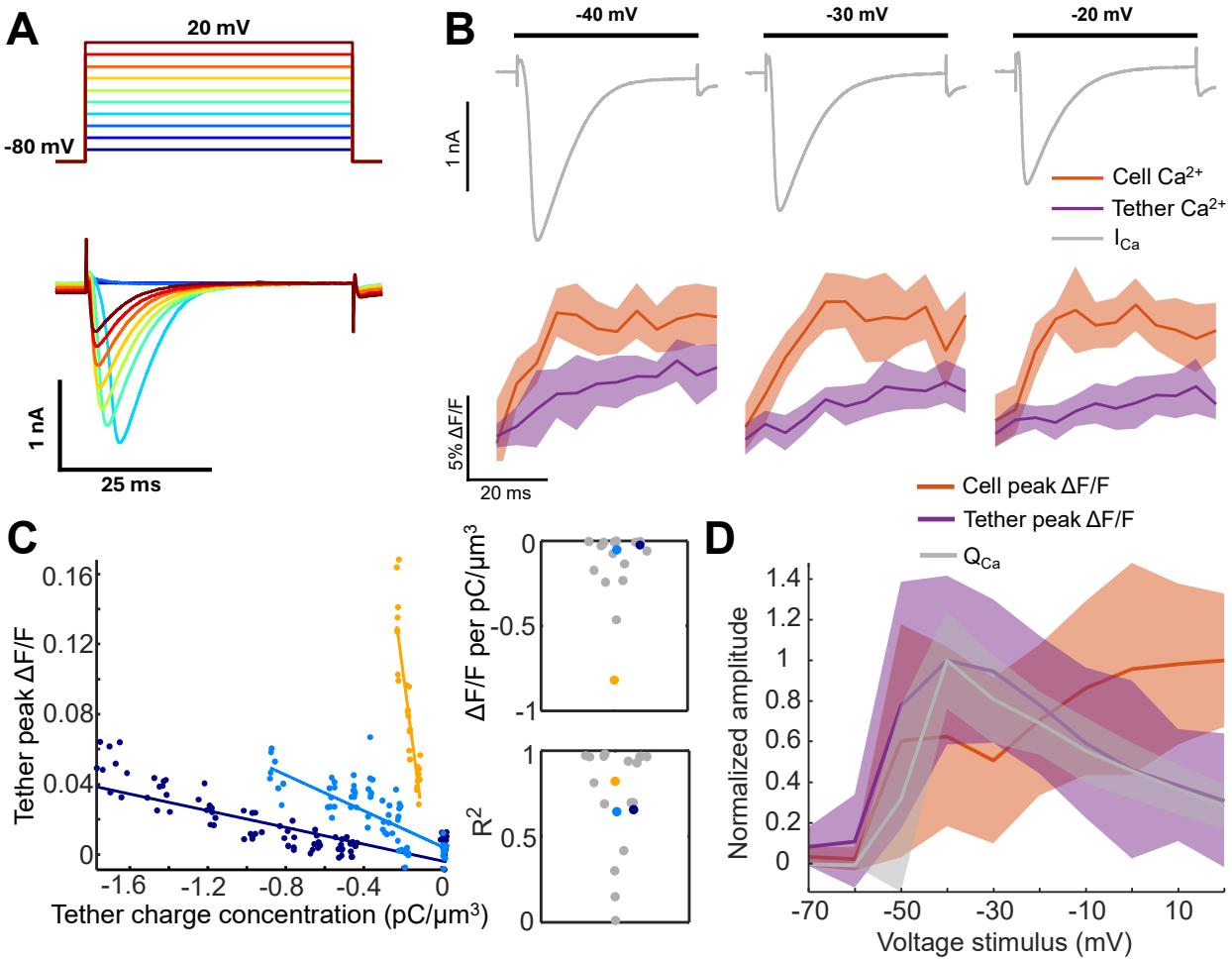

Figure 2.3 Tether Ca^{2+} signal correlates with whole-cell charge transport.
A. Inward currents (bottom) recorded from a $Ca_V3.2$ expressing HEK293 cell in response to 45 ms depolarizing voltage steps (top). **B.** Trial averaged current (top), cell (orange) and tether (purple) lck-jGCaMP8f fluorescence responses to membrane depolarizations. To calculate $(DF/F)^t$, DF/F was first calculated for each position along the tether using the pre-stimulus baseline fluorescence as F, then averaged along the tether length. Data shown for one cell (n = 9 trials, std. dev. shading). **C.** Peak $(\Delta F/F)^t$ amplitude of tether lck-jGCaMP8f fluorescence transients as a function of predicted tether charge concentration, $[Q_{Ca}^t]$, and linear fits. Data and fits shown for three example tethers. Inset: slope (top) and R^2 (bottom) from linear fits of n = 20 tethers. **D.** Voltage dependence of stimulus-evoked charge influx (gray), tether (purple) and cell (orange) peak ΔF/F amplitudes averaged across n = 25 lck-jGCaMP8f cell-tether pairs. Traces are normalized for each tether-cell pair before averaging and shaded to show std. dev. Tether peak $(\Delta F/F)^t$ and Q_{Ca} were more closely correlated than were cell peak $(\Delta F/F)^C$ and Q_{Ca}.

2.3.3 Ca^{2+} indicator reports discrete influx events

We observed stimulus-triggered Ca^{2+} events which originated from distinct positions along the tether and which fluctuated in number and position between successive voltage steps (**Figure 2.4 A-B**, **Figure A.4**). We visualized these Ca^{2+} events via kymographs, where fluorescence was displayed as a function of position along the tether and time. We combined smoothing and automated thresholding to identify peaks that were > 3 $\pm$ 0.9 s from baseline fluctuations and separated by > 0.7 μm (Section 2.5 Methods). By comparing recordings taken at the holding potential of -80 mV (when $Ca_V3.2$ channels are expected to be closed) to the recordings during voltage steps, we estimate a false-positive rate of 0.9% (**Figure A.5**).

We calculated stimulus-triggered average spatio-temporal footprints of isolated events (separated by >1.4 μm) (**Figure 2.4 C, Figure A.4**). These footprints captured the rapid depolarization-triggered Ca^{2+} influx and spread. Since the response-time of the Ca^{2+} measurements (~40 ms to peak) was comparable to the 45 ms duration of the voltage pulse, we could not resolve variations in the onset of Ca^{2+} influx relative to the voltage upstroke.

We observed clear non-exponential decay of the peak Ca^{2+} signal (**Figure 2.4 D, Figure A.4**). The 1-dimensional diffusion kernel for a d-function impulse of Ca^{2+} is $K(x,t) = \frac{1}{\sqrt{4\pi Dt}} \exp\left(-\frac{x^2}{4Dt}\right)$. Evaluating this expression at x = 0 implies that the peak concentration should decay as ~ $1/\sqrt{t}$. **Figure A.6** shows a fit of the fluorescence decay to this simple model. A more detailed model of the fluorescence decay would include dynamic equilibrium of Ca^{2+} with endogenous buffers; the nonlinear and time-dependent relation between Ca^{2+} concentration and GECI fluorescence; overlap of Ca^{2+} from neighboring Ca_V gating events; and slow interchange of Ca^{2+} between the tether and the cell body. Our analysis relied only on the initial peak signal, and so did not depend on these quantities.

We quantified the linear density of gating events in each stimulation epoch (**Figure 2.4 E**) and observed a peak density of approximately 0.15 μm^{-1}. Assuming statistically independent gating of each channel, the number of gating events is expected to follow Poisson statistics. We estimated that at the maximum activation density of 0.15 μm^{-1}, the probability of two events co-occurring within our detection window was ~13%. We did not observe a correlation between the number of detected events and the tether radius.

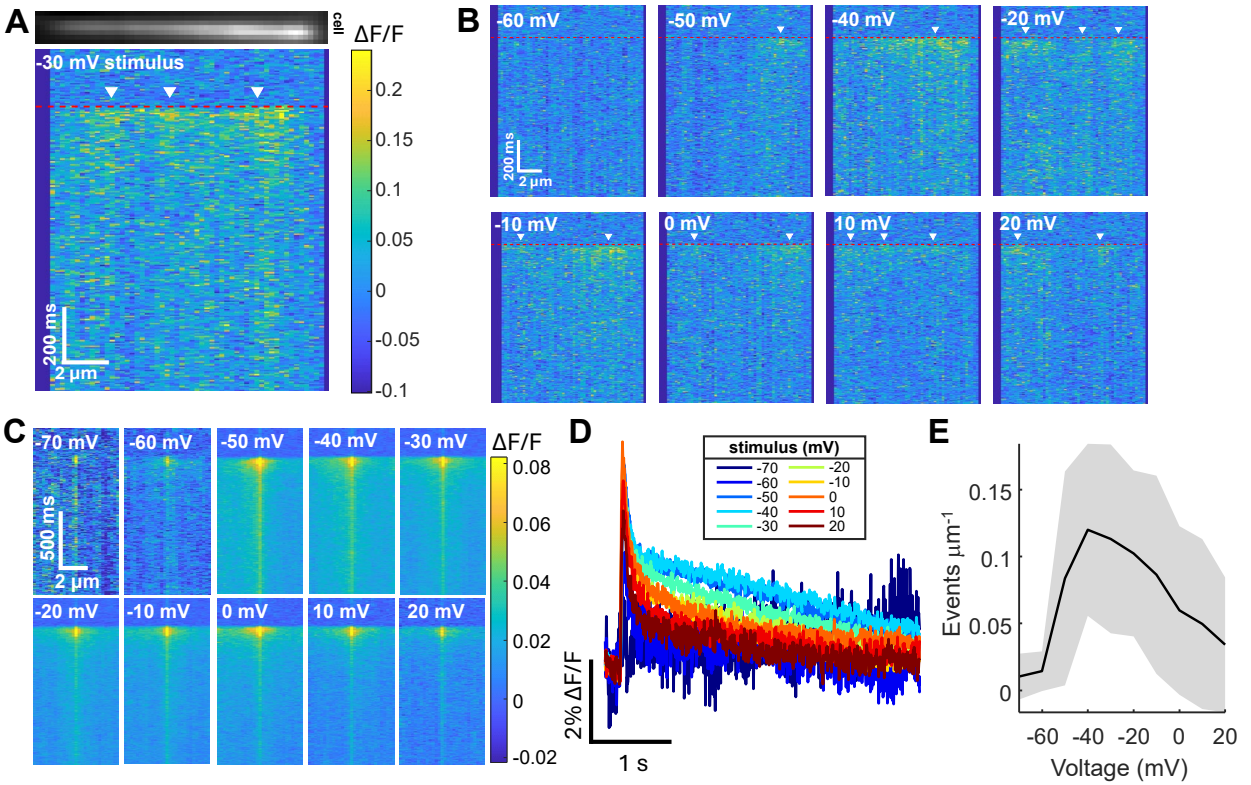

Figure 2.4 Tether Ca^{2+} signal comprises discrete events.
A. Epifluorescence image of a tether above a kymograph for a 45 ms voltage step from -80 mV to -30 mV. Red dashed line indicates step onset. White arrowheads indicate discrete Ca^{2+} events. **B.** Kymographs of tether Ca^{2+}-dependent fluorescence in response to voltage steps from -80 mV to between -60 mV and +20 mV. Data shown for single-trial responses of one tether. **C.** Stimulus-triggered average kymographs of spatially isolated tether Ca^{2+} events (8-251 events per voltage, n = 25 tethers, 17 cells). **D.** Time-course of events in (C), averaged over space. **E.** Linear density of observed Ca^{2+} influx events vs. voltage (mean ± s.d., n = 19 tethers).

2.3.4 Amplitude and frequency of single-channel gating events

We next compared event characteristics reported by tether lck-GCaMP8f to whole-cell electrical measures of channel gating. For each voltage step, we constructed a histogram of the unitary event amplitudes $(\Delta F/F)^t$ (**Figure 2.5 A**). We reasoned that the ensemble average of these discrete gating events should reproduce the previously observed linear relationship between $(\Delta F/F)^t$ and $Q_{\mathrm{Ca}}^{\mathrm{t}}$ (Eq. 2.5). To test this idea, we summed all unitary event amplitudes for each voltage. The plot of cumulative $(\Delta F/F)^t$ vs. voltage closely followed the plot of $Q_{\mathrm{Ca}}^{\mathrm{C}}$ vs. voltage, determined from the whole-cell patch clamp measurements (**Figure 2.5 B**). Thus, the fluorescence-detected Ca^{2+} events, when combined to create an ensemble average, recapitulated the voltage-dependent behavior of the macroscopic currents. This correspondence indicates that the gating properties of $Ca_V3.2$ were preserved upon channel partitioning into tethers.

We then sought to model the distribution of $(\Delta F/F)^t$ at each voltage. This distribution is not directly accessible from ensemble-average patch clamp measurements. We thus turned to stochastic simulations of channel gating. We fit a Hodgkin-Huxley-like model[96,97] of channel gating to the whole-cell currents recorded across voltage steps from -70 mV up to +20 mV (**Figure 2.5 C**). We then performed stochastic simulations of single-channel gating, using the kinetic parameters derived from the fit to the whole-cell currents (**Figure 2.5 D**, **Table A.2**, Appendix A2-3, **Figure A.7**)[98,99]. For each voltage step, we calculated the distribution of single-channel Q_{Ca}^{t} values, taking into account the voltage-dependent gating dynamics and the driving force for Ca^{2+} entry.

In the simulated single-channel trajectories, the probability of channel opening saturated at depolarized potentials (**Figure A.7**). In contrast, we observed a decrease in the frequency of Ca^{2+} events at depolarized potentials (**Figure 2.5 E**, black trace). At depolarized potentials, we expect faster $Ca_V3.2$ channel kinetics, lower driving force for Ca^{2+} entry and, thus, lower unitary charge passed by the channel. We hypothesized that these very small Ca^{2+} influx events might be below our detection threshold. To test this hypothesis, we applied a threshold to the simulated distributions of $Q_{\mathrm{Ca}}^{\mathrm{t}}$ (**Figure A.7**) and counted the voltage-dependent frequency of events that exceeded this threshold. Upon varying the simulated detection threshold, we found best correspondence between simulation and experiment at a threshold of 0.38 fC for GCaMP8f and 0.4 fC for GCaMP6s (**Figure 2.5 D** and **E, Figure A.8**). This detection threshold

corresponds to an equivalent constant current of ~9 fA over t_V = 45 ms; or to 100 fA for a 4 ms gating event. These unitary charges are substantially smaller than are typically recorded by patch clamp.[33,34]

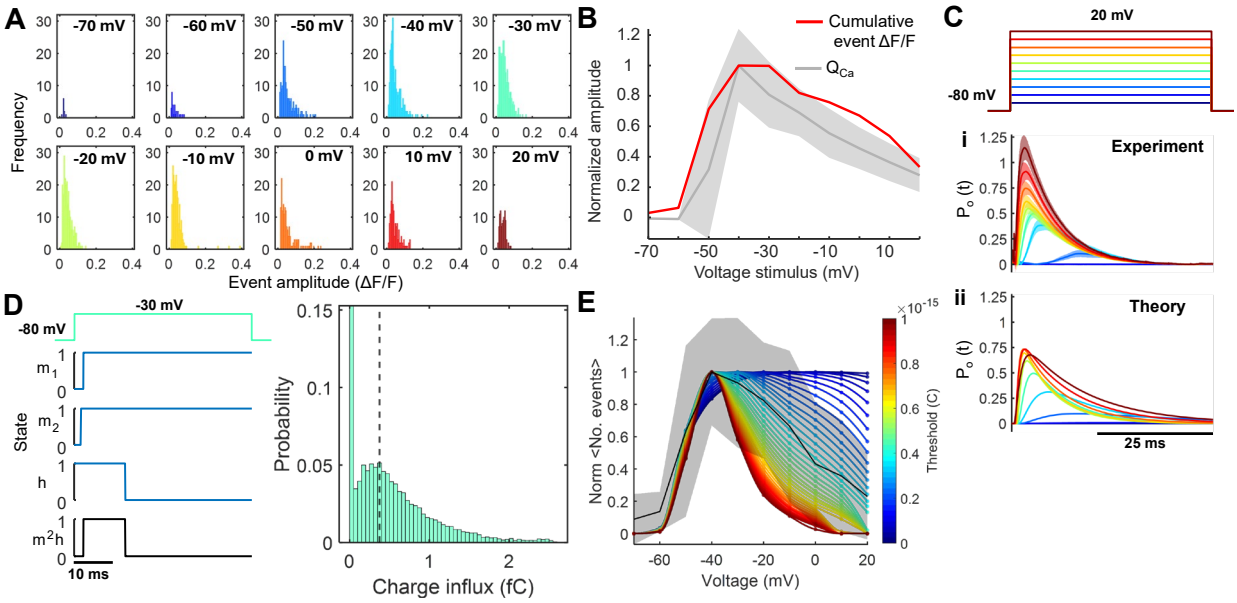

Figure 2.5 Single-molecule gating properties of $Ca_V3.2$.
A. Histograms of tether Ca^{2+} event amplitudes (10-277 events recorded per voltage stimulus, n = 25 tethers, 17 cells). **B.** Cumulative amplitudes of the event histograms in A (red) and average charge influx for the corresponding cells (gray) as a function of voltage (n = 25 cell-tether pairs). Shading indicates std. dev. **C.** $Ca_V3.2$ channel open probability, P_O, in response to depolarizing voltage steps from a holding potential of -80 mV (top). (i) P_O estimated from inward currents (n = 17 cells, shading indicates s.e.m.) and (ii) P_O calculated using a Hodgkin-Huxley-like model of gating transitions. **D.** Left: stochastic simulation of a channel gating trajectory in response to depolarization of duration t_V. Blue traces show individual gate trajectories, black trace shows channel state (m^2h). Right: distribution of charge influx, q, due to single-channel openings in response to depolarization to -30 mV for duration t_V (n = 10^4 channel trajectories). Calculated by integrating Eq. A7 over t_V. Black dashed line indicates predicted detection threshold from E. **E.** Frequency of observed events vs. voltage (normalized, black, shading std. dev. of n = 19 tethers) and predicted single-channel event probability for different detection thresholds (colors). Color bar indicates simulated charge detection threshold (maximum R-value at 0.38 fC threshold). Using the average event frequency and thresholded event detection probability, we estimated the average linear density of channels to be $\sim 0.2 \pm 0.1\ \mu m^{-1}$ (mean ± s.d.; n = 16 tethers).

2.4 Conclusions

Historically, it has been challenging to measure small ionic or biomolecular fluxes in intact membranes. Here, we showed that membrane tethers can compartmentalize and thereby amplify single-channel fluxes. Using membrane-targeted GECIs in tethers, we detected puncta of elevated Ca^{2+} in response to voltage-dependent gating of a low-conductance $Ca_V3.2$ channel (**Figure 2.4**). Despite slow GECI kinetics, the tethers amplified and prolonged [Ca^{2+}] transients enough that single-channel gating events were readily detectable (**Figure 2.1**).

We compared the amplitude and frequency of tether Ca^{2+} events to ensemble $Ca_V3.2$ electrophysiology. The mean height of tether Ca^{2+} transients correlated with the charge passed during depolarizing stimuli (**Figure 2.3**, **Figure 2.5**). Conversely, cell GECI fluorescence was poorly correlated with transported charge, likely due to intracellular Ca^{2+} transport. Pharmacological silencing of intracellular Ca^{2+} transport pathways might improve this correspondence. By comparing simulated single-channel gating trajectories and the observed frequency of Ca^{2+} events, we estimated a detection sensitivity of ~0.4 fC, corresponding to ~1250 Ca^{2+} ions (**Figure 2.5**). Strong buffering of intracellular Ca^{2+} presented a challenge for our measurements. It is estimated that the basal buffering capacity of cytoplasm ranges from 100 to 200,[18,89,100] so an influx of 1250 Ca^{2+} ions corresponds to only 6 – 13 free Ca^{2+} ions.

An extension of the current work would be to label the $Ca_V3.2$ channels directly, and to image their single-molecule fluorescence in a second fluorescence wavelength. This would provide an independent estimate of the number of channels in the tether. Additional fluorescence wavelengths could also be useful for independent fluorescent tags in the membrane or cytoplasm, either of which could be used to improve estimates of tether diameter.

In principle, our tether-based recording scheme can generalize to other proteins (e.g. channels, transporters, membrane associated enzymes). The key requirement is a suitable fluorescent reporter of the substrate or products.[38] For a 10 μm tether, a turnover rate of 100 s^{-1} at the distal end of the tether, and an unbuffered substrate with a diffusion coefficient of 200 $\mu m^2/s$, the local concentration increase is 1 μM, and the substrate residence time is 250 ms. These parameters benchmark the sensitivity needed for different substrate fluxes. Many parameters contribute to determining flux through a transport protein,

including the chemical and electrical potentials of transported species, permeation mechanism, protein conformational dynamics, bilayer tension, post-translational modifications, cofactor binding, and redox chemistry.[7,78,79] Single-channel recordings in tethers open the door to exploring these factors in a cellular context.

We observed a good correspondence between the average $Ca_V3.2$ gating behavior in tethers and bulk $Ca_V3.2$ electrophysiology, which indicates that $Ca_V3.2$ channel gating is not disrupted in tethers. In general, however, isolation of proteins in tethers has the potential to perturb their function, e.g. via differences from the parent cell in membrane tension, curvature, or cytoskeletal and organellar associations.[84,101,102] As with any single-molecule technique, one must validate (e.g. by comparison to the ensemble-averaged bulk) that the isolation strategy does not perturb the molecule of interest.

Some cellular membranes natively contain nanoscale compartments, such as dendritic spines,[5] neurites,[103,104] primary cilia,[105] synaptic vesicles,[4] tunneling nanotubes,[77] and retraction fibers.[106] Our work highlights the possibility that stochastic single-channel gating events within these structures can lead to substantial fluctuations in substrate concentration. Whereas membrane signaling is typically modeled via ensemble-average kinetics, a direction for future research will be to explore the biological roles of stochastic single-molecule gating in nanoscale compartments.

2.5 Methods

2.5.1 Genetic constructs

We used membrane targeted Lck-jGCaMP8f and GCaMP6s-CAAX Ca^{2+} indicators to detect single-channel tether Ca^{2+} transients. Both constructs were expressed under the control of a CMV promoter. The *pGP-CMV-GCaMP6s-CAAX* construct was a gift from Tobias Meyer (Addgene #52228) and used as provided. The *pGP-CMV-lck-jGCaMP8f* construct used in this work was made from a *pZac2.1-GfaABC1D-lck-jGCaMP8f* plasmid gifted by Loren Looger (Addgene #176759).

lck-jGCaMP8f was cloned into a pGP-CMV vector backbone (Addgene #104483) using Gibson assembly. Briefly, the vector was linearized by sequential digestion using restriction enzymes (New England Biolabs) and purified by GeneJET gel extraction kit (ThermoFisher). The insert fragment was generated by polymerase chain reaction amplification and inserted into the backbone using NEBuilder

HiFi DNA assembly kit (New England Biolabs). The resulting construct was verified by sequencing (Primordium).

2.5.2 Cell culture and transfection

HEK293 cells stably expressing Tet repressor (T-REx-293, ThermoFisher), constitutive human $K_{ir}2.3$, and doxycycline-inducible human $Ca_V3.2$ were a generous gift from Terrance Snutch. $Ca_V3.2/K_{ir}2.3$ cells were maintained at 37 ˚C and 5% CO_2 in Dulbecco's modified Eagle's medium (DMEM) formulated with high glucose, GlutaMAX, and pyruvate (Cat. No. 10569010, ThermoFisher) and supplemented with 10% heat-inactivated fetal bovine serum, penicillin (100 U/mL), and streptomycin (100 µg/ mL). Culture medium was supplemented with geneticin (600 µg/mL, Life Technologies), hygromycin B (150 µg/mL, Sigma Aldrich), and blasticidine (10 µg/mL, ThermoFisher) selection agents. Selection agents were removed and cells were passaged at least 24 hr prior to transfection with GECI constructs. Passaged cells were grown to ~80% confluence prior to transfection with TransIT-293 (Mirus Bio) according to manufacturer protocols. $Ca_V3.2$ expression was induced 24-72 hr prior to imaging using 150 pg/mL - 15 ng/mL doxycycline (Sigma). A doxycycline dose of 1.5 ng/mL generated a whole cell $Ca_V3.2$ conductance of 5.6 $\pm$ 1.5 pS/µm^2 (n = 17 cells) at -20 mV (**Figure A.2 E**).

2.5.3 Patch-clamp electrophysiology

Whole cell voltage-clamp recordings were acquired from $Ca_v3.2$ expressing cells. On the morning of an experiment, cells were trypsinized and replated on poly-D-lysine (Sigma) coated glass bottom dishes (20 µg/mL incubated at RT overnight or 20 min at 37 ˚C, washed 3x with phosphate-buffered saline). Prior to an experiment, cells were washed 2x and immersed in an extracellular solution containing (in mM): 125 NaCl, 25 glucose, 15 HEPES, 2.5 KCl, 1 $MgCl_2$, 2 $CaCl_2$. Patch pipettes (1-10 MΩ) were filled with an internal solution containing (in mM): 8 NaCl, 130 $KMeSO_3$, 10 HEPES, 4 MgATP, 0.3 Na_3GTP, 5 KCl. The pH was adjusted to ~7.3 using KOH and the osmolarity was adjusted to ~295 mOsm/L with sucrose. Signals were amplified using an Axopatch 200B amplifier (Molecular Devices), filtered at 5 kHz and digitized at 100 kHz (DAQ PCIe-6323, National Instruments). A micromanipulator (Sutter) maneuvered patch pipettes to the cell membrane. Cell membrane voltage was clamped at a holding potential of -80 mV and then stimulated with depolarizing pulse trains (9x 45 ms pulses, 5 s inter-pulse rest, 15 s inter-

train rest, **Figure *2.2* B-C**). All experiments were performed at 32 ˚C with temperature control provided by an objective heater (Bioptechs) and stage heater (Warner).

2.5.4 Tether formation

Micropipettes were pulled from glass capillaries (World Precision Instrument, 1B150F-4) using a pipette puller (Sutter P1000) and the tip of the pipette was sealed and rounded using a microforge (WPI, DMF1000) to form a microneedle. Microneedles were surface treated via incubation in poly-D-lysine (100 µg/mL, 37 ˚C for 20 min) followed by incubation in concanavalin A (100 µg/mL, Vector Laboratories) until use. A micromanipulator maneuvered the microneedle to the cell surface and tethers were formed upon brief contact and retraction of the microneedle tip from the membrane.

2.5.5 Imaging

Ca^{2+} imaging was performed on a custom-built inverted microscope using a 60x water immersion objective (Olympus, UPLSAPO60XW). Illumination, spatial light patterning, patch amplifier, data acquisition card, and camera were controlled with custom MATLAB (Mathworks) based software.[107] A digital micromirror device (DMD, Texas Instruments DLP3000) restricted 488 nm excitation light (81 mW/mm^2, PhoXX-488-60) to cell and tether ROIs. GECI fluorescence was imaged onto an EMCCD camera (DU-897E-CSO-#BV, Andor) with 300x electron-multiplying gain at a rate of 50-200 Hz. An adjustable slit (VA100, Thorlabs) restricted incident light to a subset of camera rows to enable high-speed imaging. Camera frames were either acquired at the rising edge of patch-clamp voltage stimuli or aligned in post-processing. Fluorescence recordings were registered in time to the voltage-clamp data by reference to the shared the DAQ clock.

2.5.6 Image processing and Ca^{2+} event finding

Tether orientation and transverse offset were identified using the Random Sample Consensus (RANSAC) algorithm.[108] Tether motion was compensated in post-processing to stabilize the image of the tether. Fluorescence was averaged along the width (short axis) of the tether and plotted as a function of time and position along the length of the tether. To these kymographs, we applied a median filter and a spatio-temporal smoothing filter. We calculated a global threshold for each recording using Otsu's method.[109] To segment Ca^{2+} events, we thresholded each recording and assigned peak amplitude and position to local maxima.[110] Spontaneous Ca^{2+} activity typically appeared outside the narrow time window

in which evoked events occurred. Stimulation epochs contaminated by spontaneous activity were thus identified and removed from our analysis. In instances where events were detected less than 0.7 μm apart, the smaller amplitude event was discarded. Additionally, we discarded any kymograph frames with greater than 0.5 events/μm.

2.5.7 Data Analysis

Data processing and image analysis were performed in MATLAB (Mathworks) and ImageJ.[111] Ca^{2+} diffusion modeling is described in Appendix A.1. $Ca_V3.2$ channel modeling and stochastic simulations are described in Appendix A.2 and A.3. To compare observed Ca^{2+} event frequency to that predicted by our stochastic simulations (**Figure 2.5 D, E**), we first calculated the mean events vs. voltage per tether and then averaged across tethers. Then, starting with the simulated distributions of charge influx, we applied a charge detection threshold, and calculated the expected frequency of detected events vs. voltage. We varied the simulated detection threshold to identify the threshold that gave closest correspondence to our data.

2.6 Manuscript Information

A version of this chapter is published[112]. Supporting information for this chapter is provided in Appendix A.

2.6.1 Acknowledgements

We thank A. Preecha, S. Begum, and C. Bodden for technical assistance, S. Innes-Gold, H. Davis, and F.P. Brooks for assistance with instrumentation, P. Park and Y. Wang for assistance with electrophysiology and E. Moult and K. Xiang for helpful discussions regarding data analysis and modeling. We thank T. Meyer, L. Looger, and D. Kim for GECI plasmid constructs and T. Snutch for the $Ca_V3.2$ cell line. This work was supported by Vannevar Bush Faculty Fellowship N00014-18-1-2859 (A.E.C.), NSF Quantum Sensing for Biophysics and Bioengineering (QuBBe) Quantum leap challenge institute (QLCI) grant OMA-2121044, and National Science Foundation Graduate Research Fellowship Grant #DGE 2140743 (M.R.H.). **Figure 2.1**, **Figure A.1 C**, **Figure A.2 A** contain elements created in BioRender (Howell, M. (2025) https://BioRender.com/r68vq1t).

2.6.2 Author contributions

Madeleine R. Howell and Adam E. Cohen conceptualized the study and designed the experiments. Madeleine R. Howell performed the experiments, analyzed the data, and performed simulations. Madeleine R. Howell and Adam E. Cohen interpreted the data and wrote the paper. Adam E. Cohen supervised the project.

3 Electrophysiology in nanoscale compartments

3.1 Abstract

Voltage-gated ion channels play important roles in many membrane-enclosed structures, including synaptic vesicles, endosomes, mitochondria, chloroplasts, viruses and bacteria. Here we study how compartment size and channel gating interact to shape voltage dynamics and ion content in sub-micron structures. In small compartments, assumptions underlying conductance-based (Hodgkin-Huxley type) models of membrane voltage must be relaxed: [1] stochastic gating of individual ion channels can quickly and substantially change membrane voltage; [2] these changes can equilibrate faster than channel state transitions; and [3] ionic currents, even through as few as two channels, can substantially alter ionic concentrations. We adapted conductance-based models to incorporate these effects, and we then simulated voltage dynamics of small vesicles as a function of vesicle radius and channel density. We identified regimes in this parameter space with qualitatively distinct dynamics. We then performed stochastic simulations to explore the role of $Na_V1.5$ in maturation of macrophage endosomes. The stochastic model predicted dramatically different dynamics compared to a deterministic approach. Electrophysiology of nanoscale structures can be very different from larger structures, even when ion channel composition and density are preserved.

Significance: With tools of optical electrophysiology, one can measure and perturb membrane voltage in sub-micron structures. Recent experiments in organelles, dendritic spines, and bacteria motivate a re-examination of basic assumptions about bioelectrical phenomena in these compartments. This paper provides a framework for predicting and interpreting bioelectrical dynamics in small structures.

Keywords: organelle electrophysiology, ion channel stochasticity, Markovian simulations

3.2 Introduction

Ion channels and pumps operate not only in large, patch-clamp-accessible cells, but also in many small membrane-enclosed structures, including synaptic vesicles [113,114], endosomes [115], lysosomes [16], mitochondria [116], chloroplasts [117], and diverse microbes and viruses [118–122] (**Figure 3.1 A**). Electrochemical gradients in these compartments are integral to cell physiology: they drive ATP synthesis in mitochondria [123]; regulate acidification and cargo processing in secretory and endocytic organelles [114,124,125]; and contribute to pH- and voltage-dependent stages of viral entry [126,127]. In bacteria, voltage- and mechano-sensitive ion channels participate in homeostasis of membrane potential, osmotic pressure, and ionic balance [119,128]. Yet, despite their ubiquity and functional importance, the electrophysiology of sub-micron compartments has historically been difficult to interrogate because of their small size, intracellular location, and (in microbes) the presence of a cell wall[129].

This experimental barrier is now largely breached. Genetically encoded voltage indicators [47,130–134] and small-molecule dyes [39,40,135,136] enable *in situ* voltage measurements in small and/or intracellular membranes [137,138], with targeted implementations in mitochondria [139,140], dendritic spines [141], distal astrocytic processes [142], lysosomes [49,125], and bacteria [143,144]. Complementing protein and dye indicators, DNA-based probes have directly reported organelle electrical and ionic state variables in live cells: an organelle-targeted “voltmeter” reported absolute membrane potentials across multiple organelle classes [49]; single-organelle Na^+ mapping revealed pronounced heterogeneity and maturation-dependent shifts in lumenal sodium [55]; and an organelle-localized reporter indicated that voltage-gated K^+ channels canonically associated with the plasma membrane can be functionally active on trafficking organelles, with measurable consequences for lumenal K^+ [145].

Together, these experiments raise mechanistic questions that are difficult to answer with classical electrophysiology models: how are organelle voltages and Na^+/ K^+ gradients established and maintained when copy numbers of channels/transporters are small [13–15]? When organelle-to-organelle variability is large [55], does this reflect deterministic maturation-dependent shifts, stochastic variations in channel number, or rare but consequential stochastic gating events? And how do transient channel openings during trafficking reshape lumenal ion composition, potentially modulating downstream processes such as acidification, cargo sorting, and maturation [124,125]?

Answering these questions presents a challenge for the standard theoretical framework for membrane voltage—the Hodgkin-Huxley (HH) family of conductance-based models—which rests on approximations appropriate for large membranes. First, HH-type descriptions are mean-field: conductances represent ensemble averages over many channels, and fluctuations are commonly treated as small perturbations around the mean. In the regime of finite-but-large channel number *N*, channel noise is often well approximated by a Gaussian perturbation to conductance (or gating variables), yielding Langevin/Fokker-Planck descriptions in which voltage performs a diffusion-like biased random walk about a stable fixed point and spiking can be described as a Kramers escape process [146–153]. A substantial literature has explored how membrane area and morphology filter or amplify this conductance noise and how it impacts spike timing and reliability [17,147,154,155]. These approaches have been powerful precisely because individual channel events contribute only weakly to V_{m}, and because averaging over many channels smooths the dynamics.

Sub-micron compartments can instead inhabit a qualitatively different regime in which voltage dynamics are dominated by discrete single-channel gating events, not by Gaussian fluctuations around a mean conductance. Two basic scalings drive this transition. (i) Membrane leak conductance scales with membrane area, so the same single-channel current produces a larger steady-state ΔV_{m} in a smaller compartment; in sufficiently small structures, opening of a single channel can drive V_{m} close to that channel's reversal potential.(ii) The membrane charging time in small structures can become fast compared to the characteristic channel state-transition times,so channels "feel" their own impact on during an opening event. This self-action breaks the separation between channel kinetics and voltage dynamics that underlies diffusion approximations: instead of nearly continuous, Gaussian-like voltage noise, the system exhibits jump-like trajectories with history-dependent effective kinetics (**Figure 3.1 B**). In this regime, it is no longer sufficient to treat stochasticity as a small, additive perturbation to HH dynamics.

A second HH assumption also can break down in small compartments: that (except for Ca^{2+}) ionic concentrations are effectively constant on the timescale of electrical activity. Extensions of conductance-based models to include dynamic ion concentrations and pumps have been developed for neurons and cardiac tissue [156,157], but typically in parameter regimes where concentration changes are slow compared

to individual spikes. In contrast, the same small volumes that amplify voltage responses also amplify concentration changes driven by ionic fluxes; moreover, coincident opening of channels with distinct reversal potentials can produce large counter-propagating ionic currents even when net membrane current is small, rapidly dissipating gradients in ways not captured by fixed-reversal-potential models (**Figure 3.1 C**). The relevance of this issue is underscored by emerging measurements showing that organellar ionic contents can be variable and responsive to channel activity [55,145]. Thus, a theory aimed at interpreting voltage and ion measurements in small compartments must simultaneously confront (a) discrete stochastic gating that directly controls V_{m}, (b) feedback from V_{m} onto channel gating on the timescale of single gating events, and (c) time-dependent driving forces arising from labile ionic gradients.

Here, we adapt conductance-based electrophysiology to explicitly incorporate these small-compartment effects. We treat channel gating as discrete stochastic jump processes (Markov state models) coupled self-consistently to membrane voltage, and we update ionic concentrations (and hence reversal potentials) as currents flow in nanoscale volumes. We use this framework to map regimes of qualitatively distinct dynamics as a function of vesicle size and channel density, to identify when deterministic HH-like descriptions approximate stochastic dynamics and when they fail, and to predict new behaviors—such as voltage “memory” and gradient-depletion–mediated refractoriness—that emerge when single-channel events dominate. Finally, motivated by experimental reports of $Na_V1.5$ in macrophage endosomes and its proposed role in acidification [115], we apply the stochastic, concentration-aware framework to endosome maturation, illustrating how rare channel openings can produce outsized physiological consequences in a small compartment. While we primarily analyze the roles of Na_V and K_V channels, the methodology is not limited to the canonical HH channels, but can apply to the many organelle-specific channels and transporters [158]. Together, these results provide a quantitative framework for emerging measurements of voltage and ionic composition in organelles, microbes, and other small compartments, and they suggest experimentally testable signatures of the single-channel-dominated regime.

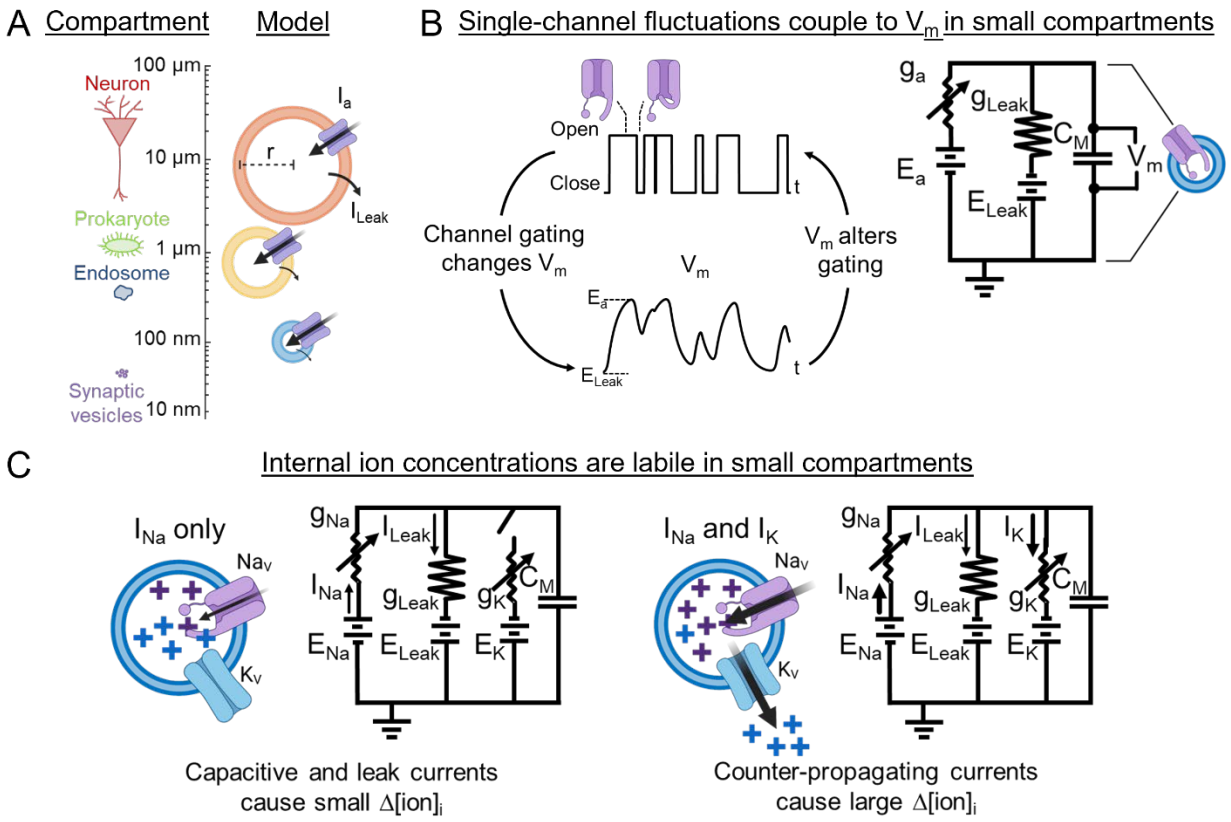

Figure 3.1 Small compartments have distinctive electrophysiology.
A. Bioelectrical dynamics occur over a wide range of spatial scales. Excitable compartments (left) and model vesicles with simplified geometry (right). **B.** In a small compartment, stochastic gating of a single channel changes V_m, which then affects channel gating. Changes in V_m alter the duration of individual channel open events and introduce a memory into the dynamics that leads to non-Markovian dynamics. In the circuit diagram, the size of the leak resistor indicates $g_{Leak} \ll g_a$. **C.** Coincident activation of channels with different reversal potentials can drive spontaneous depletion of ionic concentration gradients. Upon Na_V opening, I_{Na} charges the membrane capacitance and then maintains steady-state flow out via I_{Leak} (left panel). For realistic parameters, the capacitive charging current has little effect on internal Na^+ concentration. When Na_V and K_V opening coincide, inward I_{Na} is balanced by outward I_K until E_{Na} and E_K are equal (right panel). This current drives large changes to internal ion concentrations. Abbreviations: g_a: single-channel conductance of an arbitrary channel; g_{Na}: Na_V single-channel conductance; g_{Leak}: leak conductance; g_K: K_V single-channel conductance; E_a: reversal potential of an arbitrary channel; E_{Na}: Na^+ reversal potential; E_{Leak}: leak reversal potential; E_K: K^+ reversal potential; I_{Na}: Na_V current; I_{Leak}: leak current; I_K: K_V current; C_M: membrane capacitance; V_m: membrane potential.

3.3 Methods

All simulations were performed in MATLAB.

3.3.1 Single-channel vesicle model

We examine the interaction between stochastic channel gating and membrane voltage (V_m) using a single 14 pS conductance voltage-gated Na^+ channel (Na_V) in the membrane of a spherical vesicle. The vesicle also contains a non-specific and deterministic leak conductance proportional to vesicle area (A_m) with $g_{\mathrm{Leak}} = 1\,\frac{\mathrm{pS}}{\mu\mathrm{m}^2} \times A_{\mathrm{m}}$ and the leak reversal potentials (E_{Leak}) given below. Simulations of vesicle V_m are initialized at $V_m = E_{Leak}$. Because unidirectional single-channel currents do not substantially alter internal electrolyte concentrations, Na^+ and leak reversal potentials are not updated in simulations of single channel stochastic Na_V trajectories. The Markovian model of stochastic Na_V gating is described below (3.3.4 Markovian dynamics for voltage-gated ion channels) and in Appendix B.1. To examine the role of window currents on channel behavior, we modify Na_V kinetics to yield a model with substantial window current (Na_V^+) as well as negligible window current (Na_V^-). These modifications are described in Appendix B.1.

We simulate [1] V_m in response to a single channel opening (**Figure 3.2 A**); $E_{\mathrm{Leak}} = -93\ \mathrm{mV}$ [2] time-to-close of a channel initialized in the open state (**Figure 3.2 C**); $E_{\mathrm{Leak}} = -25\ \mathrm{mV}$ and [3] spontaneous trajectories of channel gating and V_m using either the default Na_V model (**Figure 3.2 B**), $E_{\mathrm{Leak}} = -25\ \mathrm{mV}$; or the modified window current models (**Figure 3.2 G**), $E_{\mathrm{Leak}} = -60\ \mathrm{mV}$. $E_{\mathrm{Leak}} = -25\ \mathrm{mV}$ in [2] and [3] was chosen such that V_m does not transit the window current regime, to isolate the effect of depolarization on channel kinetics and memory. $E_{\mathrm{Leak}} = -60\ \mathrm{mV}$ in [3] was chosen such that channel activation forced V_m to transit the window regime.

Annotated code for simulating the dynamics in **Figure 3.2 B, C** and **G** is available at: https://github.com/adamcohenlab/howell2025small-scale-ephys/tree/main/code-single_NaV_vesicles

3.3.2 Hodgkin-Huxley (HH) -type vesicle model

We examine the ensemble effects of stochastic and counter-propagating currents in vesicles with HH-like Na_V, voltage-gated K^+ channel (K_V) and leak conductances [159,160]. While the original HH model does not explicitly consider intracellular ion concentrations, it can be extended to an ion-specific form [156,159–165]. Following the conventions of Hübel et al., the ion concentrations and reversal potentials are

updated at each time step, a Na^+/K^+-ATPase model is added to restore the Na^+/K^+ balance, and the non-specific leak current is rendered ion-specific [156,160]. Na_V and K_V channels are modeled as discrete and stochastic with Markovian dynamics (described in 3.3.4 Markovian dynamics for voltage-gated ion channels). All other conductances are modeled as continuous and deterministic. We assume similar mobilities for Na^+ and K^+ ions, so the contribution of each ion to the injected current is proportional to its mole fraction in the extravesicular solution. The formulation is:

$$\frac{dV_m}{dt} = -\frac{1}{C_M}\left(I_{Na^+} + I_{K^+} + I_{Cl^-}\right) \quad 3.1$$

$$I_{Na^+} = \left(g_{Na_V} N_{open,Na_V} + g_{Na^+,leak}\right)(V_m - E_{Na^+}) - I_{inj}\frac{[Na^+]_o}{[Na^+]_o + [K^+]_o} + 3I_{pump} \quad 3.2$$

$$I_{K^+} = \left(g_{K_V} \cdot N_{open,K_V} + g_{K^+,leak}\right)(V_m - E_{K^+}) - I_{inj}\frac{[K^+]_o}{[Na^+]_o + [K^+]_o} - 2I_{pump} \quad 3.3$$

$$I_{Cl^-} = g_{Cl^-,leak}\,(V - E_{Cl^-}) \quad 3.4$$

$$I_{pump} = I_{pump,max}\left(1 + e^{\frac{25 - [Na^+]_i}{3}}\right)^{-1}\left(1 + e^{5.5 - [K^+]_o}\right)^{-1} \quad 3.5$$

Here V_m is the membrane potential, C_M is the membrane capacitance, E_{ion} is the reversal potential; I_{ion} is the ionic current, I_{inj} is the injection current, I_{pump} is the Na^+/K^+-ATPase current; g_{ion_V} is the conductance of a single voltage-gated channel, N_{open,ion_V} is the number of open channels, $g_{ion,leak}$ is the leakage conductance, $[ion]_i$ is the internal ion concentration, and $[ion]_o$ is the external concentration. All vesicles are modeled as spheres. The electrophysiological parameters and initial conditions of the HH-like vesicle model are in **Table B.1** and Appendix B.2.

Annotated code to simulate the dynamics in **Figure 3.3** and **Figure 3.4** is available at: https://github.com/adamcohenlab/howell2025small-scale-ephys/tree/main/code-HH_neuron_vesicles

To compare dynamics between deterministic and stochastic simulations, we used the autocorrelation of the spike train. We chose this measure because it was not sensitive to the precise spike timing. Our measure of similarity plotted in **Figure 3.4 D** was: $\left(1 - \frac{\text{rmsd}}{\text{rmsd}_{max}}\right) \times 100\%$, where rmsd is the root-mean-square deviation between the autocorrelation traces, and rmsd_{max} is the maximum rmsd seen across all vesicle sizes and channel densities.

3.3.3 Endosome model

We study the combined effects of stochastic channel dynamics and ion concentration changes in intracellular endosomes. Carrithers *et al.* reported $Na_V1.5$ channels in macrophage late endosomes, and suggested a role in endosome acidification, a part of endosome maturation [115]. The minimal endosome model includes $Na_V1.5$, vacuolar-type H^+ ATPase (v-ATPase), and H^+/Cl^- exchange transporter 7 (ClC-7) [166–168]. The $Na_V1.5$ channels are inserted in an inverted orientation relative to the cell membrane; i.e., the intracellular domain (C-terminus) is facing the outside of the endosome. For ClC-7, a 2:1 Cl^-/H^+ coupling ratio is assumed. The formulation is:

$$\frac{dV_m}{dt} = -\frac{1}{C_m}\left(I_{Na^+} + I_{Cl^-} + I_{H^+}\right) \quad 3.6$$

$$I_{Na^+} = g_{Na_V1.5} \cdot N_{open,Na_V1.5} \cdot (V_m - E_{Na^+}) \quad 3.7$$

$$I_{Cl^-} = N_{ClC-7} \cdot (2 \cdot I_{ClC-7}) \quad 3.8$$

$$I_{H^+} = N_{ClC-7} \cdot I_{ClC-7} - N_{v-ATPase} \cdot I_{v-ATPase} \quad 3.9$$

$$I_{ClC-7} = F(V_m, [Cl^-]_i, [Cl^-]_e, [H^+]_i, [H^+]_e) \quad 3.10$$

$$I_{v-ATPase} = G(V_m, [H^+]_i, [H^+]_e) \quad 3.11$$

In which I_{ClC-7} is the net current through a single ClC-7 channel, $I_{v-ATPase}$ is the single-transporter v-ATPase current; the formulations for F,G (Eqs. 3.10 and 3.11) come from literature[167,168]; $N_{channel}$ is the number of channels. The electrophysiological parameters and initial conditions of the endosome model are in **Table B.2**.

Annotated code to simulate the dynamics in **Figure 3.5 B** and **C** is available at:
https://github.com/adamcohenlab/howell2025small-scale-ephys/tree/main/code-endosome

3.3.4 Markovian dynamics for voltage-gated ion channels

To facilitate the direct comparison between stochastic and deterministic channel dynamics, Markovian state transition models are used for voltage-gated ion channels in all simulations. The Markovian models for HH-type Na_V and K_V channels, as well as the $Na_V1.5$ channel, come from literature [166,169–172]. The deterministic channel dynamics formulation is:

$$\frac{dN_k}{dt} = \sum_i \alpha_{i\to k} N_i - \sum_i \alpha_{k\to i} N_k \quad 3.12$$

In which N_k is the number of channels in state k and $\alpha_{i\to k}$ is the transition rate from state i to state k ($\alpha_{i\to i} = 0$). Transition rates for all voltage-gated ion channels are provided in Appendix B.1 and Appendix B.2.

The Gillespie method is used for the stochastic simulations [170,172]. In short, we define the sum of all the transition rates across all channels in a system as λ:

$$\lambda = \sum_k (\sum_i \alpha_{k\to i} N_k) \quad 3.13$$

Then the probability that no transition occurs in the system after time *t* follows an exponential distribution:

$$P(t) = \lambda \exp[-\lambda t] \quad 3.14$$

A random number is drawn from this distribution to determine the time elapsed before the next transition. Then, a uniform random number is drawn to determine which type of transition in which type of channel occurs, with weight $\alpha_{k\to i}\frac{N_k}{\lambda}$ assigned to each type of transition.

3.3.5 Ion concentration update

The deterministic and stochastic Markovian simulations are performed with intravesicular ion concentrations either fixed or continuously updated. The dynamic ion simulations follow the formalism of Hübel and Dahlem [156,160]. The ionic currents are converted to changes in internal and external concentrations, and the reversal potentials of each ionic species are updated accordingly. For all simulations, the external volume is set to 10^5 μm^3 – large enough that extravesicular ion concentrations are approximately constant. The ionic composition of the applied current is set proportional to the extravesicular cation ratio. For endosome simulations, a buffering capacity of 40 mM/dpH is assumed in updating the intravesicular H^+ concentration, following literature precedent [173].

3.3.6 Dynamic choice of simulation step size

To accommodate vesicle sizes and ion channel densities that vary across orders of magnitudes, the simulation step size, dt, is chosen dynamically at each step, to satisfy the following criteria: 1) $dt < 0.001$ ms; 2) $dt < 0.2\,\tau_V$, where τ_V is the characteristic membrane charging time; and 3) In a single step, the internal concentration of each ion does not change by more than 2%. In driven stochastic simulations, if dt chosen from the exponential distribution exceeds the limits set by 1), 2), or 3), then the transition is rejected and the system evolves by the time step dictated by 1), 2), or 3). In simulations of spontaneous activity in single-channel and HH-type vesicles, constraint 1) was relaxed. This minimized the number of

timesteps sampled during quiescent periods in vesicles with few channels. Additionally, in simulations of single-channel vesicles without [ion] update, constraint 3) did not apply and 2) was tightened such that $dt < 0.01\,\tau_V$. This enabled accurate calculation of time-averaged V_m.

3.3.7 Vesicle size and channel density scales

For the HH-type vesicle model, a range of physiologically relevant vesicle sizes and ion channel densities were considered (**Figure 3.3 B**). The vesicle radii were selected to correspond approximately to a synaptic vesicle (r = 0.02 μm) [174,175]; an endosome (r = 0.05 μm) [175]; a large endosome or vacuole (r = 0.4 μm) [176]; a prokaryotic cell (r = 1 μm); and a eukaryotic cell (r = 10 μm). Ion channel densities were selected as follows: [Na_V K_V] = [80 20] μm^{-2} is the approximate density on the squid giant axon, [160,170] and [Na_V K_V] = [800 200] μm^{-2} is the approximate density on a synaptic vesicle if it contains exactly one copy of the K_V channel. On a synaptic vesicle, the copy numbers of each type of ion channel and transporter are often in the single-digit regime [13,174,177–179]. The ratio of Na_V to K_V channel was fixed at 4 to 1 across all channel density scales.

For the endosome model, the vesicle radius was 0.2 μm. The density of v-ATPase was estimated to be 700 μm^{-2} and that of ClC-7 was 300 μm^{-2} [167,173]. The density of ClC-7 was adjusted so the initial membrane potential was +19 mV [180]. The density of $Na_V1.5$ on macrophage late endosomes is not known. We varied this density across a wide range, from 0 to 6400 μm^{-2}.

3.4 Results

3.4.1 Scaling electrophysiology to small systems

3.4.1.1 Single-channel perturbations to membrane voltage

We begin by examining the relationship between membrane voltage and channel dynamics in small systems. **Figure 3.1 A** depicts the scale of several electrically excitable biological systems. For simplicity, we consider a spherical membrane-bound compartment (a “vesicle”) containing a single ion channel of type *a*, with open-state conductance g_a (pS) and reversal potential E_a (mV). Assume the membrane has a specific leak conductance G_0 (pS/μm^2) and a resting potential E_{leak} (mV). Typically G_0 ~1 pS/μm^2 for neuronal membranes [156]. What is the effect of the single channel opening on the membrane potential, V_m?

If we approximate all the conductances as Ohmic, then a simple circuit analysis shows that (for static ion concentrations, i.e. fixed ion reversal potentials) the change in steady-state membrane potential upon channel *a* opening is:

$$\Delta V_{\mathrm{ss}} = \frac{g_{\mathrm{a}}(E_{\mathrm{a}}-E_0)}{g_{\mathrm{a}}+A\,G_0}, \qquad 3.15$$

where *A* is the surface area of the vesicle. For example, when $g_{\mathrm{a}}=A\,G_0$, the voltage swing is half its maximum value: $\Delta V_{\mathrm{ss}} = (E_{\mathrm{a}} - E_0)/2$. Not surprisingly, the single-channel gating has a substantial effect on the steady-state membrane potential when the unit conductance surpasses the resting leak conductance. **Figure 3.2 A** illustrates this scenario for a canonical Hodgkin-Huxley Na_V channel.

The leak conductance of a vesicle is proportional to its surface area (assuming a high density of leak channels), while the single-channel conductance is independent of the vesicle surface area. Hence, the crossover between charging regimes (i.e. when $g_{\mathrm{a}} = A\,G_0$) corresponds to a characteristic vesicle radius r_{c}. For example, for $G_0 = 1$ pS/μm² and a Na_V channel ($g_{\mathrm{a}} = 14$ pS) [181], the crossover radius is $r_{\mathrm{c}} = 1.1$ μm. For a BK calcium-activated potassium channel ($g_{\mathrm{a}} \sim 200$ pS) [182], $r_{\mathrm{c}} = 4$ μm, while for a homomeric 5-HT_{3A} receptor ($g_{\mathrm{a}} = 1$ pS) [183], $r_{\mathrm{c}} = 280$ nm.

Upon opening of a single ion channel (**Figure 3.2 A)**, the RC time constant for the voltage to approach its new steady state is

$$\tau_{\mathrm{V}} = \frac{C_{\mathrm{M}}}{g_{\mathrm{a}}+A\,G_0}, \qquad 3.16$$

where $C_{\mathrm{M}} = A\,c_0$ is the membrane capacitance (specific capacitance c_0 ~10 fF/μm²), and the denominator is the total membrane conductance. At the crossover radius r_{c}defined above, $\tau_{\mathrm{V}} = \frac{\tau_{\mathrm{mem}}}{2}$, where $\tau_{\mathrm{mem}} = \frac{c_0}{G_0}$ is the intrinsic membrane time constant. Fore example, for $G_0 = 1$ pS/μm², $\tau_{\mathrm{mem}} = 10$ ms and when $r = r_C$,$\tau_V = 5$ ms. If the single-channel gating events have duration $\tau_{opem} \gg \tau_V$, then ΔV_m approaches ΔV_{SS} during a single gating event (**Figure 3.2 A**, blue trace). If $\tau_{open} \ll \tau_V$, then the amplitude of the voltage fluctuations is suppressed to $\Delta V_{\mathrm{m}} \approx \Delta V_{\mathrm{ss}}\tau_{\mathrm{open}}/\tau_{\mathrm{V}}$ (**Figure 3.2 A**, yellow trace).

For big vesicles ($r \gg r_c$) single-channel gating changes steady-state voltage by $\Delta V_{\mathrm{ss}} \approx \frac{g_{\mathrm{a}}(E_{\mathrm{a}}-E_0)}{A\,G_0}$, with time constant $\tau_V \approx \tau_{mem}$. Since $g_a \ll AG_0$ for big vesicles, ΔV_{SS} is a small perturbation to the resting

potential (**Figure 3.2 A**, orange trace). This corresponds to the situation previously analyzed in models of channel stochasticity in neural firing [149–153].

For small vesicles ($r \ll r_c$), single-channel gating brings the voltage close to the reversal potential of channel a, i.e. $\Delta V_{ss} \approx (E_a - E_0)$. In this case the time constant is $\tau_V \approx \frac{A\, c_0}{g_a} \ll \tau_{mem}$. For example, upon activation of a single 14 pS channel in a vesicle of $r = 0.1\ \mu m$, the voltage responds with a time constant $\tau_V \approx 10^{-4}$ s (**Figure 3.2 A**, blue trace). When the channel closes, the voltage relaxes back toward the resting potential with time constant τ_{mem}.

Thus, for sufficiently small structures, the single-channel influence on the membrane voltage can be substantial and the membrane voltage equilibrates faster than the characteristic channel gating times (**Figure 3.2 B)**. Single ion channels then 'see' their own influence on V_m during a stochastic gating event. This self-action changes the statistics of channel fluctuations.

For example, consider a vesicle containing a single Na_V channel (Na_V model in **Figure B.1**) and a constitutively open 'leak' conductance. Here we assume internal ion concentrations are fixed (an assumption relaxed later) and we initialize the channel in the open state at $V_m = E_{Leak}$. In a large vesicle, Na_V opening (gating variables m^3: 0 → 1; h: 1) is quickly reversed through deactivation (m^3: 1 → 0). In a small vesicle, Na_V opening depolarizes the vesicle to a voltage which favors the open state. The channel then remains open until open-state inactivation sets in (h: 1 → 0). Closing of the channel leads to an increase in the membrane time-constant from τ_V to τ_{mem}, so the voltage recovery is slower than the voltage upstroke. **Figure 3.2 C** shows how voltage self-action prolongs mean Na_V open-state lifetimes in small vesicles relative to large vesicles, and **Figure B.2** shows the underlying distributions of Na_V open times in small and large vesicles.

In a large vesicle, channel closing after an open-state fluctuation typically resets the gating variables to $m^3 = 0$, $h = 1$. The channel is immediately available to open again. Since single-channel gating has minimal effect on V_m (**Figure 3.2 B**, bottom), the channel has constant probability of opening per unit time. Thus, the closed-state waiting-time distribution is exponentially distributed at short times. Occasionally, open-state fluctuations terminate in an inactivated state ($h = 0$). These rare events lead to a long exponential tail to the waiting time distribution (**Figure 3.2 D**).

In a small vesicle, an open-state fluctuation induces a large depolarization, which continues to act after the channel has inactivated ($h = 0$). The voltage then relaxes back toward E_{Leak} with time constant τ_{mem} (**Figure 3.2 B**, top). The time-dependent voltage interacts with the voltage-dependent gating parameters to produce a complex waiting-time distribution (**Figure 3.2 D**). As a result of the residual depolarization following an open event, the time-average membrane voltage is more depolarized in small vesicles than in large vesicles (**Figure 3.2 E**).

If the resting potential, E_{Leak}, is hyperpolarized relative to E_{Window}, the window current regime is wide enough, and the repolarization is slow enough, then the channel may have a high probability to re-open when the voltage nears E_{Window} (**Figure 3.2 F**, green trace). In trajectories simulated with a Na_V model modified to have a large window current, we observed voltage oscillations between E_{Window} and E_{Na}. Occasionally the voltage repolarized below E_{Window} without the channel opening, leading to a quiescent epoch with voltage close to E_{Leak} (**Figure 3.2 G**, green trace). A spontaneous opening event would then re-start the oscillatory dynamics. The membrane voltage thus "chattered" between epochs at E_{Leak} and oscillations between E_{Window} and E_{Na} (**Figure 3.2 F-G**, green trace). This behavior was absent in large vesicles containing the same Na_V model. In a Na_V model modified to have negligible window current (**Figure 3.2 F**, purple trace), the voltage repolarized completely to E_{Leak} (**Figure 3.2 G**, purple trace). **Figure B.3** shows the distributions of Na_V closed times for these different scenarios. Through large V_m fluctuations and slow membrane voltage repolarization, small vesicles endow channels with a "memory" of prior gating events, which can lead to a rich repertoire of vesicle size-dependent dynamics.

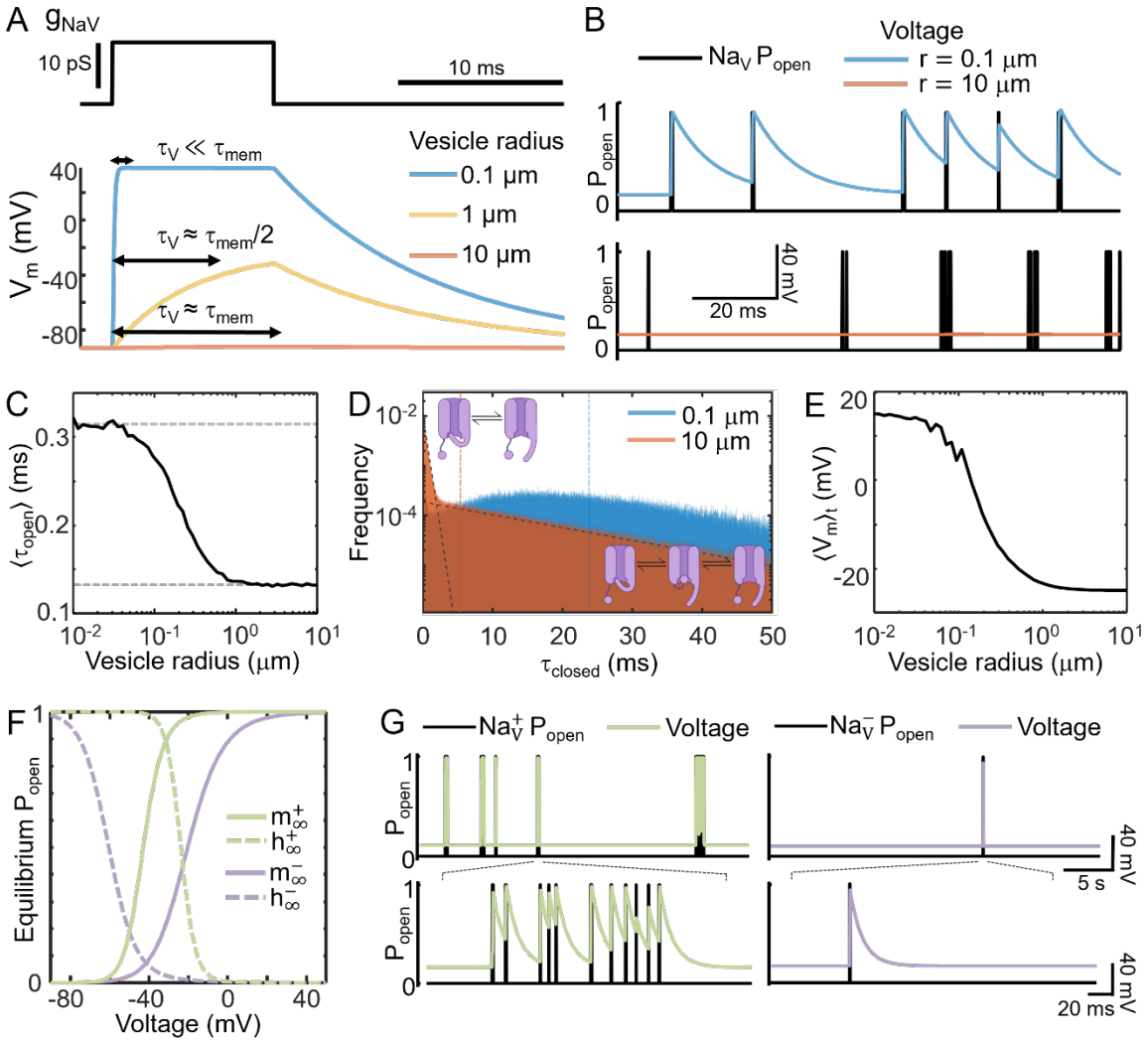

Figure 3.2 Reciprocal interactions between single-channel gating and V_m fluctuations in small compartments. *(caption on next page)*

(*Figure 3.2 continued)*

Figure 3.2 Reciprocal interactions between single-channel gating and V_m fluctuations in small compartments.

A. Simulated V_m in response to a single Na_V channel opening in vesicles of varying size. τ_V is the time constant of the voltage response when the channel is open; τ_{mem} is the intrinsic membrane time constant (when the channel is closed). **B**. Spontaneous Na_V gating (black) and V_m for $r = 10\ \mu m\ (\text{orange})$ and $r = 0.1\ \mu m$ (blue). Leak reversal potential, $E_{Leak} = -25$ mV. **C**. Mean Na_V open-state dwell time as a function of vesicle radius; average of $n = 10^4$ simulations of a Na_V channel initialized in the open state with $V_m(t = 0) = E_{Leak}$. Dashed lines show open-state dwell time when V_m is clamped at $V_m = E_{Leak}$ (bottom) and $V_m = E_{Na}$ (top). **D**. Closed-state dwell time histograms for voltage trajectories in vesicles with $r = 10\ \mu m$ and $0.1\ \mu m$, calculated as in B; simulations 5,000 s. Black dashed lines indicate linear fits to the fast $\tau_{closed}^{short} = 0.47 \pm 0.01$ ms (95% confidence) and slow $\tau_{closed}^{long} = 17 \pm 0.07$ ms (95% confidence) closed state dwell times for the $r = 10\ \mu m$ vesicle. Orange and blue vertical lines indicate mean τ_{closed} for $r = 10\ \mu m\ (5.4 \pm 12\ ms)$ and $0.1\ \mu m\ (24 \pm 19\ ms)$ vesicles (mean $\pm$ std). **E**. Time-average membrane voltage during spontaneous single-channel gating trajectories as in B. Each data point is an average of five 50 s-long simulations. **F**. Steady-state activation (solid trace) and inactivation (dashed) curves for a Na_V model with a large window current (Na_V^+, light green) and a Na_V model with a small window current (Na_V^-, light purple). **G**. Spontaneous Na_V gating (black) and V_m for the Na_V^+ model (left, light green) and the Na_V^- model (right, light purple) in F, for $r = 0.1\ \mu m$ vesicles at $E_{Leak} = -60$ mV. The Na_V^+ model voltage chatters between epochs of high-frequency oscillation and quiescent epochs.

3.4.1.2 Single-channel perturbations to concentration

Stochastic channel gating can also affect the ionic contents of the vesicle. To change the membrane voltage by an amount ΔV requires a flux of charge $\Delta Q = C\Delta V$. The ions carrying this charge flow into an internal volume M. Thus, the change in concentration, $\Delta\Gamma = C\Delta V/(z\,F\,M)$, where z is the valence of the charge carrier and F is the Faraday constant. For a spherical vesicle of radius r, we have $C \propto r^2$ while $M \propto r^3$, so $\Delta\Gamma \propto 1/r$, i.e. for a given voltage swing, changes in internal concentration are bigger for smaller vesicles. Numerically, the change in concentration is $\Delta\Gamma = 3.1 \times 10^{-4}\,\Delta V/z\,r$, where V is measured in mV, r in microns, and Γ in mM. For an r = 0.1 μm vesicle with a voltage swing ΔV = 100 mV, the change in concentration due to charging is ~0.3 mM/z, likely important only for Ca^{2+}.

This estimate misses an important factor, however. Simultaneous opening of channels with different reversal potentials leads to steady-state ionic flows. Net current can be approximately zero (so $dV/dt \approx 0$), while distinct ionic species maintain equal and opposite flows, e.g. via balanced Na^+ influx and K^+ efflux, leading to substantial changes in concentration.

In Appendix B.1 we analyze this scenario for a persistent Na^+ current combined with a leak conductance. We assume that voltage equilibrates fast compared to $[Na^+]_{in}$. This assumption then leads to a rate of change of $[Na^+]_{in}$ is proportional to the difference in reversal potential between Na^+ and the leak:

$$\frac{d[\mathrm{Na}^+]_{\mathrm{in}}}{dt} = \left(\frac{g_{\mathrm{Na}}g_{\mathrm{Leak}}}{g_{\mathrm{Na}}+g_{\mathrm{Leak}}}\right)\frac{1}{MzF}\,(E_{\mathrm{Na}}(t) - E_{\mathrm{Leak}}(t)). \qquad 3.17$$

Where $E_{Na}(t)$ and $E_{Leak}(t)$ are instantaneous values of the Na^+ and leak reversal potentials, respectively.

The steady-state $[\mathrm{Na}^+]_{\mathrm{in}}$ is reached when $E_{\mathrm{Na}}(t) = E_{\mathrm{Leak}}(t)$. Imposing electroneutrality, i.e. $\frac{d[\mathrm{Na}^+]_{\mathrm{in}}}{dt} = -\frac{d[\mathrm{X}]_{\mathrm{in}}}{dt}$, where $[X]_{in}$ is the concentration of the counterion carried by the leak conductance (e.g. Cl^- or K^+), the steady-state value of $[\mathrm{Na}^+]_{\mathrm{in}}$ is:

$$[\mathrm{Na}^+]_{\mathrm{in}}(\infty) = [\mathrm{Na}^+]_{\mathrm{in}}(0) + \frac{[\mathrm{Na}^+]_{\mathrm{ext}}[\mathrm{X}]_{\mathrm{in}}(0) - [\mathrm{X}]_{\mathrm{ext}}[\mathrm{Na}^+]_{\mathrm{in}}(0)}{[\mathrm{Na}^+]_{\mathrm{ext}}+[\mathrm{X}]_{\mathrm{ext}}}, \qquad 3.18$$

where $[X]_{in}(0)$ and $[Na^+]_{in}(0)$ are initial internal concentrations of ions. The external concentrations of ions, $[Na^+]_{ext}$ and $[X]_{ext}$ are assumed to be fixed. From Eq. 3.17, we derive the characteristic timescale of changes in $[\mathrm{Na}^+]_{\mathrm{in}}$:

$$\tau_{\mathrm{conc}} = MzF\,\frac{(g_{\mathrm{Na}}+g_{\mathrm{Leak}})}{g_{\mathrm{Na}}g_{\mathrm{Leak}}}\left(\frac{[\mathrm{Na}^+]_{\mathrm{in}}(\infty) - [\mathrm{Na}^+]_{\mathrm{in}}(0)}{E_{\mathrm{Na}}(0) - E_{\mathrm{Leak}}(0)}\right), \qquad 3.19$$

where $E_{Na}(0)$ and $E_{Leak}(0)$ are the initial values of the Na^+ and leak reversal potentials, respectively.

Let us consider the case where a single Na_V channel ($g_{Na_V} = 14$ pS, E_{Na} = 40 mV) and a single K_V channel (e.g. a delayed rectifier K^+ channel, $g_{K_V} = 20$ pS, E_K = -90 mV) are open simultaneously. Then the initial steady-state voltage is -36 mV, the initial steady-state Na^+ current is I_{Na} = -1.1 pA and the initial steady-state K^+ current is I_K = +1.1 pA. In a 1 mm diameter vesicle, these currents correspond to $\frac{d[Na^+]_{in}}{dt} =$ 21 mM/s. In a 0.1 □m diameter vesicle, $\frac{d[Na^+]_{in}}{dt}$ is 1000-fold higher, i.e. 21 mM/ms. Thus, a millisecond-duration flicker comprising counter-propagating ionic currents can substantially change the ionic content of a small compartment. **Figure 3.3 A** shows an example of $[Na^+]_{in}$ dynamics resulting from a charging current $\left(I_{Na} = -C_M \frac{dV}{dt}\right)$ and a persistent current $\left(I_{Na} = -C_M \frac{dV}{dt} - I_K\right)$ during Na_V and K_V gating in a small vesicle**.**

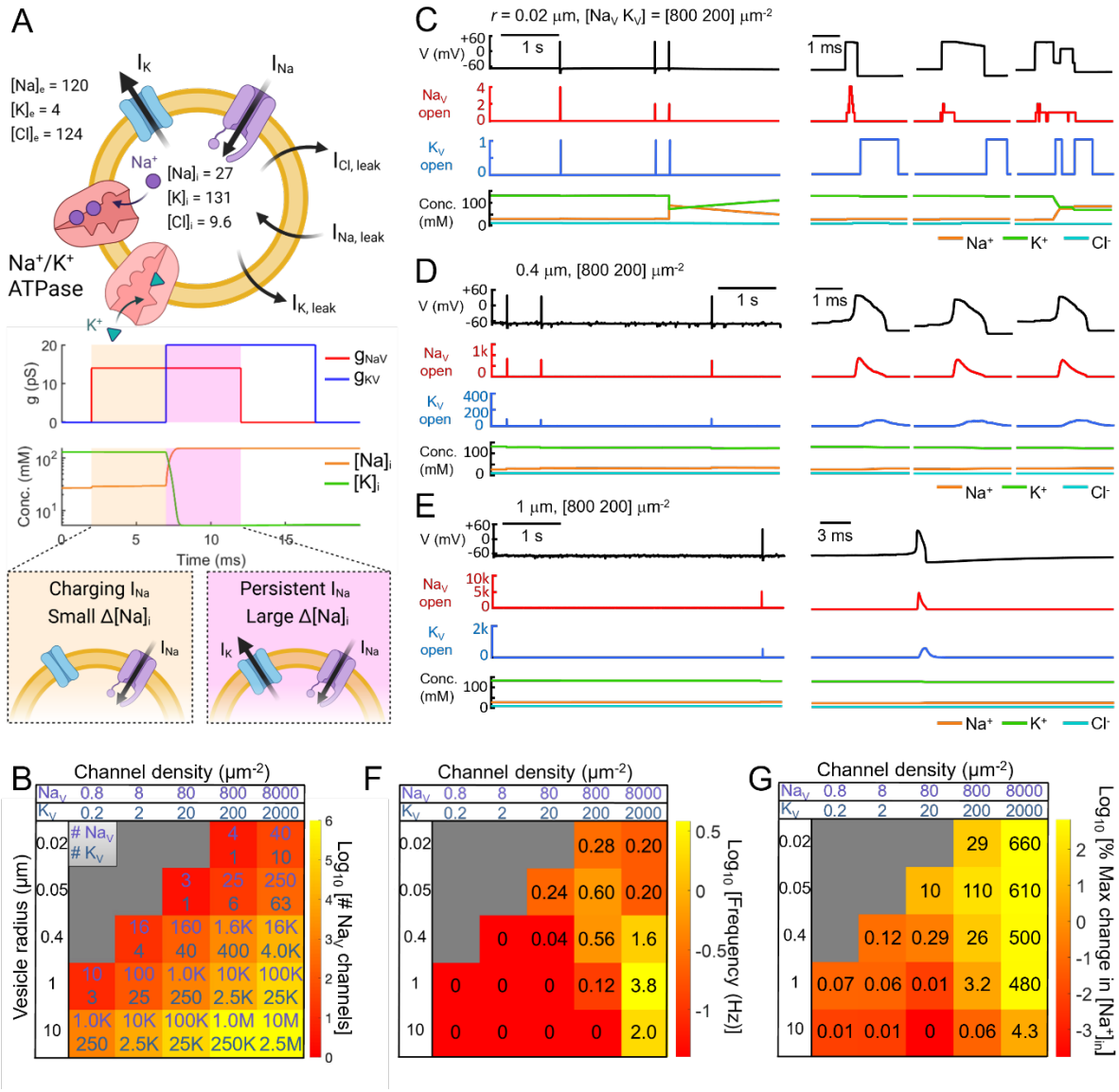

Figure 3.3 Spontaneous voltage dynamics in small compartments. *(caption on next page)*

(***Figure 3.3*** *continued)*

Figure 3.3. Spontaneous voltage dynamics in small compartments. Voltage and ion concentration dynamics were simulated in vesicles with different sizes and channel densities. **A**. Top: Model vesicle with HH-type conductances and Na^+/K^+-ATPase. All concentrations in mM. Beige panels: Activation of an individual Na_V channel does not appreciably change internal [Na^+]. Pink panels: Concurrent Na_V and K_V activation depletes [Na^+] and [K^+] concentration gradients until the Na^+ and K^+ reversal potentials become equal. Plots are for an $r = 0.02\ \mu m$ vesicle. **B**. Range of vesicle sizes and channel densities investigated. Gray regions correspond to size and density combinations with less than one K_V channel per vesicle. **C**. Left: 5 s simulation of a vesicle with r = 0.02 μm and [Na_V, K_V] = [800, 200] μm^2, corresponding to 4 Na_V channels and 1 K_V channel. Right: close-up of the three spontaneous events. In the third event, Na_V and K_V channel activation overlapped in time, leading to partial dissipation of the ionic gradients. **D**. Left: 5 s simulation of a vesicle with r = 0.4 μm and [Na_V, K_V] = [800 200] μm^2, corresponding to 1,600 Na_V channels and 400 K_V channels. Overlapping spontaneous Na_V activations were sufficient to trigger well-defined spikes. Changes in internal ionic composition were small, on account of the larger vesicle size compared to C. **E**. 5 s simulation of a vesicle with r = 1 μm and [Na_V, K_V] = [800 200] μm^2, corresponding to 10,000 Na_V and 2,500 K_V channels. Due to the larger vesicle size, the influence of each gating event diminished compared to the vesicle in D. Channel noise led to small fluctuations in baseline voltage, which occasionally triggered spontaneous spikes. **F** Color map of average spontaneous spiking frequency as a function of vesicle radius and channel density. **G** Color map of the average percent amplitude of internal [Na^+] concentration changes as a function of vesicle radius and channel density. These fluctuations were driven by overlapping Na_V and K_V currents. Data in F and G are the mean of five, 5 s simulations, excluding the r = 10 μm and [Na_V, K_V] = [8000 2000] μm^2 vesicle, which was simulated for 500 ms due to computational constraints.

3.4.2 Electrophysiology in Hodgkin-Huxley-type model vesicles

Next, we explore how ion channel stochasticity, self-action on membrane voltage, and ion concentration dynamics interact to influence electrophysiology in small compartments. We modeled small spherical vesicles with variable densities of Hodgkin-Huxley (HH)-type Na_V and K_V channels (**Figure 3.3 A**, Section 3.3 Methods). For biologically plausible vesicle sizes and channel densities, channel numbers vary by ~7 orders of magnitude (**Figure 3.3 B**). To restore ionic gradients, we added a Na^+/K^+-ATPase with a biophysically realistic Na^+ and K^+ concentration-dependent pumping rate [160,184]. We added Na^+, K^+, and Cl^- leak conductances to set a resting potential of -68 mV. The Na^+/K^+-ATPase and the leaks were proportional to the membrane area and deterministic. We simulated voltage and concentration dynamics, comparing deterministic and probabilistic Markov models of Na_V and K_V channel gating (Section 3.3 Methods). In all simulations we treated internal ion concentrations as dynamic and external ion concentrations as approximately constant.

3.4.2.1 Spontaneous activity

We simulated trajectories of spontaneous Na_V and K_V channel gating. As expected, the deterministic simulations produced no spontaneous activity, since both Na_V and K_V channels remained closed at the resting membrane potential, -68 mV. In stochastic simulations however, Na_V and K_V channels occasionally fluctuated to the open state. The consequences of these fluctuations depended on vesicle size and channel density.

In small vesicles ($r < 100$ nm), a single Na_V channel opening could depolarize the vesicle enough to activate other Na_V channels, leading to a spike (**Figure 3.3 C**). The spike waveforms were highly variable, due to the strong contributions of discrete channel gating events. During some spikes the Na_V and K_V currents overlapped, driving rapid ion gradient depletion (**Figure 3.3 C**, inset, right panel). The amount of ion gradient depletion depended on the overlap of the Na_V and K_V open times. Smaller vesicles supported longer Na_V channel openings due to voltage self-action (**Figure 3.2 C**) and higher channel densities created more opportunity for Na_V and K_V overlap. This gradient depletion caused a long-lasting decrease in vesicle excitability, restored eventually by the activity of the Na^+/K^+-ATPase (we assume a constant supply of ATP). This depletion-mediated refractory period is distinct from a typical refractory

period associated with ion channel recovery kinetics. Gradient depletion diminished spontaneous spike frequency at high channel densities (**Figure 3.3 F-G**, right column).

In larger vesicles ($100\ \mathrm{nm} < r < 1$ mm), single-channel events typically induced subthreshold depolarization (Na_V) and hyperpolarization (K_V). As channel density increased, these independent single-channel events began to overlap in time, leading to voltage dynamics that resembled an Ornstein-Uhlenbeck process, i.e. diffusion in a parabolic potential. This scenario has previously been studied analytically [170] and numerically [171]. When the biased random walk of voltage approached the Na_V activation potential, it triggered spikes which resembled classical action potentials (**Figure 3.3 D-E**). The frequency of these events has been modeled as a Kramers escape process [170].

At constant channel density, the spontaneous firing rate showed a non-monotonic dependence on vesicle size (**Figure 3.3 F**). For small vesicles, an increase in size led to an increase in the number of channels. Since a single stochastic channel gating event was sufficient to trigger a spike, more channels led to a higher spontaneous spike rate. For large vesicles, the influence of single-channel gating events on membrane voltage decreased, so spontaneous spikes became less frequent. This non-monotonic trend is similar to results of numerical simulations by Skaugen and Walløe [171]. The largest vesicles (r > 1 μm) were quiescent at all but the highest channel densities.

3.4.2.2 Evoked activity

We next simulated voltage trajectories in response to constant current injection. To mimic the effect of an electrogenic pump (optogenetic or chemically driven), we made the current proportional to membrane area ($I \approx 2.4 \times 10^3\ \mathrm{fA}/\mu\mathrm{m}^2$). We generated voltage trajectories using both stochastic and deterministic (i.e. HH-like) simulations of channel gating with dynamic internal ion concentrations.

When the number of channels was small, discrete gating events led to substantial deviations between the deterministic and stochastic simulations. Stochastic gating events could lead to spontaneous recovery from depolarization block (**Figure 3.4 A**), and converted regular spike trains into irregular trains (**Figure 3.4 B**). As channel number increased, stochastic trajectories came to resemble deterministic trajectories of the same vesicle (**Figure 3.4 C**). We quantified the similarity between voltage traces for deterministic vs. stochastic simulations via root-mean-square deviation (rmsd) between the autocorrelation functions of the two voltage trajectories (Section 3.3 Methods). **Figure 3.4 D** shows the

similarity between deterministic and stochastic simulations as a function of vesicle size and channel density.

We quantified the extent of internal ion concentration changes in the stochastic simulations. The ion gradients were more prone to depletion when the vesicle was smaller and the channel density was higher, as in the simulations in the absence of current injection (**Figure 3.4 E** and **Figure 3.3 G**).

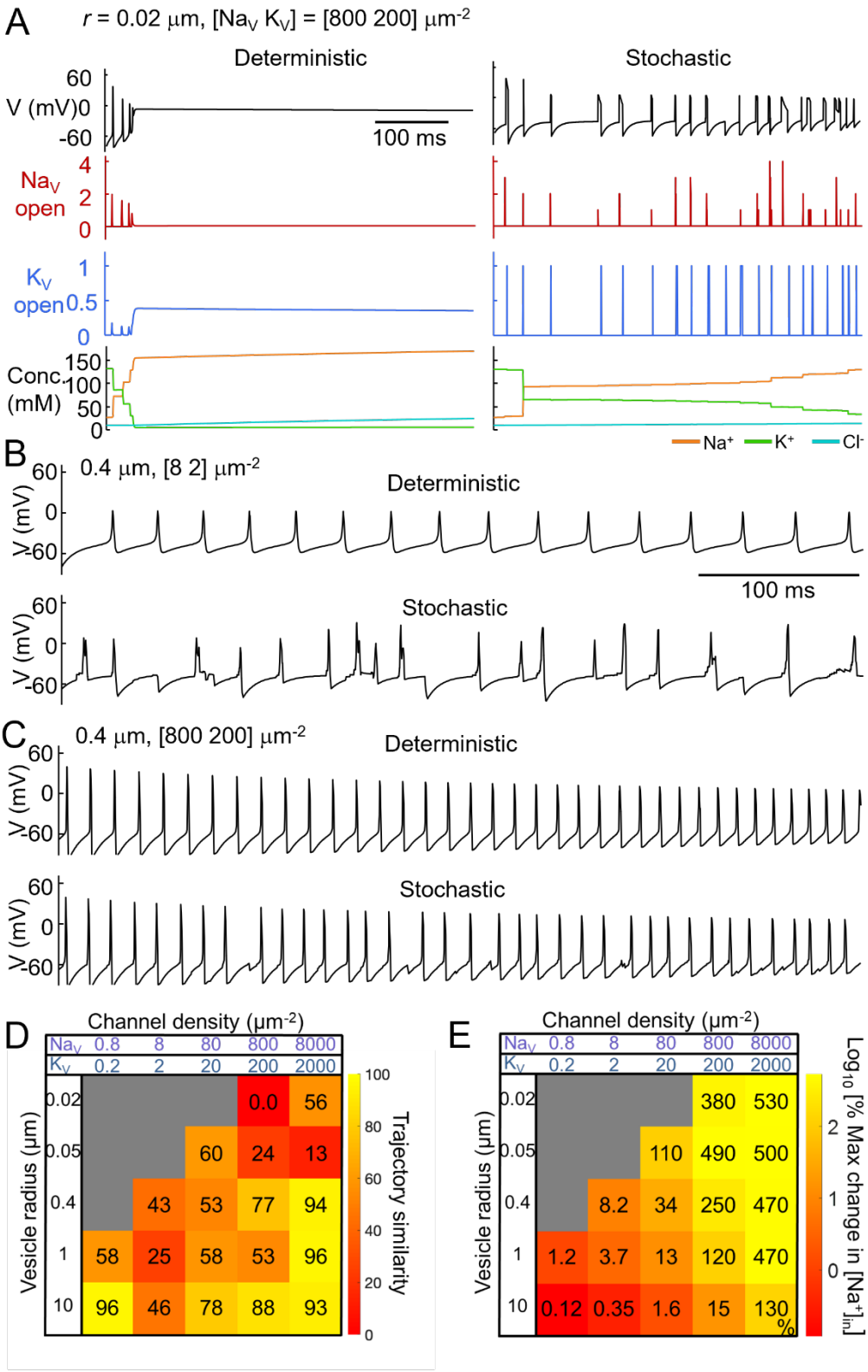

Figure 3.4 Driven voltage dynamics in small compartments. *(caption on next page)*

(*Figure 3.4 continued)*

Figure 3.4. Driven voltage dynamics in small compartments. Simulations were performed as in **Figure 3.3**, with the addition of a constant inward current density (Section 3.3 Methods). **A**. At the smallest vesicle size, the deterministic simulation (left) quickly entered depolarization block. In the stochastic simulations (right), fluctuations in channel gating restored the voltage from depolarization block, leading to sustained, but erratic, spiking. **B**. In an r = 0.4 μm vesicle with low channel density, the evoked spikes were variable in waveform due to stochastic variations in the number and timing of channel opening. **C**. In an r = 0.4 μm vesicle with higher channel density, stochastic channel fluctuations caused spike timing to be more variable than in deterministic simulations. **D**. Color map of the similarity between stochastic and deterministic responses to current injection, as measured by cross-correlation (Section 3.3 Methods). In the gray region, there is less than one K_V channel. **E**. Color map of the percent amplitude of internal [Na^+] concentration changes as a function of vesicle radius and channel density. Data in D and E are from one, 5 s simulation, excluding the r = 10 μm and [Na_V, K_V] = [8000 2000] μm^2 vesicle, which was simulated for 500 ms.

3.4.3 $Na_V1.5$ channels and endosome acidification

Finally, we modeled the effects of small-scale electrophysiology on macrophage endosome acidification. This acidification is essential for killing of pathogens engulfed by phagocytosis. Macrophage endosomes express $Na_V1.5$, with C-terminus outside the lumen (inverted relative to $Na_V1.5$ on the cell membrane). The channel density in endosomes is not known [115], so we simulated vesicles with $Na_V1.5$ densities (ρ_{Na_V}) between 0 – 6400 μm^{-2}. We assumed radius r = 0.2 μm [176] (**Figure 3.5 A**), initial membrane potential +19 mV (inside relative to outside), initial pH 6.2, and initial internal Na^+ concentration 100 mM [180,185]. A v-ATPase imports H^+, acidifying the endosome during maturation [167,168], and ClC-7 contributes a small outward H^+ current [167]. The electrophysiological parameters and initial conditions are in **Table B.2**. The $Na_V1.5$ model is described in Appendix B.3. The endosomal $Na_V1.5$ model accounts for isoform-specific features, including greater steady-state inactivation at moderate to high voltages compared to the canonical HH Na_V model.

In deterministic simulations of endosomes with $\rho_{Na_V} = 6400\ \mu m^{-2}$, the mean number of open $Na_V1.5$ channels was always much less than 1. We rounded the Na_V conductance to the nearest integer (in units of the open-state conductance), which rounded to zero. Hence, the Na_V channels did not contribute to the deterministic simulations (**Figure 3.5 B**).

In stochastic simulations at $\rho_{Na_V} = 6400\ \mu m^{-2}$, the $Na_V1.5$ channels were mostly in the inactive state due to the "felt" voltage of -19 mV (outside relative to inside). Occasionally, a single $Na_V1.5$ channel fluctuated to the open state. In the $r = 0.2\ \mu m$ vesicle, this induced a decrease in membrane voltage (inside relative to outside) of ~21±16 mV (mean ± s.d.) since [Na^+] was higher inside the endosome than in the cytoplasm. The voltage dips recovered with time constant ~16±2.4 ms (mean ± s.d.). The voltage decrease enhanced v-ATPase activity and suppressed the outward H^+ current due to ClC-7 activity, speeding up acidification (**Figure 3.5 B**). The effect of $Na_V1.5$ activity on the acidification dynamics became more pronounced as $Na_V1.5$ channel density increased, since the fraction of time when there was one $Na_V1.5$ channel open was proportional to the number of $Na_V1.5$ channels present (**Figure 3.5 C**).

Figure 3.5 D shows endosomal pH change as a function of the density of $Na_V1.5$ channels. In the deterministic simulations, the acidification rate was unaffected by the presence of $Na_V1.5$, since the average number of open channels was approximately zero. In the stochastic simulations, however, the

acidification rate increased as $Na_V1.5$ channel density increased, due to the Na_V-induced membrane potential fluctuations. Thus, stochastic channel fluctuations are likely relevant to this important physiological process.

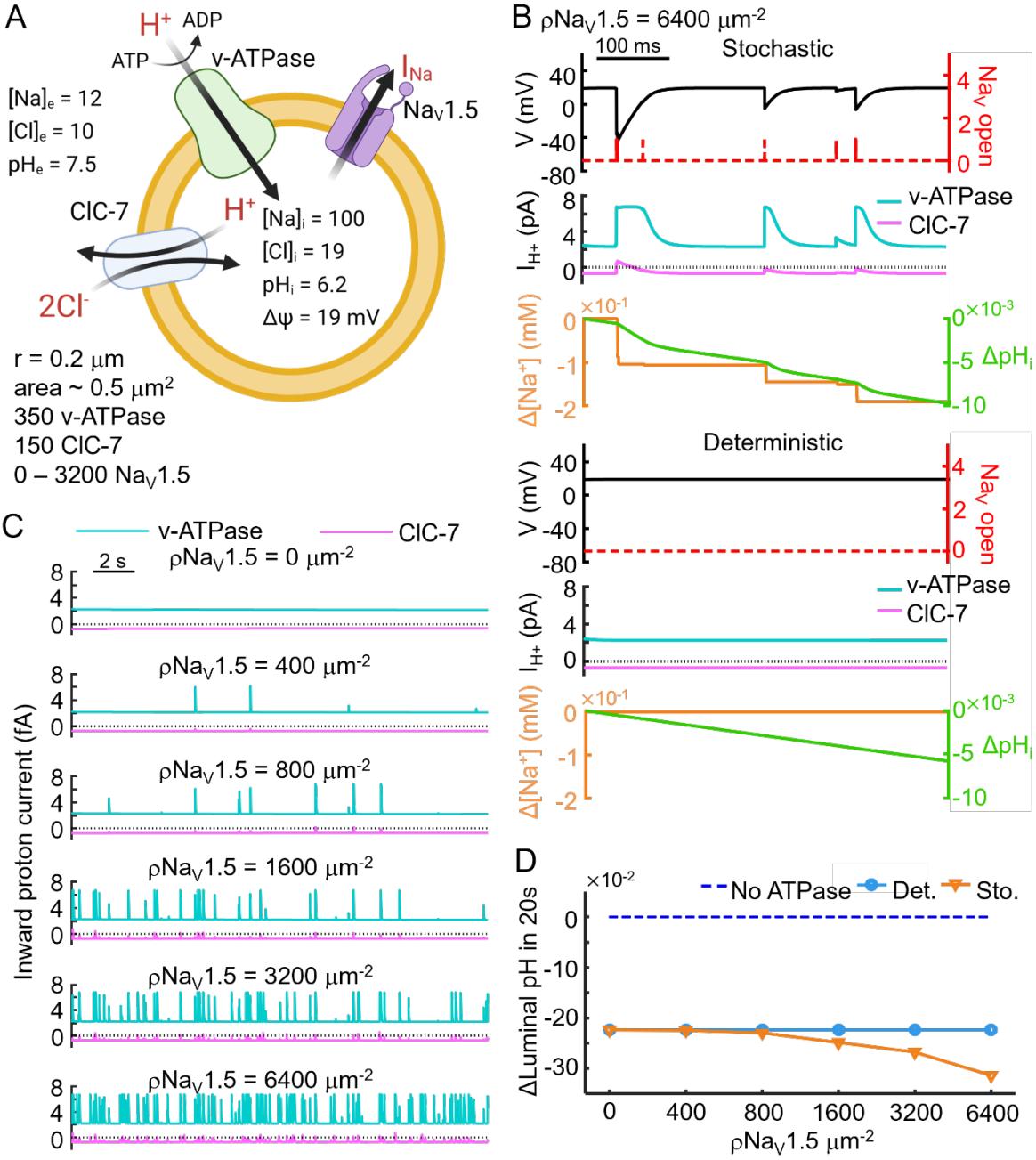

Figure 3.5. Stochastic simulations of endosome acidification dynamics.
A. Model endosome. Concentrations in mM. **B**. Comparison between the stochastic (top) and deterministic (bottom) dynamics. In the stochastic simulation, spontaneous $Na_V1.5$ fluctuations transiently decreased the membrane voltage and increased the acidification rate. **C**. The effect of $Na_V1.5$ activity on endosome acidification increased at higher $Na_V1.5$ density. **D**. Luminal pH in stochastic or deterministic simulations after 20 s, across a range of $Na_V1.5$ channel densities. The initial pH is shown as a dashed line.

3.5 Discussion

This work identifies a qualitative regime change in electrophysiology as membrane-enclosed compartments shrink to sub-micron dimensions. In this regime, (i) single-channel openings can drive large, rapid excursions in membrane potential, (ii) the resulting voltage changes feed back onto channel kinetics during the same opening event, and (iii) ionic currents—especially counter-propagating currents through different channel types—can measurably reshape intralumenal ion concentrations during single gating events. By combining Markov-state channel gating with self-consistent voltage dynamics and ion-concentration updates, we provide a unified framework that connects classical conductance-based descriptions to the single-molecule limit.

A central implication of our work is that small compartments need not behave like miniature versions of excitable cells. In the classical setting (large membrane area and many channels), channel noise is well captured as an approximately Gaussian perturbation around a mean conductance, enabling diffusion/Langevin and Kramers-type descriptions of rare excursions and spontaneous spikes [147,149–153,169–171]. In contrast, when channel copy numbers are in the single-digit to tens, and leak conductance and capacitance are correspondingly small, voltage trajectories are inherently jump-like: individual gating events can move V_{m} a substantial fraction of the way toward a reversal potential, and the ensuing self-action can prolong or curtail dwell times depending on the voltage-dependence of the transition rates. This feedback effectively endows the system with history dependence (“memory”) even when the underlying channel model is Markovian, and it can generate dynamics—such as intermittency or “chattering” in channels with appreciable window currents—that have no direct analog in larger systems.

A second implication concerns ionic homeostasis. In large cells, voltage dynamics are often computed with fixed reversal potentials (except for Ca^{2+}), and concentration dynamics enter only as slow modulators [156,157]. In small volumes, this separation can break down. Our simulations highlight a particularly important case: coincident opening of conductances with different reversal potentials can drive large counter-propagating ionic fluxes while producing little net capacitive current. This flux can rapidly dissipate Na^+/K^+ gradients, producing a depletion-mediated refractory period that is mechanistically distinct from classic refractoriness set by channel inactivation and recovery. This predicted mechanism suggests a plausible interpretation for recent organelle measurements, where endosome-to-endosome

variability in lumenal Na^+ and maturation-dependent Na^+ shifts are substantial [55], and where K^+ channel activity on trafficking organelles measurably changes lumenal K^+ [145]. In particular, our results motivate the hypothesis that some of the observed heterogeneity could arise from rare overlaps of channel openings that transiently reshape ionic gradients.

Our endosome simulations provide a complementary example of how discrete gating can matter even when the mean open probability is extremely small. For $Na_V1.5$ in macrophage late endosomes [115], the deterministic (mean-field) description can effectively "round away" the channel contribution when the expected number of open channels is $\ll 1$. The stochastic model, however, predicts that rare single-channel openings can generate transient voltage excursions that systematically bias electrogenic transport (v-ATPase, ClC-7), accelerating acidification. This points to a broader principle: in nanoscale compartments, physiological impact may be controlled by event statistics (amplitude, dwell-time distributions, and coincidence rates) rather than by ensemble- or time-averaged conductances.

These considerations suggest several experimentally testable predictions and design principles for organelle and microbial electrophysiology. First, voltage and ion measurements at single-organelle resolution [49,55,145] should exhibit non-Gaussian signatures—e.g., heavy-tailed distributions of voltage deflections and state-dependent dwell times—that become more distinct as compartments become smaller or channel copy number decreases. Second, simultaneous measurements of V_{m} and lumenal counterions (e.g. $[Na^+]$ or pH in endosomes) should reveal transient covariance consistent with counter-propagating flux episodes: large voltage events with disproportionately large concentration changes when multiple channel types overlap. Third, perturbations that change organelle size, channel abundance, or kinetics (e.g., channel blockers or mutants that modify window current) should shift systems between qualitatively distinct dynamical regimes in predictable ways, offering a path to infer otherwise inaccessible parameters such as channel copy number per organelle.

Several extensions could broaden the model's applicability. Many small compartments are not closed: dendritic spines, nodes of Ranvier, and subcellular invaginations exchange ions with a larger reservoir through narrow necks or diffusion-limited pathways [15,186,187]. Incorporating diffusive coupling to cytosol or extracellular space would allow the same framework to address when local ionic depletion is buffered by exchange versus when it becomes functionally consequential. Similarly, allowing external concentrations

to vary—important in crowded extracellular spaces where external volume fractions are small—would connect to activity-driven extracellular K^+ accumulation and spreading depolarization phenomena [188,189]. Finally, while we treated pumps and transporters deterministically, growing evidence indicates that ultraslow mode switching and static disorder can be intrinsic to transport proteins [10,11,30]. A fully stochastic treatment of pumps and exchangers, coupled to voltage and concentration dynamics, may be essential for quantitatively predicting organelle-to-organelle heterogeneity and intermittency.

More broadly, this work emphasizes that "channel noise" in small compartments can be a primary driver of state transitions and homeostatic set points. As optical electrophysiology and organelle-resolved ion sensing mature [49,55–57,125,145], theories that retain discreteness—single-molecule gating, finite copy numbers, and concentration-driven feedback—will be increasingly necessary for interpretation and for mechanistic inference from data.

3.6 Manuscript information

A version of this chapter is published to a preprint server[190]. Supporting information for this chapter is provided in Appendix B.

3.6.1 Acknowledgements

We thank Prof. Michael Grabe of UCSF for providing us with the Matlab code for the vesicle-type H^+ ATPase model. This work was supported by a NSF Graduate Research Fellowship (M.R.H.) and NSF Quantum Sensing for Biophysics and Bioengineering (QuBBe) Quantum leap challenge institute (QLCI) grant OMA-2121044. Components of **Fig 1-3**, **5** and **Note S2** were created in BioRender. Howell, M. (2025) https://BioRender.com/nm7zk94

3.6.2 Author Contributions

Madeleine R. Howell and Rosalind J. Xu performed the simulations. Rosalind J. Xu, Madeleine R. Howell, and Adam E. Cohen. wrote the manuscript. Adam E. Cohen envisioned and supervised this project.

4 Concluding Remarks

This dissertation explores single-molecule effects on electrolyte concentrations and voltage in nanoscale membrane compartments, both through the lens of method development for sensitive membrane transport measurements and towards predicting electrophysiology in native compartments.

In Chapter Two we develop a new paradigm for sensitive single-channel recordings using membrane tethers. We hypothesized that membrane tethers could amplify and isolate small substrate fluxes in the tether lumen. We found that membrane tethers (area ~1 μm^2) isolate a small number of channels from bulk membrane (expression density ~4 channels/μm^2). Tethers have subdiffraction-sized radii (radius ~50 nm), providing optical sectioning for fluorescence signals in the tether lumen. Diffusional confinement of transported Ca^{2+} in the quasi-1D tether lumen enabled the detection of small, spatially discrete Ca^{2+} signals using a membrane targeted GECI. The discrete and stochastic nature of this signal suggested that these events corresponded to single-channel openings. Voltage dependence of event occurrence corresponded to ensemble currents in the cell body. Estimates of steady-state buffering capacity (~1 free Ca^{2+} ion per 100-200 Ca^{2+} transported) and $Ca_V3.2$ unitary conductance (~2 pS) suggest that our tether recording paradigm was sensitive to ~0.4 fC of transported charge, which corresponds to as few as 6-13 molecules of free Ca^{2+}.

Our Ca^{2+} imaging in tethers suggests that concentration gradients may change significantly due to stochastic channel openings in native membrane tubes and analogous structures. Furthermore, while voltage changes due to electrogenic channel gating in tethers are expected to be minimal (see Appendix C.2) and tether voltage is expected to be well-clamped by the cell body, these assumptions do not hold in the nanoscopic, spherical vesicles such as synaptic vesicles and endocytic organelles.

In Chapter Three we explore, through simple scaling arguments and stochastic single-channel and ensemble simulations, the unique electrophysiology of nanoscopic vesicles. We find that when single-channel currents are larger than capacitive and leak currents, vesicle voltage can stochastically “jump” from its resting leak potential to the channel reversal potential. For small but physiological vesicle sizes, voltage equilibrates faster than channel state transition rates. Fast voltage equilibration changes apparent channel kinetics and dynamics. Furthermore, when stochastic channels carrying counter-propagating currents are incorporated into our simulations, we find that overlapping channel activation can deplete

ionic gradients. This leads to a distinct “refractory” mechanism controlled by the re-establishment of ion gradients through pumps. The following sections discuss extensions and limitations of this work.

4.1 Do single-channel recordings in tethers generalize to other integral proteins?

In Chapter Two we performed proof-of-concept using a low-conductance Ca^{2+} channel and a membrane-targeted genetically-encoded Ca^{2+} indicator. Yet, we have not experimentally tested the capability of this approach for measurement of non-electrogenic and low ($<<10^5$ molecules s^{-1}) flux regimes[20]. Here we discuss how this recording modality might generalize for different flux regimes while accounting for typical biosensor constraints.

Transport and turnover rates by integral membrane proteins vary by ~9 orders of magnitude, from <1 molecules s^{-1} for glutamate transporter isoform EAAT5 to ~10^7 ions s^{-1} for BK Ca^{2+}-activated K^+ channel[191,192]. Estimates for steady-state lumenal substrate concentration (Eq. 2.1) and substrate residence time in tethers (Eq. 2.2) constrain the binding affinity (i.e. K_D) and binding kinetics (i.e. k_{on}) of candidate substrate biosensors. **Table 4.1** lists several membrane transporter and sensor pairs which may be amenable to tether-based transport recordings. The transporters listed have been largely inaccessible to conventional single-unit electrical or optical recording techniques due to slow or electroneutral transport.

Several **pitfalls** may arise when trying to port conventional fluorescent sensors to tether-based measurements. First, sensors are engineered to be maximally sensitive to the magnitude and variance of substrate concentrations expected for a specific compartment, which may differ from the tether. For example, glutamate sensors are designed to respond to extracellular synaptic glutamate concentrations which peak at $[Glu]_{cleft}$ ~0.5-5 mM from resting $[Glu]_{cleft}$ ~1-5 μM. In contrast, basal intracellular $[Glu]_i$, can reach 5-10 mM in glutamatergic neurons.[193] Typical glutamate sensors may saturate at the $[Glu]_i$ of glutamatergic neuron-derived tethers (i.e. $K_D << [Glu]_i$) or lack the dynamic range to detect ~μM signals from single transporters on top of high background (i.e. $\Delta[Glu]_{tether} << K_D \approx [Glu]_I$) (**Table 4.1**). This can be managed by tether-based recordings in cell types with low basal $[Glu]_i$ (matched to sensor K_D) or pharmacological perturbation of glutamate export (e.g. stimulation with high extracellular cysteine)[194]. For heavily buffered substrates (e.g. Ca^{2+}, H^+), it is important to note that buffering in tethers likely differs from the cell body at least in part due to the lack of buffering organelles in tethers. From a concentration

standpoint, tether-based recordings are most practical when available sensor affinity is close to basal tether substrate concentration, $K_D \approx [\text{substrate}]_{tether}$, and single-transporter fluctuations are large, $\Delta[\text{substrate}]_{tether} \approx K_D$.

What transport parameters are measurable with tether-based recordings? To assess, we incorporate sensor binding into our model of Ca^{2+} transport in tethers (see also Appendix A.1). We make the simplifying assumptions that Ca^{2+} - sensor binding is a bimolecular reaction with on- and off-rate α and β, that endogenous Ca^{2+} buffering is fast, and neglect Ca^{2+} extrusion:

$$\frac{\partial[Ca^{2+}]_{free}}{\partial t} = D_{eff}\frac{\partial^2[Ca^{2+}]_{free}}{\partial x^2} + \delta_0(x)J_{Ch}(t) - \frac{\partial[CaG]}{\partial t} \quad 4.1$$

$$\frac{\partial[CaG]}{\partial t} = -\beta[CaG] + \alpha[Ca^{2+}]_{free}([G]_T - [CaG]) \quad 4.2$$

Where lumenal free Ca^{2+} concentration is $[Ca^{2+}]_{free}$, buffered Ca^{2+} diffusion coefficient is D_{eff} and the Ca^{2+} channel is treated as a point source, $\delta_0(x)$ of flux $J_{Ch}(t)$. Lumenal Ca^{2+}-bound sensor is $[CaG]$ and total bound and free sensor concentration is $[G]_T$.

Two competing timescales emerge. In the limit of fast diffusional equilibrium, the time resolution of single-channel flux, $J_{Ch}(t)$, is limited by sensor binding kinetics, e.g.:

$$\tau_S = \frac{1}{\beta + \alpha[Ca^{2+}]_{free}} \quad 4.3$$

In the limit of fast Ca^{2+}-sensor binding equilibrium, time resolution is limited by Ca^{2+} diffusional equilibrium, e.g. (Eq. 2.2).

$$\tau_D = \frac{L^2}{2D_{eff}} \quad 4.4$$

What are common $J_{Ch}(t)$ motifs? Transport rates may be constant in time (e.g. constant pump rate), vary between discrete states (e.g. open vs closed channel), or vary continuously. The quantity of interest may be the state-dependent transport rate (e.g. unitary open channel current), state dwell time (e.g. how long the channel is open) or both. How these quantities change with substrate concentration, membrane voltage, drugs etc. can provide insights on transporter gating, pharmacology, and affinity for substrate. Reporter kinetics must be compatible with the timescale of transporter dynamics as well as substrate residence time in the tether.

Under what conditions might tether recordings *average*, *integrate*, or *exactly report* transporter rate over time? High fidelity measurements of transport rate may be feasible when the characteristic timescale of transporter transitions, $\tau_{Ch} \gg \max(\tau_S, \tau_D)$ where τ_S and τ_D are the substrate – sensor equilibration time and diffusional equilibration time, respectively. Transport rates may be integrated over diffusion timescales when $\tau_S \ll \tau_{Ch} < \tau_D$ or over binding timescales when $\tau_D \ll \tau_{Ch} < \tau_S$. Finally, transport rates may be averaged over many state transitions or across multiple transporters when $\tau_{Ch} \ll \min(\tau_S, \tau_D)$ or when signals from multiple transporters overlap in space or time. In such cases, noise analysis of tether fluorescence may enable the recovery of time- or subpopulation-averaged kinetic parameters.

Sensor kinetics were too slow to resolve fast channel flickers in our Ca$_V$3.2 recordings, reporting instead the relative cumulative charge passed during voltage stimulus. Despite simultaneous current and Ca^{2+} sensor measurements at the cell body, we could not convert tether Ca^{2+} signal to free Ca^{2+}, likely due to differences in Ca^{2+} handling between compartments. Quantitative measurement of Ca^{2+} flux would require a calibrated reporter of Ca^{2+} and knowledge of endogenous buffering. Furthermore, without *a priori* knowledge of channel gating (e.g. voltage-dependent unitary conductance) it would not be possible to disentangle changes in channel open time from altered channel conductance with a slow sensor.

Brighter, faster, and more sensitive biosensors are continually developed. Improved and calibrated sensors will benefit this recording modality.

Table 4.1 Properties of select integral proteins and biosensors of their substrates

Integral protein	Transport stoichiometry	Basal [Substrate]	Transport rate φ	D_{eff} (μm^2 s^{-1})	Max. substrate Δc in tether	Residence time (s)	Candidate sensor	Ref.
Plasma membrane glutamate transporter (*EAAT*)	Secondary active *imports:* 3 Na^+ 1 H^+ 1 glutamate (Glu^-) *exports:* 1 K^+	Basal cytosolic: $[Glu]_i$ ~ 5-10 mM* $[Na^+]_i$ ~ 30 mM $[H^+]_i$ ~ pH 7.2 or 60 nM $[K^+]_i$ ~ 130 mM	1 – 100 cycles s^{-1} *imports:* ~1-100 H^+ s^{-1}, Glu s^{-1} ~3 – 300 Na^+ s^{-1} *exports:* ~ 1-100 K^+ s^{-1}	ND ~200 (Glu)‡ ~140 (H^+) ~700 (Na^+) ~1200 (K^+)	10 nM – 1 μM (Glu) 15 nM - 1.5 μM (total H^+) <50 pM (free H^+) 10 nM – 1 μM (Na^+) < 200 nM (K^+)	250 ms (Glu) 360 ms (H^+) 70 ms (Na^+) 40 ms (K^+)	High-affinity iGluSnFR variants, if $[Glu]_I$ can be decreased, e.g. iGluSnFR4f K_D = 22 μM τ_{off} = 26 ms	37,160,195–198
Plasma membrane Ca^{2+}-ATPase (*PMCA*)	Active transport; Hydrolysis of 1 ATP *imports:* 2 H^+ *exports*: 1 Ca^{2+}	Basal cytosolic: $[H^+]$ ~ pH 7.2 or 60 nM	100 – 10000 H^+ s^{-1} Assuming β = 5 mM/pH ~3×10^{-3} – 0.3 free H^+ ions s^{-1}	~140 (H^+)	50 pM – 5 nM i.e. pH ~7.2 – 7.17	360 ms	downward going sepHluorin signal: pK_a ~7.1	195,197,199,200
Channelrhodopsin2 (*ChR2*)	Ion channel: Unitary conductance: 3×10^4 ions s^{-1} 1% Ca^{2+} permeability	Basal cytosolic: $[Ca^{2+}]$ ~ 100 nM	~300 Ca^{2+} s^{-1} Assuming κ_{Ca} ~100-200 ~1.5 – 3 free Ca^{2+}s^{-1}	~20 (Ca^{2+})	150 nM – 300 nM	2.5 s	GCaMP8f K_D = 330 nM τ_{off} = 19 ms	42,89,104,201,202

*in glutamatergic neurons.

‡ND, 200 μm^2 s^{-1} is an estimate for glutamate diffusion in the synaptic cleft[203]

κ_{Ca} is Ca^{2+} buffering capacity

β is pH buffering capacity

4.2 Extensions and limitations of tether-based recordings

4.2.1 Cell-regulatory control of single transporters

Integral membrane proteins are subject to many posttranslational regulatory controls, including phosphorylation, redox modifications, and glycosylation, as well as allosteric interactions with nearby proteins and lipids[204,205]. These regulatory controls are difficult to reconstitute in *in vitro* systems. A potential capability of *in cellulo* tether-based recordings is the ability to directly interrogate perturbations to transporter biophysics downstream of native signaling pathways. For example, D_1R dopamine receptor activation releases G-protein $\beta_2\gamma_2$ subunit which binds to and decreases $Ca_V3.2$-mediated Ca^{2+} conductance in bulk flux assays[206]. This decrease is not caused by changes in channel expression or voltage dependence of gating. Our $Ca_V3.2$ tether recordings do not have the time resolution to discriminate between a change in state dwell time (i.e. shorter channel openings) or through a change in unitary conductance. However, our $Ca_V3.2$ tether recordings could indicate whether this effect is caused by block of a subset of channels based on the difference in Ca^{2+} event statistics before and after D_1R activation. In theory, tether-based transport measurements before and after stimulation of an intracellular signaling pathway (e.g. by receptor activation, metabolic perturbation, voltage, etc.) may help to elucidate regulatory mechanisms.

Physical forces can also tune the conformational dynamics and spatial localization of integral membrane proteins. Recent work shows that both canonically mechanosensitive channels (e.g. Piezo1[101]) and non-mechanosensitive integral proteins[207,208] are enriched in membranes of particular curvatures. This suggests that membrane curvature may bias the complement of proteins which can be isolated for tether-based recordings. In our recordings of $Ca_V3.2$ in tethers, however, we observed no correlation between tether radii and channel density[112] and suspect that higher-order effects, such as lack of cytoskeleton in tethers[84], may be responsible for differences in tether and cell body channel density. Curvature can also bias channel gating[66]. In our $Ca_V3.2$ recordings, however, the voltage dependence of channel events mirrored that recorded in the cell body. If tether radii can be systematically varied, then the curvature dependence of transport could be measured. Such control may be achieved by extracting tethers from membrane blebs under different osmotic conditions[101].

4.2.2 Membrane tethers as minimal models of signaling organelles

Cell membranes natively adopt tether-like structures including primary cilia, dendritic spines, filopodia, and tunneling nanotubes. Why are membrane tubes a recurring structural motif in these sensory compartments? Studies of membrane tethers as a minimal model can help to distinguish passive geometric contributions to signaling (e.g. large surface area to volume ratio, small lumenal volume, diffusional confinement, gradient depletion, electrotonic length constants, curvature-mediated trafficking) from active tuning of biochemical constituents (e.g. density and type of integral proteins, lumenal buffers, selectivity filters etc.) For example, our work demonstrates that Ca^{2+} channels in tethers can cause large local Ca^{2+} amplification due to diffusional confinement alone. Primary cilia possess a similar geometry to tethers but achieve signal amplification through an orders of magnitude greater abundance of effector proteins (e.g. substrate import/export and buffers) over their soluble signaling substrates (e.g. Ca^{2+}, cAMP, etc.)[19,209]. Thus, they remain highly sensitive and robust to noise.

How do buffering (e.g. affinity, kinetics and mobility) and compartmentalization interact to shape ciliary Ca^{2+} signaling? Tether-based recording of Ca^{2+} signal propagation from ciliary Ca^{2+} channels in which buffer parameters and tether radii are systematically varied can help to answer this question. This could be accomplished by loading cells with well-characterized exogenous buffers (e.g. BAPTA, EGTA, etc.) or titrating expression and localization of endogenous buffers (e.g. parvalbumins, calbindins, and calretinin)[89]. The Ca^{2+} sensor used would need to be carefully titrated to ensure sensor buffering is negligible. To understand how the filtered Ca^{2+} signal is interpreted by ciliary signaling pathways, one could reconstitute a minimal ciliary Ca^{2+} signaling pathway in membrane tethers (e.g. ciliary TRP channel opens and [Ca]↑, Ca^{2+} inhibits adenylate cyclases and [cAMP]↓)[209,210] and readout fluctuations of downstream signaling molecules (e.g. [cAMP]) using fluorescent biosensors.

4.2.3 Fluorescence correlation measurements of low-affinity binding

A challenge to many single molecule techniques is background suppression. Fluorescence correlation and cross-correlation spectroscopy (FCS/FCCS) rely on dilute biomolecule density and small confocal volumes to remain in a regime where fluorescence fluctuations are large relative to the mean signal. Typically, a tradeoff exists between biomolecule observation time, which is set by diffusion time across the smallest focal volume dimension, and biomolecule density (i.e. mean signal). The concentration limit in a

typical FCS-like experiment is ~10 nM[211]. Resolving binding interactions (e.g. via dwell time of a fluorescently labeled substrate) is thus only feasible for high-affinity interactions. Yet many enzymes have K_M in the μM to mM regime. Tether lumen volume can be much smaller than a typical ~1 fL confocal volume, yet the residence time scales according to tether length, L^2 rather than confocal radius, r^2 (e.g. $\frac{L^2}{2D} \gg \frac{r^2}{6D}$). Diffusional slowdown in tethers permits long observation windows, and the small luminal volume ensures that fluctuations dominate mean biomolecule occupancy. For example, a substrate concentration of ~1 μM corresponds to only ~60 molecules in a 0.1 fL tether. To test this, one could load cells with known concentrations, c, of diffusible fluorescent tracers, pull tethers and calculate the autocorrelation function of tether fluorescence. For reasonable substrate concentrations, the amplitude of the ACF at zero time lag, $G(0) \propto \frac{1}{c}$.

4.3 Voltage in vesicles, tethers, and intermediate geometries

Our work in Chapters Two and Three shows that voltage dynamics differ substantially in voltage-clamped membrane tethers and isolated vesicles. In Appendix C.1 we show that, despite their small diameter, membrane tethers are electrotonically close to cell bodies (e.g. tether length $l \ll \lambda$, electrotonic length constant) so that tether voltage is clamped by the cell body. These estimates of electrical coupling are supported by our observation of similar voltage-dependent $Ca_V3.2$ gating in cell bodies and tethers. In contrast, electrically isolated vesicles can undergo large and fast voltage fluctuations which feedback on channel gating. Recent work suggests that primary cilia[210] and dendritic spines[187] can escape voltage clamp from their parent compartments despite sharing structural similarities to membrane tethers. In Appendix C.2 we attempt to rationalize these findings, using simple equivalent circuits to show that high resistance junctions (e.g. narrow spine neck or cilia selectivity filter) and steady-state differences in compartment reversal potential or local currents can drive voltage offsets in tether-like compartments.

A second distinction between model vesicles and membrane tethers arises from spatial gradients of electrolytes. Our calculations of substrate transport in tethers suggest that spatial gradients of substrate can be substantial and slow to dissipate $\sim \frac{L^2}{2D}$ in the tether lumen. In contrast, spatial gradients in spherical vesicles will equilibrate fast $\sim \frac{r^2}{6D}$ so substrate concentrations are assumed to be homogeneous. A consequence is that tether voltage can remain clamped by the cell body but tether transporters can

experience local fluctuations in chemical driving force (e.g. reversal potential) that curtail substrate flux. This “self-action” will have a greater effect on unbuffered substrates. For example, lumenal Ca^{2+} changes were highly buffered in our $Ca_V3.2$ recordings, resulting in little free Ca^{2+} to change Ca^{2+} reversal potential.

Bibliography

1. Satchwell, T. J. & Toye, A. M. Band 3, an essential red blood cell hub of activity. *Haematologica* **106**, 2792–2793 (2021).

2. Nenasheva, T. A. *et al.* Abundance, distribution, mobility and oligomeric state of M2 muscarinic acetylcholine receptors in live cardiac muscle. *J. Mol. Cell. Cardiol.* **57**, 129–136 (2013).

3. Jung, C. Y. Permeability of bimolecular membranes made from lipid extracts of human red cell ghosts to sugars. *J. Membr. Biol.* **5**, 200–214 (1971).

4. Mutch, S. A. *et al.* Protein Quantification at the Single Vesicle Level Reveals That a Subset of Synaptic Vesicle Proteins Are Trafficked with High Precision. *J. Neurosci.* **31**, 1461–1470 (2011).

5. Sabatini, B. L. & Svoboda, K. Analysis of calcium channels in single spines using optical fluctuation analysis. *Nature* **408**, 589–593 (2000).

6. Weatherill, E. E. & Wallace, M. I. Combining Single-Molecule Imaging and Single-Channel Electrophysiology. *J. Mol. Biol.* **427**, 146–157 (2015).

7. Modak, A. *et al.* Single-Molecule Imaging of Integral Membrane Protein Dynamics and Function. *Annu. Rev. Biophys.* **53**, 427–453 (2024).

8. Lu, H. P., Xun, L. & Xie, X. S. Single-Molecule Enzymatic Dynamics. *Science* **282**, 1877–1882 (1998).

9. English, B. P. *et al.* Ever-fluctuating single enzyme molecules: Michaelis-Menten equation revisited. *Nat. Chem. Biol.* **2**, 87–94 (2006).

10. Ciftci, D. *et al.* Single-molecule transport kinetics of a glutamate transporter homolog shows static disorder. *Sci. Adv.* **6**, eaaz1949 (2020).

11. Kosmidis, E. *et al.* Regulation of the mammalian-brain V-ATPase through ultraslow mode-switching. *Nature* **611**, 827–834 (2022).

12. Levring, J. *et al.* CFTR function, pathology and pharmacology at single-molecule resolution. *Nature* **616**, 606–614 (2023).

13. Mutch, S. A. *et al.* Protein Quantification at the Single Vesicle Level Reveals That a Subset of Synaptic Vesicle Proteins Are Trafficked with High Precision. *J. Neurosci.* **31**, 1461–1470 (2011).

14. McVeigh, B. M. *et al.* Visualization of lysosomal membrane proteins by cryo electron tomography. *Nat. Commun.* **16**, 9234 (2025).

15. Sabatini, B. L. & Svoboda, K. Analysis of calcium channels in single spines using optical fluctuation analysis. *Nature* **408**, 589–593 (2000).

16. Wang, W. *et al.* A voltage-dependent K+ channel in the lysosome is required for refilling lysosomal Ca2+ stores. *J. Cell Biol.* **216**, 1715–1730 (2017).

17. Johansson, S. & Arhem, P. Single-channel currents trigger action potentials insmall cultured hippocampal neurons. *Proc. Natl. Acad. Sci.* **91**, 1761–1765 (1994).

18. Higley, M. J. & Sabatini, B. L. Calcium Signaling in Dendrites and Spines: Practical and Functional Considerations. *Neuron* **59**, 902–913 (2008).

19. Trötschel, C. *et al.* Absolute proteomic quantification reveals design principles of sperm flagellar chemosensation. *EMBO J.* **39**, EMBJ2019102723 (2019).

20. Levis, R. A. & Rae, J. L. The use of quartz patch pipettes for low noise single channel recording. *Biophys. J.* **65**, 1666–1677 (1993).

21. Hamill, O. P., Marty, A., Neher, E., Sakmann, B. & Sigworth, F. Improved patch-clamp techniques for high-resolution current recording from cells and cell-free membrane patches. *Eur. J. Physiol.* **391**, 85–100 (1981).

22. Magde, D., Elson, E. & Webb, W. W. Thermodynamic fluctuations in a reacting system–measurement by fluorescence correlation spectroscopy. *Phys. Rev. Lett.* **29**, 705–708 (1972).

23. Ha, T. *et al.* Probing the interaction between two single molecules: fluorescence resonance energy transfer between a single donor and a single acceptor. *Proc. Natl. Acad. Sci.* **93**, 6264–6268 (1996).

24. Rust, M. J., Bates, M. & Zhuang, X. Sub-diffraction-limit imaging by stochastic optical reconstruction microscopy (STORM). *Nat. Methods* **3**, 793–795 (2006).

25. Dickson, R. M., Cubitt, A. B., Tsien, R. Y. & Moerner, W. E. On/off blinking and switching behaviour of single molecules of green fluorescent protein. *Nature* **388**, 355–358 (1997).

26. Betzig, E. *et al.* Imaging intracellular fluorescent proteins at nanometer resolution. *Science* **313**, 1642–1645 (2006).

27. Cohen, A. E. & Moerner, W. E. Method for trapping and manipulating nanoscale objects in solution. *Appl. Phys. Lett.* **86**, 093109–093109 (2005).

28. Shon, M. J. & Cohen, A. E. Mass action at the single-molecule level. *J. Am. Chem. Soc.* **134**, 14618–14623 (2012).

29. Yang, S., Klughammer, N., Barth, A., Tanenbaum, M. E. & Dekker, C. Zero-Mode Waveguide Nanowells for Single-Molecule Detection in Living Cells. *ACS Nano* **17**, 20179–20193 (2023).

30. Møller, M. P. *et al.* Long-term single-molecule Ca2+ flux recordings reveal mode-switching regulation of Ca2+-ATPases. 2026.01.28.701947 Preprint at https://doi.org/10.64898/2026.01.28.701947 (2026).

31. Leslie, S. R., Fields, A. P. & Cohen, A. E. Convex lens-induced confinement for imaging single molecules. *Anal. Chem.* **82**, 6224–6229 (2010).

32. Hensel, Z. & Xiao, J. Single-molecule methods for studying gene regulation in vivo. *Pflüg. Arch. - Eur. J. Physiol.* **465**, 383–395 (2013).

33. Hamill, O. P., Marty, A., Neher, E., Sakmann, B. & Sigworth, F. J. Improved patch-clamp techniques for high-resolution current recording from cells and cell-free membrane patches. *Pflüg. Arch.* **391**, 85–100 (1981).

34. Plested, A. J. R. Single-Channel Recording of Ligand-Gated Ion Channels. *Cold Spring Harb. Protoc.* **2016**, 10.1101/pdb.top087239 (2016).

35. Arroyo, J. P., Kahle, K. T. & Gamba, G. The SLC12 family of electroneutral cation-coupled chloride cotransporters. *Mol. Aspects Med.* **34**, 288–298 (2013).

36. Mueckler, M. & Thorens, B. The SLC2 (GLUT) family of membrane transporters. *Mol. Aspects Med.* **34**, 121–138 (2013).

37. Malik, A. R. & Willnow, T. E. Excitatory Amino Acid Transporters in Physiology and Disorders of the Central Nervous System. *Int. J. Mol. Sci.* **20**, 5671 (2019).

38. Greenwald, E. C., Mehta, S. & Zhang, J. Genetically Encoded Fluorescent Biosensors Illuminate the Spatiotemporal Regulation of Signaling Networks. *Chem. Rev.* **118**, 11707–11794 (2018).

39. Yan, P. *et al.* Near-infrared voltage-sensitive dyes based on chromene donor. *Proc. Natl. Acad. Sci.* **120**, e2305093120 (2023).

40. Navarro, M. X., Gerstner, N. C., Lipman, S. M., Dolgonos, G. E. & Miller, E. W. Improved Sensitivity in a Modified Berkeley Red Sensor of Transmembrane Potential. *ACS Chem. Biol.* **19**, 2214–2219 (2024).

41. Grynkiewicz, G., Poenie, M. & Tsien, R. Y. A new generation of Ca2+ indicators with greatly improved fluorescence properties. *J. Biol. Chem.* **260**, 3440–3450 (1985).

42. Zhang, Y. *et al.* Fast and sensitive GCaMP calcium indicators for imaging neural populations. *Nature* **615**, 884–891 (2023).

43. Kralj, J. M., Douglass, A. D., Hochbaum, D. R., Maclaurin, D. & Cohen, A. E. Optical recording of action potentials in mammalian neurons using a microbial rhodopsin. *Nat. Methods* **9**, 90–95 (2012).

44. Harada, K. *et al.* Red fluorescent protein-based cAMP indicator applicable to optogenetics and in vivo imaging. *Sci. Rep.* **7**, 7351 (2017).

45. Rangaraju, V., Calloway, N. & Ryan, T. A. Activity-Driven Local ATP Synthesis Is Required for Synaptic Function. *Cell* **156**, 825–835 (2014).

46. Aggarwal, A. *et al.* Glutamate indicators with improved activation kinetics and localization for imaging synaptic transmission. *Nat. Methods* **20**, 925–934 (2023).

47. Abdelfattah, A. S. *et al.* Sensitivity optimization of a rhodopsin-based fluorescent voltage indicator. *Neuron* https://doi.org/10.1016/j.neuron.2023.03.009 (2023) doi:10.1016/j.neuron.2023.03.009.

48. Hellweg, L. *et al.* A general method for the development of multicolor biosensors with large dynamic ranges. *Nat. Chem. Biol.* **19**, 1147–1157 (2023).

49. Saminathan, A. *et al.* A DNA-based voltmeter for organelles. *Nat. Nanotechnol.* **16**, 96–103 (2021).

50. Addgene: Fluorescent Protein Guide: Biosensors. https://www.addgene.org/fluorescent-proteins/biosensors/.

51. Akerboom, J. *et al.* Crystal Structures of the GCaMP Calcium Sensor Reveal the Mechanism of Fluorescence Signal Change and Aid Rational Design*. *J. Biol. Chem.* **284**, 6455–6464 (2009).

52. Miyawaki, A. *et al.* Fluorescent indicators for Ca2+based on green fluorescent proteins and calmodulin. *Nature* **388**, 882–887 (1997).

53. Zhang, Y. & Looger, L. L. Fast and sensitive GCaMP calcium indicators for neuronal imaging. *J. Physiol.* **602**, 1595–1604 (2024).

54. Anees, P. *et al.* Detecting organelle-specific activity of potassium channels with a DNA nanodevice. *Nat. Biotechnol.* **42**, 1065–1074 (2024).

55. Zou, J. *et al.* A DNA nanodevice for mapping sodium at single-organelle resolution. *Nat. Biotechnol.* **42**, 1075–1083 (2024).

56. Saha, S., Prakash, V., Halder, S., Chakraborty, K. & Krishnan, Y. A pH-independent DNA nanodevice for quantifying chloride transport in organelles of living cells. *Nat. Nanotechnol.* **10**, 645–651 (2015).

57. Narayanaswamy, N. *et al.* A pH-correctable, DNA-based fluorescent reporter for organellar calcium. *Nat. Methods* **16**, 95–102 (2019).

58. Lee, S. *et al.* Organelles harbour pH gradients. 2025.12.12.694065 Preprint at https://doi.org/10.64898/2025.12.12.694065 (2025).

59. Seidel, Z. P., Wang, J. C. K., Riegler, J., York, A. G. & Ingaramo, M. Relaxation Sensors. *Github.io* https://andrewgyork.github.io/relaxation_sensors/ (2021).

60. Hou, J. H., Venkatachalam, V. & Cohen, A. E. Temporal dynamics of microbial rhodopsin fluorescence reports absolute membrane voltage. *Biophys. J.* **106**, 639–648 (2014).

61. Brooks, F. P. *et al.* Photophysics-informed two-photon voltage imaging using FRET-opsin voltage indicators. *Sci. Adv.* **11**, eadp5763 (2025).

62. Jo, M. H. *et al.* Determination of single-molecule loading rate during mechanotransduction in cell adhesion. *Science* **383**, 1374–1379 (2024).

63. Fitzgerald, G. A. *et al.* Quantifying secondary transport at single-molecule resolution. *Nature* **575**, 528–534 (2019).

64. Ciftci, D. *et al.* Linking function to global and local dynamics in an elevator-type transporter. *Proc. Natl. Acad. Sci.* **118**, e2025520118 (2021).

65. Damm, A. *et al.* Conformational Changes of the ABC Transporter BmrA Depend on Membrane Curvature. *eLife* **15**, (2026).

66. Tonnesen, A., Christensen, S. M., Tkach, V. & Stamou, D. Geometrical Membrane Curvature as an Allosteric Regulator of Membrane Protein Structure and Function. *Biophys. J.* **106**, 201–209 (2014).

67. Shuai, J. & Parker, I. Optical single-channel recording by imaging Ca2+ flux through individual ion channels: theoretical considerations and limits to resolution. *Cell Calcium* **37**, 283–299 (2005).

68. Demuro, A. & Parker, I. “Optical Patch-clamping” : Single-channel Recording by Imaging Ca2+ Flux through Individual Muscle Acetylcholine Receptor Channels. *J. Gen. Physiol.* **126**, 179–192 (2005).

69. Demuro, A. & Parker, I. Optical single-channel recording: imaging Ca2+ flux through individual N-type voltage-gated channels expressed in *Xenopus* oocytes. *Cell Calcium* **34**, 499–509 (2003).

70. Wang, S.-Q., Song, L.-S., Lakatta, E. G. & Cheng, H. Ca2+ signalling between single L-type Ca2+ channels and ryanodine receptors in heart cells. *Nature* **410**, 592–596 (2001).

71. Zou, H., Lifshitz, L. M., Tuft, R. A., Fogarty, K. E. & Singer, J. J. Visualization of Ca2+ entry through single stretch-activated cation channels. *Proc. Natl. Acad. Sci.* **99**, 6404–6409 (2002).

72. Tay, L. H. *et al.* Nanodomain Ca2+ of Ca2+ channels detected by a tethered genetically encoded Ca2+ sensor. *Nat. Commun.* **3**, 778 (2012).

73. Dynes, J. L., Amcheslavsky, A. & Cahalan, M. D. Genetically targeted single-channel optical recording reveals multiple Orai1 gating states and oscillations in calcium influx. *Proc. Natl. Acad. Sci.* **113**, 440–445 (2016).

74. Bertaccini, G. A. *et al.* Visualizing PIEZO1 Localization and Activity in hiPSC-Derived Single Cells and Organoids with HaloTag Technology. 2023.12.22.573117 Preprint at https://doi.org/10.1101/2023.12.22.573117 (2024).

75. Demuro, A. & Parker, I. Imaging single-channel calcium microdomains. *Cell Calcium* **40**, 413–422 (2006).

76. Smith, I. F. & Parker, I. Imaging the quantal substructure of single IP3R channel activity during Ca2+ puffs in intact mammalian cells. *Proc. Natl. Acad. Sci.* **106**, 6404–6409 (2009).

77. Smith, I. F., Shuai, J. & Parker, I. Active Generation and Propagation of Ca2+ Signals within Tunneling Membrane Nanotubes. *Biophys. J.* **100**, L37–L39 (2011).

78. Hediger, M. A., Clémençon, B., Burrier, R. E. & Bruford, E. A. The ABCs of membrane transporters in health and disease (SLC series): Introduction. *Mol. Aspects Med.* **34**, 95–107 (2013).

79. Hille, B. *Ion Channels of Excitable Membranes*. vol. 507 (Sinauer, Sunderland, MA, 2001).

80. Neher, E. & Sakmann, B. Single-channel currents recorded from membrane of denervated frog muscle fibres. *Nature* **260**, 799–802 (1976).

81. Hamill, O. P. & McBride, D. W. Rapid adaptation of single mechanosensitive channels in Xenopus oocytes. *Proc. Natl. Acad. Sci.* **89**, 7462–7466 (1992).

82. Scheppach, C. & Robinson, H. P. C. Fluctuation Analysis in Nonstationary Conditions: Single Ca2+ Channel Current in Pyramidal Neurons. *Biophys. J.* **113**, 2383–2395 (2017).

83. Sanchez, C. *et al.* Detection of Ca2+ transients near ryanodine receptors by targeting fluorescent Ca2+ sensors to the triad. *J. Gen. Physiol.* **153**, e202012592 (2021).

84. Shi, Z., Graber, Z. T., Baumgart, T., Stone, H. A. & Cohen, A. E. Cell Membranes Resist Flow. *Cell* **175**, 1769-1779.e13 (2018).

85. Perez-Reyes, E. Molecular Physiology of Low-Voltage-Activated T-type Calcium Channels. *Physiol. Rev.* **83**, 117–161 (2003).

86. Weber, A. M. *et al.* N-type Ca2+ channels carry the largest current: implications for nanodomains and transmitter release. *Nat. Neurosci.* **13**, 1348–1350 (2010).

87. Chen, T.-W. *et al.* Ultrasensitive fluorescent proteins for imaging neuronal activity. *Nature* **499**, 295–300 (2013).

88. Murthy, V. N., Sejnowski, T. J. & Stevens, C. F. Dynamics of dendritic calcium transients evoked by quantal release at excitatory hippocampal synapses. *Proc. Natl. Acad. Sci.* **97**, 901–906 (2000).

89. Dupont, G., Falcke, M., Kirk, V. & Sneyd, J. *Models of Calcium Signalling*. vol. 43 (Springer International Publishing, Cham, 2016).

90. Allbritton, N. L., Meyer, T. & Stryer, L. Range of Messenger Action of Calcium Ion and Inositol 1,4,5-Trisphosphate. *Science* **258**, 1812–1815 (1992).

91. Derényi, I., Jülicher, F. & Prost, J. Formation and Interaction of Membrane Tubes. *Phys. Rev. Lett.* **88**, 238101 (2002).

92. Naraghi, M. & Neher, E. Linearized Buffered Ca2+ Diffusion in Microdomains and Its Implications for Calculation of [Ca2+] at the Mouth of a Calcium Channel. *J. Neurosci.* **17**, 6961–6973 (1997).

93. Sabatini, B. L., Maravall, M. & Svoboda, K. Ca2+ signaling in dendritic spines. *Curr. Opin. Neurobiol.* **11**, 349–356 (2001).

94. Belardetti, F. *et al.* A Fluorescence-Based High-Throughput Screening Assay for the Identification of T-Type Calcium Channel Blockers. *ASSAY Drug Dev. Technol.* **7**, 266–280 (2009).

95. Spruston, N., Jaffe, D. B., Williams, S. H. & Johnston, D. Voltage- and space-clamp errors associated with the measurement of electrotonically remote synaptic events. *J. Neurophysiol.* **70**, 781–802 (1993).

96. Huguenard, J. R. & McCormick, D. A. Simulation of the currents involved in rhythmic oscillations in thalamic relay neurons. *J. Neurophysiol.* **68**, 1373–1383 (1992).

97. Destexhe, A. & Huguenard, J. R. Nonlinear Thermodynamic Models of Voltage-Dependent Currents. *J. Comput. Neurosci.* **9**, 259–270 (2000).

98. Thompson, S. M. Relations between chord and slope conductances and equivalent electromotive forces. *Am. J. Physiol.-Cell Physiol.* **250**, C333–C339 (1986).

99. Gillespie, D. T. Exact stochastic simulation of coupled chemical reactions. *J. Phys. Chem.* **81**, 2340–2361 (1977).

100. Eisner, D., Neher, E., Taschenberger, H. & Smith, G. Physiology of intracellular calcium buffering. *Physiol. Rev.* **103**, 2767–2845 (2023).

101. Yang, S. *et al.* Membrane curvature governs the distribution of Piezo1 in live cells. *Nat. Commun.* **13**, 7467 (2022).

102. Domanov, Y. A. *et al.* Mobility in geometrically confined membranes. *Proc. Natl. Acad. Sci.* **108**, 12605–12610 (2011).

103. Xiang, K. M., Park, P., Koren, S. A., Hayward, R. F. & Cohen, A. E. All-optical mapping of cAMP transport reveals rules of sub-cellular localization. 2023.06.27.546633 Preprint at https://doi.org/10.1101/2023.06.27.546633 (2023).

104. Hayward, R. F. & Cohen, A. E. All-optical mapping of Ca2+ transport and homeostasis in dendrites. 2024.07.16.603652 Preprint at https://doi.org/10.1101/2024.07.16.603652 (2024).

105. Truong, M. E. *et al.* Vertebrate cells differentially interpret ciliary and extraciliary cAMP. *Cell* **184**, 2911-2926.e18 (2021).

106. Dharan, R. *et al.* Tetraspanin 4 stabilizes membrane swellings and facilitates their maturation into migrasomes. *Nat. Commun.* **14**, 1037 (2023).

107. Itkis, D. G. *et al.* Luminos: open-source software for bidirectional microscopy. 2025.02.22.639658 Preprint at https://doi.org/10.1101/2025.02.22.639658 (2025).

108. Torr, P. H. S. & Zisserman, A. MLESAC: A New Robust Estimator with Application to Estimating Image Geometry. *Comput. Vis. Image Underst.* **78**, 138–156 (2000).

109. Otsu, N. A Threshold Selection Method from Gray-Level Histograms. *IEEE Trans. Syst. Man Cybern.* **9**, 62–66 (1979).

110. Fast 2D peak finder. https://www.mathworks.com/matlabcentral/fileexchange/37388-fast-2d-peak-finder (2021).

111. Schneider, C. A., Rasband, W. S. & Eliceiri, K. W. NIH Image to ImageJ: 25 years of Image Analysis. *Nat. Methods* **9**, 671–675 (2012).

112. Howell, M. R. & Cohen, A. E. Optical Single-Channel Recording via Diffusional Confinement in Membrane Tethers. *ACS Nano* **19**, 26852–26861 (2025).

113. Rahamimoff, R., DeRiemer, S. A., Sakmann, B., Stadler, H. & Yakir, N. Ion channels in synaptic vesicles from Torpedo electric organ. *Proc. Natl. Acad. Sci.* **85**, 5310–5314 (1988).

114. Takamori, S. *et al.* Molecular Anatomy of a Trafficking Organelle. *Cell* **127**, 831–846 (2006).

115. Carrithers, M. D. *et al.* Expression of the Voltage-Gated Sodium Channel NaV1.5 in the Macrophage Late Endosome Regulates Endosomal Acidification1. *J. Immunol.* **178**, 7822–7832 (2007).

116. Ichas, F., Jouaville, L. S. & Mazat, J. P. Mitochondria are excitable organelles capable of generating and conveying electrical and calcium signals. *Cell* **89**, 1145–1154 (1997).

117. Finazzi, G. *et al.* Ions channels/transporters and chloroplast regulation. *Cell Calcium* **58**, 86–97 (2015).

118. Martinac, B., Buechner, M., Delcour, A. H., Adler, J. & Kung, C. Pressure-sensitive ion channel in Escherichia coli. *Proc. Natl. Acad. Sci. U. S. A.* **84**, 2297–2301 (1987).

119. Berrier, C., Besnard, M., Ajouz, B., Coulombe, A. & Ghazi, A. Multiple Mechanosensitive Ion Channels from Escherichia coli, Activated at Different Thresholds of Applied Pressure. *J. Membr. Biol.* **151**, 175–187 (1996).

120. Radchenko, M. V. *et al.* Potassium/Proton Antiport System of *Escherichia coli**. *J. Biol. Chem.* **281**, 19822–19829 (2006).

121. Martinac, B., Saimi, Y. & Kung, C. Ion channels in microbes. *Physiol. Rev.* **88**, 1449 (2008).

122. Sze, C. & Tan, Y.-J. Viral Membrane Channels: Role and Function in the Virus Life Cycle. *Viruses* **7**, 3261–3284 (2015).

123. Sorgato, M. C., Keller, B. U. & Stühmer, W. Patch-clamping of the inner mitochondrial membrane reveals a voltage-dependent ion channel. *Nature* **330**, 498–500 (1987).

124. Scott, C. C. & Gruenberg, J. Ion flux and the function of endosomes and lysosomes: pH is just the start. *BioEssays* **33**, 103–110 (2011).

125. Modi, S. *et al.* A DNA nanomachine that maps spatial and temporal pH changes inside living cells. *Nat. Nanotechnol.* **4**, 325–330 (2009).

126. Pinto, L. H., Holsinger, L. J. & Lamb, R. A. Influenza virus M2 protein has ion channel activity. *Cell* **69**, 517–528 (1992).

127. Akole, A. & Warner, J. M. Model of influenza virus acidification. *PLOS ONE* **14**, e0214448 (2019).

128. Payandeh, J. & Minor, D. L. Bacterial Voltage-Gated Sodium Channels (BacNaVs) from the Soil, Sea, and Salt Lakes Enlighten Molecular Mechanisms of Electrical Signaling and Pharmacology in the Brain and Heart. *J. Mol. Biol.* **427**, 3–30 (2015).

129. Cohen, A. E. & Venkatachalam, V. Bringing Bioelectricity to Light. *Annu. Rev. Biophys.* **43**, 211–232 (2014).

130. Adam, Y. *et al.* Voltage imaging and optogenetics reveal behaviour-dependent changes in hippocampal dynamics. *Nature* **569**, 413–417 (2019).

131. Tian, H. *et al.* Video-based pooled screening yields improved far-red genetically encoded voltage indicators. *Nat. Methods* **20**, 1082–1094 (2023).

132. Lu, X. *et al.* Widefield imaging of rapid pan-cortical voltage dynamics with an indicator evolved for one-photon microscopy. *Nat. Commun.* **14**, 6423 (2023).

133. Hao, Y. A. *et al.* A fast and responsive voltage indicator with enhanced sensitivity for unitary synaptic events. *Neuron* **112**, 3680-3696.e8 (2024).

134. Kannan, M. *et al.* Dual-polarity voltage imaging of the concurrent dynamics of multiple neuron types. *Science* **378**, eabm8797 (2022).

135. Miller, E. W. *et al.* Optically monitoring voltage in neurons by photo-induced electron transfer through molecular wires. *Proc. Natl. Acad. Sci.* **109**, 2114–2119 (2012).

136. Antic, S. D. *et al.* ElectroFluor Voltage-Sensitive Dyes: Comprehensive Analysis of Wavelength-Dependent Sensitivity and Cross-Channel Bleed-Through. *J. Biophotonics* **n/a**, e70008.

137. Cohen, A. E. & Venkatachalam, V. Bringing bioelectricity to light. *Annu Rev Biophys* **43**, 11.1-11.22 (2014).

138. Sepehri Rad, M., Cohen, L. B., Braubach, O. & Baker, B. J. Monitoring voltage fluctuations of intracellular membranes. *Sci. Rep.* **8**, 6911 (2018).

139. Crowley, L. C., Christensen, M. E. & Waterhouse, N. J. Measuring Mitochondrial Transmembrane Potential by TMRE Staining. *Cold Spring Harb. Protoc.* **2016**, (2016).

140. Kowaltowski, A. J. & Abdulkader, F. How and when to measure mitochondrial inner membrane potentials. *Biophys. J.* **123**, 4150–4157 (2024).

141. Cornejo, V. H., Ofer, N. & Yuste, R. Voltage compartmentalization in dendritic spines in vivo. *Science* **375**, eabg0501 (2021).

142. Armbruster, M. *et al.* Neuronal activity drives pathway-specific depolarization of peripheral astrocyte processes. *Nat. Neurosci.* **25**, 607–616 (2022).

143. Kralj, J. M., Hochbaum, D. R., Douglass, A. D. & Cohen, A. E. Electrical spiking in Escherichia coli probed with a fluorescent voltage indicating protein. *Science* **333**, 345–348 (2011).

144. Benarroch, J. M. & Asally, M. The Microbiologist's Guide to Membrane Potential Dynamics. *Trends Microbiol.* **28**, 304–314 (2020).

145. Anees, P. *et al.* Detecting organelle-specific activity of potassium channels with a DNA nanodevice. *Nat. Biotechnol.* **42**, 1065–1074 (2024).

146. Skaugen, E. & Walløe, L. Firing behaviour in a stochastic nerve membrane model based upon the Hodgkin—Huxley equations. *Acta Physiol. Scand.* **107**, 343–363 (1979).

147. Faisal, A. A., White, J. A. & Laughlin, S. B. Ion-Channel Noise Places Limits on the Miniaturization of the Brain's Wiring. *Curr. Biol.* **15**, 1143–1149 (2005).

148. Chow, C. C. & White, J. A. Spontaneous action potentials due to channel fluctuations. *Biophys. J.* **71**, 3013–3021 (1996).

149. White, J. A., Rubinstein, J. T. & Kay, A. R. Channel noise in neurons. *Trends Neurosci.* **23**, 131–137 (2000).

150. Goldwyn, J. H. & Shea-Brown, E. The What and Where of Adding Channel Noise to the Hodgkin-Huxley Equations. *PLOS Comput. Biol.* **7**, e1002247 (2011).

151. Mino, H., Rubinstein, J. T. & White, J. A. Comparison of Algorithms for the Simulation of Action Potentials with Stochastic Sodium Channels. *Ann. Biomed. Eng.* **30**, 578–587 (2002).

152. White, J. A., Klink, R., Alonso, A. & Kay, A. R. Noise from voltage-gated ion channels may influence neuronal dynamics in the entorhinal cortex. *J. Neurophysiol.* **80**, 262–269 (1998).

153. Schmid, G., Goychuk, I. & Hänggi, P. Channel noise and synchronization in excitable membranes. *Phys. Stat. Mech. Its Appl.* **325**, 165–175 (2003).

154. Zeng, S., Tang, Y. & Jung, P. Spiking synchronization of ion channel clusters on an axon. *Phys. Rev. E* **76**, 011905 (2007).

155. Cannon, R. C., O'Donnell, C. & Nolan, M. F. Stochastic Ion Channel Gating in Dendritic Neurons: Morphology Dependence and Probabilistic Synaptic Activation of Dendritic Spikes. *PLOS Comput. Biol.* **6**, e1000886 (2010).

156. Hübel, N. & Dahlem, M. A. Dynamics from Seconds to Hours in Hodgkin-Huxley Model with Time-Dependent Ion Concentrations and Buffer Reservoirs. *PLoS Comput. Biol.* **10**, e1003941 (2014).

157. Di Francesco, D. & Noble, D. A model of cardiac electrical activity incorporating ionic pumps and concentration changes. *Philos. Trans. R. Soc. Lond. B Biol. Sci.* **307**, 353–398 (1997).

158. Xu, H., Martinoia, E. & Szabo, I. Organellar channels and transporters. *Cell Calcium* **58**, 1–10 (2015).

159. Hodgkin, A. L. & Huxley, A. F. A quantitative description of membrane current and its application to conduction and excitation in nerve. *J. Physiol.* **117**, 500–544 (1952).

160. Hübel, N., Schöll, E. & Dahlem, M. A. Bistable Dynamics Underlying Excitability of Ion Homeostasis in Neuron Models. *PLOS Comput. Biol.* **10**, e1003551 (2014).

161. Barreto, E. & Cressman, J. R. Ion concentration dynamics as a mechanism for neuronal bursting. *J. Biol. Phys.* **37**, 361–373 (2011).

162. Sherman, A., Rinzel, J. & Keizer, J. Emergence of organized bursting in clusters of pancreatic beta-cells by channel sharing. *Biophys. J.* **54**, 411–425 (1988).

163. Krishnan, G. P. & Bazhenov, M. Ionic dynamics mediate spontaneous termination of seizures and post-ictal depression state. *J. Neurosci. Off. J. Soc. Neurosci.* **31**, 8870–8882 (2011).

164. Chay, T. R. & Keizer, J. Minimal model for membrane oscillations in the pancreatic beta-cell. *Biophys. J.* **42**, 181–189 (1983).

165. Sherman, A. & Rinzel, J. Model for synchronization of pancreatic beta-cells by gap junction coupling. *Biophys. J.* **59**, 547–559 (1991).

166. Balbi, P., Massobrio, P. & Kotaleski, J. H. A single Markov-type kinetic model accounting for the macroscopic currents of all human voltage-gated sodium channel isoforms. *PLOS Comput. Biol.* **13**, e1005737 (2017).

167. Ishida, Y., Nayak, S., Mindell, J. A. & Grabe, M. A model of lysosomal pH regulation. *J. Gen. Physiol.* **141**, 705–720 (2013).

168. Grabe, M., Wang, H. & Oster, G. The Mechanochemistry of V-ATPase Proton Pumps. *Biophys. J.* **78**, 2798–2813 (2000).

169. Schmandt, N. T. & Galán, R. F. Stochastic-Shielding Approximation of Markov Chains and its Application to Efficiently Simulate Random Ion-Channel Gating. *Phys. Rev. Lett.* **109**, (2012).

170. Chow, C. C. & White, J. A. Spontaneous action potentials due to channel fluctuations. *Biophys. J.* **71**, 3013–3021 (1996).

171. Skaugen, E. & Walløe, L. Firing behaviour in a stochastic nerve membrane model based upon the Hodgkin—Huxley equations. *Acta Physiol. Scand.* **107**, 343–363 (1979).

172. Gillespie, D. T. Exact stochastic simulation of coupled chemical reactions. *J. Phys. Chem.* **81**, 2340–2361 (1977).

173. Grabe, M. & Oster, G. Regulation of Organelle Acidity. *J. Gen. Physiol.* **117**, 329–344 (2001).

174. Takamori, S. *et al.* Molecular Anatomy of a Trafficking Organelle. *Cell* **127**, 831–846 (2006).

175. Murk, J. L. a. N. *et al.* Endosomal compartmentalization in three dimensions: Implications for membrane fusion. *Proc. Natl. Acad. Sci.* **100**, 13332–13337 (2003).

176. Ganley, I. G., Carroll, K., Bittova, L. & Pfeffer, S. Rab9 GTPase Regulates Late Endosome Size and Requires Effector Interaction for Its Stability. *Mol. Biol. Cell* **15**, 5420–5430 (2004).

177. Farsi, Z. *et al.* Single-vesicle imaging reveals different transport mechanisms between glutamatergic and GABAergic vesicles. *Science* **351**, 981–984 (2016).

178. Daniels, R. W. *et al.* A Single Vesicular Glutamate Transporter Is Sufficient to Fill a Synaptic Vesicle. *Neuron* **49**, 11–16 (2006).

179. Upmanyu, N. *et al.* Colocalization of different neurotransmitter transporters on synaptic vesicles is sparse except for VGLUT1 and ZnT3. *Neuron* **110**, 1483-1497.e7 (2022).

180. Koivusalo, M., Steinberg, B. E., Mason, D. & Grinstein, S. In situ Measurement of the Electrical Potential Across the Lysosomal Membrane Using FRET. *Traffic* **12**, 972–982 (2011).

181. Bezanilla, F. Single sodium channels from the squid giant axon. *Biophys. J.* **52**, 1087–1090 (1987).

182. Marty, A. Ca-dependent K channels with large unitary conductance in chromaffin cell membranes. *Nature* **291**, 497–500 (1981).

183. Hales, T. G. *et al.* Common Determinants of Single Channel Conductance within the Large Cytoplasmic Loop of 5-Hydroxytryptamine Type 3 and α4β2 Nicotinic Acetylcholine Receptors*. *J. Biol. Chem.* **281**, 8062–8071 (2006).

184. Barreto, E. & Cressman, J. R. Ion concentration dynamics as a mechanism for neuronal bursting. *J. Biol. Phys.* **37**, 361–373 (2011).

185. Scott, C. C. & Gruenberg, J. Ion flux and the function of endosomes and lysosomes: pH is just the start. *BioEssays* **33**, 103–110 (2011).

186. Salzer, J. L. Clustering Sodium Channels at the Node of Ranvier: Close Encounters of the Axon–Glia Kind. *Neuron* **18**, 843–846 (1997).

187. Harnett, M. T., Makara, J. K., Spruston, N., Kath, W. L. & Magee, J. C. Synaptic amplification by dendritic spines enhances input cooperativity. *Nature* **491**, 599–602 (2012).

188. Somjen, G. G. Mechanisms of Spreading Depression and Hypoxic Spreading Depression-Like Depolarization. *Physiol. Rev.* **81**, 1065–1096 (2001).

189. Dreier, J. P. The role of spreading depression, spreading depolarization and spreading ischemia in neurological disease. *Nat. Med.* **17**, 439–447 (2011).

190. Howell, M. R., Xu, R. J. & Adam, E. C. Electrophysiology in nanoscale compartments. 2025.08.29.673146 Preprint at https://doi.org/10.1101/2025.08.29.673146 (2026).

191. Sun, X.-P., Schlichter, L. C. & Stanley, E. F. Single-channel properties of BK-type calcium-activated potassium channels at a cholinergic presynaptic nerve terminal. *J. Physiol.* **518**, 639–651 (1999).

192. Gameiro, A., Braams, S., Rauen, T. & Grewer, C. The Discovery of Slowness: Low-Capacity Transport and Slow Anion Channel Gating by the Glutamate Transporter EAAT5. *Biophys. J.* **100**, 2623–2632 (2011).

193. Featherstone, D. E. Intercellular Glutamate Signaling in the Nervous System and Beyond. *ACS Chem. Neurosci.* **1**, 4–12 (2010).

194. Lewerenz, J. *et al.* The Cystine/Glutamate Antiporter System xc− in Health and Disease: From Molecular Mechanisms to Novel Therapeutic Opportunities. *Antioxid. Redox Signal.* **18**, 522–555 (2013).

195. CHESLER, M. Regulation and Modulation of pH in the Brain. *Physiol. Rev.* **83**, 1183–1221 (2003).

196. Deisl, C., Chung, J. H. & Hilgemann, D. W. Longitudinal diffusion barriers imposed by myofilaments and mitochondria in murine cardiac myocytes. *J. Gen. Physiol.* **155**, e202213329 (2023).

197. al-Baldawi, N. F. & Abercrombie, R. F. Cytoplasmic hydrogen ion diffusion coefficient. *Biophys. J.* **61**, 1470–1479 (1992).

198. Aggarwal, A. *et al.* Glutamate indicators with increased sensitivity and tailored deactivation rates. *Nat. Methods* **23**, 417–425 (2026).

199. Constantin, C. E. *et al.* Ca2+-pumping by PMCA-neuroplastin complexes operates in the kiloHertz-range. *Nat. Commun.* **16**, 7550 (2025).

200. Sankaranarayanan, S., Angelis, D. D., Rothman, J. E. & Ryan, T. A. The Use of pHluorins for Optical Measurements of Presynaptic Activity. *Biophys. J.* **79**, 2199–2208 (2000).

201. Nagel, G. *et al.* Channelrhodopsin-2, a directly light-gated cation-selective membrane channel. *Proc. Natl. Acad. Sci.* **100**, 13940–13945 (2003).

202. Kleinlogel, S. *et al.* Ultra light-sensitive and fast neuronal activation with the Ca2+-permeable channelrhodopsin CatCh. *Nat. Neurosci.* **14**, 513–518 (2011).

203. Nielsen, T. A., DiGregorio, D. A. & Silver, R. A. Modulation of Glutamate Mobility Reveals the Mechanism Underlying Slow-Rising AMPAR EPSCs and the Diffusion Coefficient in the Synaptic Cleft. *Neuron* **42**, 757–771 (2004).

204. Choi, Y.-B. & Lipton, S. A. Redox modulation of the NMDA receptor. *Cell. Mol. Life Sci. CMLS* **57**, 1535–1541 (2000).

205. Iftinca, M. C. & Zamponi, G. W. Regulation of neuronal T-type calcium channels. *Trends Pharmacol. Sci.* **30**, 32–40 (2009).

206. Wolfe, J. T., Wang, H., Howard, J., Garrison, J. C. & Barrett, P. Q. T-type calcium channel regulation by specific G-protein βγ subunits. *Nature* **424**, 209–213 (2003).

207. Kockelkoren, G. *et al.* Molecular mechanism of GPCR spatial organization at the plasma membrane. *Nat. Chem. Biol.* **20**, 142–150 (2024).

208. Shah, M. *et al.* Mitochondria structurally remodel near synapses to fuel the sustained energy demands of plasticity. 2025.08.27.672715 Preprint at https://doi.org/10.1101/2025.08.27.672715 (2025).

209. Ott, C. M. & Lippincott-Schwartz, J. Design principles of ciliary signaling. *J. Cell Sci.* **138**, jcs264325 (2025).

210. Delling, M., DeCaen, P. G., Doerner, J. F., Febvay, S. & Clapham, D. E. Primary cilia are specialized calcium signalling organelles. *Nature* **504**, 311–314 (2013).

211. White, D. S., Smith, M. A., Chanda, B. & Goldsmith, R. H. Strategies for Overcoming the Single-Molecule Concentration Barrier. *ACS Meas. Sci. Au* **3**, 239–257 (2023).

212. Destexhe, A. & Huguenard, J. R. Modeling Voltage-Dependent Channels. in *Computational Modeling Methods for Neuroscientists* (ed. De Schutter, E.) 0 (The MIT Press, 2009). doi:10.7551/mitpress/9780262013277.003.0006.

213. Balbi, P., Massobrio, P. & Kotaleski, J. H. A single Markov-type kinetic model accounting for the macroscopic currents of all human voltage-gated sodium channel isoforms. *PLOS Comput. Biol.* **13**, e1005737 (2017).

214. Bezanilla, F. Single sodium channels from the squid giant axon. *Biophys. J.* **52**, 1087–1090 (1987).

215. Llano, I., Webb, C. K. & Bezanilla, F. Potassium conductance of the squid giant axon. Single-channel studies. *J. Gen. Physiol.* **92**, 179–196 (1988).

216. Beyder, A. *et al.* Mechanosensitivity of Nav1.5, a voltage-sensitive sodium channel. *J. Physiol.* **588**, 4969–4985 (2010).

217. McKinney, L. C. & Moran, A. Regulation of intracellular pH in J774 murine macrophage cells: H+ extrusion processes. *Am. J. Physiol.-Cell Physiol.* **268**, C210–C217 (1995).

218. Holmes, W. R. Cable Theory: Overview. in *Encyclopedia of Computational Neuroscience* 1–2 (Springer, New York, NY, 2014). doi:10.1007/978-1-4614-7320-6_757-1.

Appendix A. Supplemental information for Chapter Two

A.1 Model of single-channel Ca^{2+} domains in a tether and cell body membrane.

We assume: [1] The equilibration time of Ca^{2+} buffering is fast relative to diffusion out of the observation volume, so free and buffer-bound Ca^{2+} exist in a local equilibrium. [2] The change in total (free + bound) Ca^{2+} concentration, $\Delta[Ca^{2+}]_T$, due to a single channel gating event does not saturate endogenous buffers. Therefore, the change in free Ca^{2+}, $\Delta[Ca^{2+}]_{free}$, can be expressed as a fraction of $\Delta[Ca^{2+}]_T$:

$$\Delta[\mathrm{Ca}^{2+}]_{\mathrm{free}} = \frac{\Delta[\mathrm{Ca}^{2+}]_{\mathrm{T}}}{1+\kappa_{\mathrm{B}}}, \quad \text{A1}$$

where κ_B is the cytoplasm Ca^{2+} buffering capacity.

The effective diffusion coefficient of Ca^{2+} is a weighted average of free (D_{Ca}) and buffer-bound (D_B) Ca^{2+} diffusion coefficients:

$$D_{\mathrm{eff}}^{\mathrm{Ca}} = \frac{D_{\mathrm{Ca}}+D_{\mathrm{B}}\kappa_{\mathrm{B}}}{1+\kappa_{\mathrm{B}}}. \quad \text{A2}$$

To calculate the spatiotemporal profiles of single-channel Ca^{2+} domains in a tether, we solve the diffusion equation numerically using the MATLAB *pdepe* solver,

$$\frac{\partial[\mathrm{Ca}^{2+}]_{\mathrm{free}}}{\partial t} = D_{\mathrm{eff}}^{\mathrm{Ca}}\nabla^2[\mathrm{Ca}^{2+}]_{\mathrm{free}}\ , \quad \text{A3}$$

with boundary conditions:

$$\text{at } x = 0\text{: } \frac{\partial[\mathrm{Ca}^{2+}]_{\mathrm{free}}}{\partial x} = -\frac{\phi}{D_{\mathrm{eff}}^{\mathrm{Ca}}\, a\, (1+\kappa_{\mathrm{B}})},$$

$$\lim_{x\to\infty}[\mathrm{Ca}^{2+}]_{\mathrm{free}} = [\mathrm{Ca}^{2+}]_0,$$

where *x* denotes distance from the open channel and *a* denotes tether cross-sectional area. $\Delta[Ca^{2+}]_{free}$ profiles are calculated using the model parameters in **Table A.1**. We used the same diffusion model to calculate volume-averaged $\Delta[Ca^{2+}]_{free}$ in the cell body.

For transient channel opening, we can estimate the time-dependent concentration within an observation volume centered on the channel. In a tether, the molecules are diluted into a volume of approximate dimensions $a \times \sqrt{2D_{\mathrm{eff}}^{\mathrm{Ca}}t}$. Hence the concentration scales as $a^{-1}\left(2D_{\mathrm{eff}}^{\mathrm{Ca}}t\right)^{-1/2}$. In the bulk, the molecules are diluted into a volume of approximate dimensions $\left(\sqrt{2D_{\mathrm{eff}}^{\mathrm{Ca}}t}\right)^3$, so the concentration scales

as $\left(2D_{\mathrm{eff}}^{\mathrm{Ca}}t\right)^{-3/2}$. Thus, the fluorescent signal from a transiently open channel decays much more slowly in a tether ($t^{-1/2}$) than in the bulk ($t^{-3/2}$).

A.2 Model of T-type voltage-gated Ca^{2+} channels.

We employ the Hodgkin-Huxley (HH) model of T-type Ca_V currents developed by Huguenard and McCormick[96]. Briefly, the macroscopic current, I_{Ca} is defined as the product of the unitary Ca^{2+} conductance, g_{SC}, the ensemble-averaged channel open probability, P_O, the number of Ca_V channels in the membrane, N_C, and the voltage and $[Ca^{2+}]$-dependent driving force, G.

$$I_{\mathrm{Ca}}(V,t) = g_{\mathrm{sc}}P_{\mathrm{O}}(V,t)N_{\mathrm{c}}G(V,[\mathrm{Ca}_{\mathrm{i}}^{2+}],[\mathrm{Ca}_{\mathrm{o}}^{2+}]), \quad \text{A4}$$

where P_O is modeled as the product of three independent two-state gates: two activation *m*-gates and one inactivation *h*-gate.

$$P_O(V,t) = m^2h. \quad \text{A5}$$

To fit P_O parameters (see below, section A.2.2 Thermodynamic model of rate constants) to our ensemble currents, we used G defined by the Goldman-Hodgkin-Katz current equation (in units of C m^{-3}) and a membrane permeability (P, $m^3\ s^{-1}$), such that

$$I_{\mathrm{Ca}}(V,t) = m^2h \times P \times G(V,[\mathrm{Ca}_{\mathrm{i}}^{2+}],[\mathrm{Ca}_{\mathrm{o}}^{2+}]). \quad \text{A6}$$

For stochastic simulation of single-channel trajectories (see section A.3), we define the unitary current, i_{Ca}, as the product of P_O, G, and a single-channel permeability, p (same units as above).

$$i_{\mathrm{Ca}}(V,t) = m^2h \times p \times G(V,[\mathrm{Ca}_{\mathrm{i}}^{2+}],[\mathrm{Ca}_{\mathrm{o}}^{2+}]), \quad \text{A7}$$

where p is related to the single-channel slope conductance[98] g_{sc}, measured by *Weber et al.* in the linear i-V regime:

$$p = g_{\mathrm{sc}} \times \left(\frac{z^2F^2}{RT} \times \left(\frac{[\mathrm{Ca}_{\mathrm{o}}^{2+}]-[\mathrm{Ca}_{\mathrm{i}}^{2+}](1+\zeta)e^{\zeta}}{(1-e^{\zeta})} + \frac{\zeta e^{\zeta}([\mathrm{Ca}_{\mathrm{o}}^{2+}]-[\mathrm{Ca}_{\mathrm{i}}^{2+}]e^{\zeta})}{(1-e^{\zeta})^2}\right)\right)^{-1}, \quad \text{A8}$$

where $\zeta \equiv \frac{zFV_{\mathrm{m}}}{RT}$ and $V_{\mathrm{m}} = -70\ \mathrm{mV}$.

A.2.1 Channel gating

The voltage-dependent equilibrium for each gate (x = *m* or *h*) and its time-dependent and steady state open probability are expressed below. All gates must open for the channel to conduct a current.

$$\text{Open} \underset{\alpha_{\mathrm{x}}(V)}{\overset{\beta_{\mathrm{x}}(V)}{\rightleftharpoons}} \text{Closed} \quad \text{A9}$$

$$x(V,t) = x_\infty(V) + [\mathrm{x}_0 - x_\infty(V)]\mathrm{e}^{\frac{-t}{\tau_\mathrm{x}(V)}} \quad \text{A10}$$

$$x_\infty(V) = \frac{\alpha_\mathrm{x}(V)}{\alpha_\mathrm{x}(V)+\beta_\mathrm{x}(V)} \quad \text{A11}$$

$$\tau_\mathrm{x}(V) = \frac{1}{\alpha_\mathrm{x}(V)+\beta_\mathrm{x}(V)} \quad \text{A12}$$

Where α and β are voltage-dependent transition rates and τ denotes the time constant of activation or inactivation.

A.2.2 Thermodynamic model of rate constants

We employ the thermodynamic model of voltage dependent rate constants described by Destexhe and Huguenard.[97] Briefly, each transition rate, $r = \alpha_\mathrm{x}, \beta_\mathrm{x}$ is described by a Boltzmann distribution, where ΔG is the free energy barrier associated with the transition, R is the gas constant, and T is the temperature.

$$r(V) = r_0\mathrm{e}^{-\frac{\Delta G(V)}{RT}}, \quad \text{A13}$$

where ΔG is expressed as a nonlinear function of voltage.

$$\Delta G(V) = a + bV + cV^2 + dV^3. \quad \text{A14}$$

Defining V_x as the voltage at which $\alpha_\mathrm{x} = \beta_\mathrm{x}$, we arrive at the following rate expressions for the m and h gates (see section A.2 for a definition of m and h).

$$\alpha_\mathrm{m}(V) = A_\mathrm{m}e^{-[b_{\mathrm{m}1}(V-V_\mathrm{m})+c_{\mathrm{m}1}(V-V_\mathrm{m})^2+d_{\mathrm{m}1}(V-V_\mathrm{m})^3]/RT}, \quad \text{A15}$$

$$\beta_\mathrm{m}(V) = A_\mathrm{m}e^{-[b_{\mathrm{m}2}(V-V_\mathrm{m})+c_{\mathrm{m}2}(V-V_\mathrm{m})^2+d_{\mathrm{m}2}(V-V_\mathrm{m})^3]/RT}, \quad \text{A16}$$

$$\alpha_\mathrm{h}(V) = A_\mathrm{h}e^{-[b_{\mathrm{h}1}(V-V_\mathrm{h})+c_{\mathrm{h}1}(V-V_\mathrm{h})^2+d_{\mathrm{h}1}(V-V_\mathrm{h})^3]/RT}, \quad \text{A17}$$

$$\beta_\mathrm{h}(V) = A_\mathrm{h}e^{-[b_{\mathrm{h}2}(V-V_\mathrm{h})+c_{\mathrm{h}2}(V-V_\mathrm{h})^2+d_{\mathrm{h}2}(V-V_\mathrm{h})^3]/RT}, \quad \text{A18}$$

Using the parameters reported in Destexhe *et al.* as a starting point, we further refined the parameter values to fit our macroscopic $Ca_V3.2$ currents (see Table A2 and Fig. A7).

A.3 Stochastic simulation of single-channel trajectories.

We employed the Gillespie algorithm[99] to simulate single-channel trajectories using thermodynamic models of transition rates fit to our ensemble-average currents. Our implementation of the algorithm is as follows:

Define voltage-dependent transition rates (Eq. A15–A18), $\alpha_\mathrm{x}(V), \beta_\mathrm{x}(V)$.

Assume equilibrium at voltage $V = V_\mathrm{hold}$ prior to the first time-step, t_1.

1. assign an initial open probability $P_O(t_0)$

   draw a random sample, s_0 from a uniform distribution, U: $s_0 \sim U(0,1)$

   define x_∞ as the equilibrium open probability (Eq. A11)

   if $s_0 < x_\infty(V = V_{\text{hold}})$ then $P_O(t_0) = 1$ (open)

   else $P_O(t_0) = 0$ (closed)

2. instantaneously step to $V = V_{\text{test}}$

3. sample the gate dwell time, τ in the t_0 state (open or closed)

   for $P_O(t_0) = 1$ (open)

$$\tau_O = -\frac{1}{\beta_x(V = V_{\text{test}})} ln[u \sim U(0,1)]$$

   for $P_O(t_0) = 0$ (closed)

$$\tau_c = -\frac{1}{\alpha_x(V = V_{\text{test}})} ln[u \sim U(0,1)]$$

4. sample the following state

   for $P_O(t_0) = 1$

$$s_1 \sim U(0,1)$$

   if $s_1 < \beta_x(V = V_{\text{test}}) \times \tau_O$ then $P_O(t_0 + \tau_O) = 0$

   else $P_O(t_0 + \tau_O) = 1$

   for $P_O(t_0) = 0$

$$s_1 \sim U(0,1)$$

   if $s_1 < \alpha_x(V = V_{\text{test}}) \times \tau_C$ then $P_O(t_0 + \tau_C) = 1$

   else $P_O(t_0 + \tau_C) = 0$

5. repeat for $t \leq 45$ ms

We estimated the distribution of charge influx from simulated single-channel trajectories by integrating Eq. A7 over t_V (**Figure 2.5 D**, **Figure A.7**).

Table A.1 Parameters for modeling single-channel Ca^{2+} domains

Parameter		Ref.
Buffer dissociation constant K_d	1 μM	[67,89]
Buffer concentration $[B]_T$	200 μM	[67,89]
Buffering capacity κ_B	200	$\approx [B]_T/K_d$ [18]
Buffer diffusion coefficient D_B	20 $\mu m^2\ s^{-1}$	[88,89]
Free Ca^{2+} diffusion coefficient D_{Ca}	200 $\mu m^2\ s^{-1}$	[90]
Single channel Ca^{2+} transport rate φ	1×10^5 ions s^{-1}	[86]
Tether length, L	10 μm	
Tether radius, r_t	50 nm	
Confocal volume radius, r_0	250 nm	

Table A.2 Fit of model parameters to macroscopic currents.
See section A.2 for a description of the gating model. T = 32 °C

m-gate parameters	
V_m	-49 mV
A_m	0.093 ms^{-1}
b_{m1}	-340 J mV^{-1}
c_{m1}	3.6 J mV^{-2}
d_{m1}	5.4e-4 J mV^{-3}
b_{m2}	130 J mV^{-1}
c_{m2}	3.8 J mV^{-2}
d_{m2}	0.018 J mV^{-3}

h-gate parameters	
V_h	-69 mV
A_h	2.7e-3 ms^{-1}
b_{h1}	150 J mV^{-1}
c_{h1}	6.5 J mV^{-2}
d_{h1}	0.062 J mV^{-3}
b_{h2}	-470 J mV^{-1}
c_{h2}	7.0 J mV^{-2}
d_{h2}	-0.057 J mV^{-3}

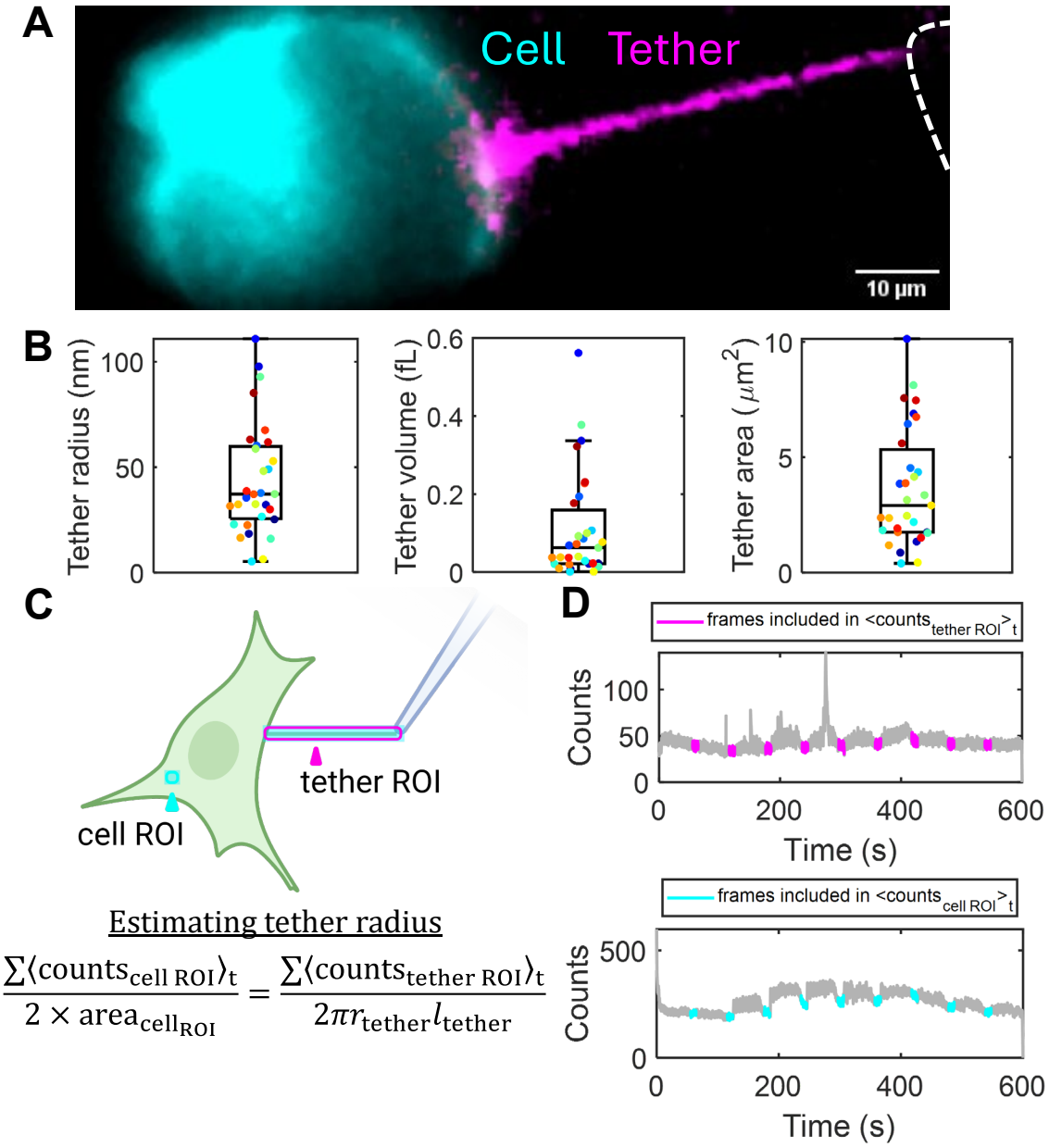

Figure A.1 Characterization of tether geometry.
A. Fluorescence image of a membrane tether extracted from a HEK293 cell expressing lck-jGCaMP8f and $Ca_V3.2$. Image is a composite of two pictures, one with tether-only illumination (purple) and one with cell body illumination (cyan). Tether-only contrast is enhanced to aid visualization. **B.** Distribution of tether radii (left, n = 31 tethers, median 37.2 nm), volumes (middle, median 62.7 aL), and surface areas (right, median 2.91 µm^2) estimated using baseline fluorescence counts/membrane area from cell body lck-jGCaMP8f or GCaMP6s-CAAX and assuming cylindrical tether geometry (box: median, 25th and 75th percentiles, extrema). **C.** Procedure for estimating radii of tethers. Excitation light (light blue) is restricted to the tether (magenta) and a small patch of the cell membrane (cyan). **D.** Cell and tether GECI fluorescence, recorded in the absence of depolarizing stimulus (cyan and magenta timepoints), are averaged in time and summed over region of interest (ROI). Bottom: cell ROI counts per ROI area (accounting for excitation of top and bottom membrane patches) provides a count density, which is used to estimate tether radius.

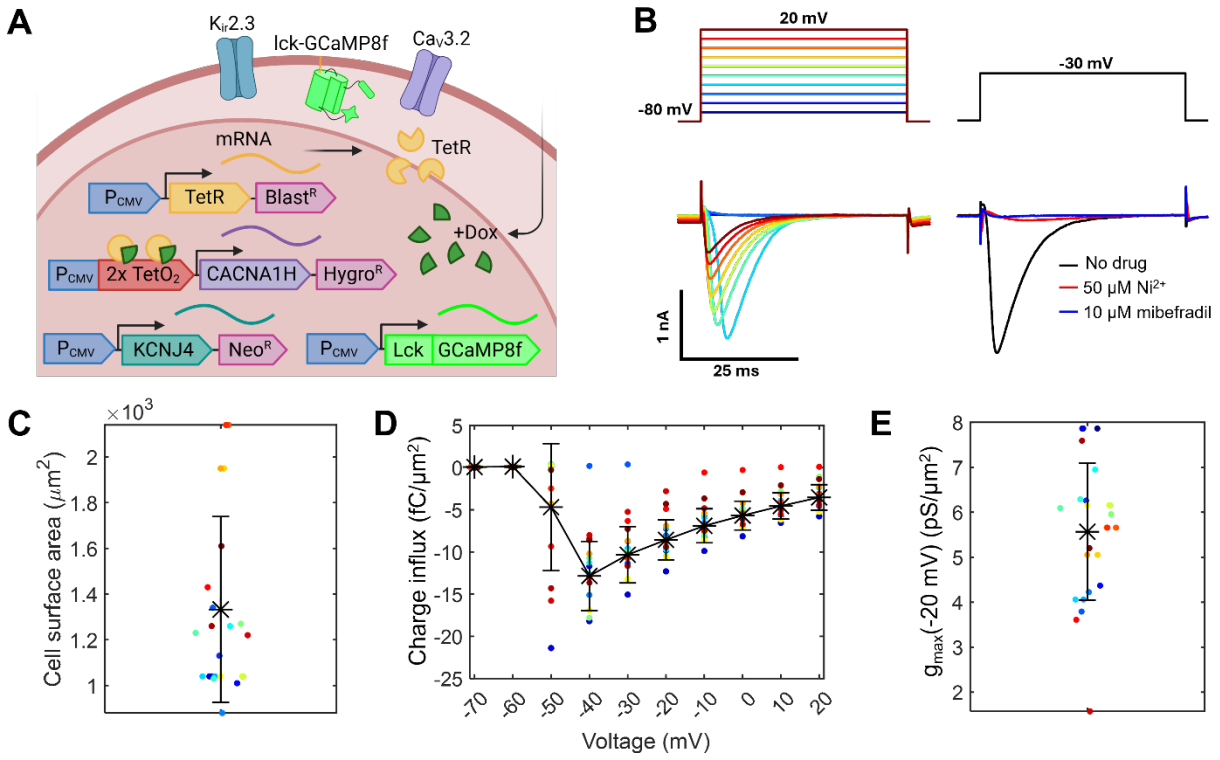

Figure A.2 Electrophysiology of HEK cells expressing $Ca_V3.2$.
A. HEK293 cell line stably incorporated genes encoding Tet repressor (TetR), tetracycline-inducible $Ca_V3.2$ pore-forming subunit CACNA1H, and constitutive $K_{ir}2.3$ inward-rectifier potassium channel KCNJ4. Membrane-targeted GECI (lck-jGCaMP8f shown here) was expressed by transient transfection. **B.** Representative inward currents (bottom, left) in response to depolarizing voltage pulses (top). $Ca_V3.2$ channel blockers suppressed these currents (bottom, right). **C.** Distribution of cell surface areas, calculated from whole cell capacitance, assuming a specific membrane capacitance of 1 μF/cm^2 (1332 ± 406 μm^2, mean ± s.d., n = 17 cells). **D.** Distribution of charge influx densities. Cells were treated with 1.5 ng/mL doxycycline and measured at 24-48 hr post-induction. Charge influx density was calculated via the time integral of whole-cell inward currents and dividing by the cell surface area (mean ± s.d., n = 17 cells). **E.** Distribution of conductance densities for the cells analyzed in C-D. Calculated by taking the maximal inward current measured at -20 mV and dividing by the Ca^{2+} driving force (5.57 ± 1.52 pS/μm^2, mean ± s.d., n = 17 cells). Multiplying the average conductance density by the median tether area (2.9 μm^2, **Figure A.1**), and dividing by prior estimates of channel conductance[86] (g = 1.7 pS) and predicted maximum channel open probability (P_o = 0.82) yields an estimate of ~12 channels per tether.

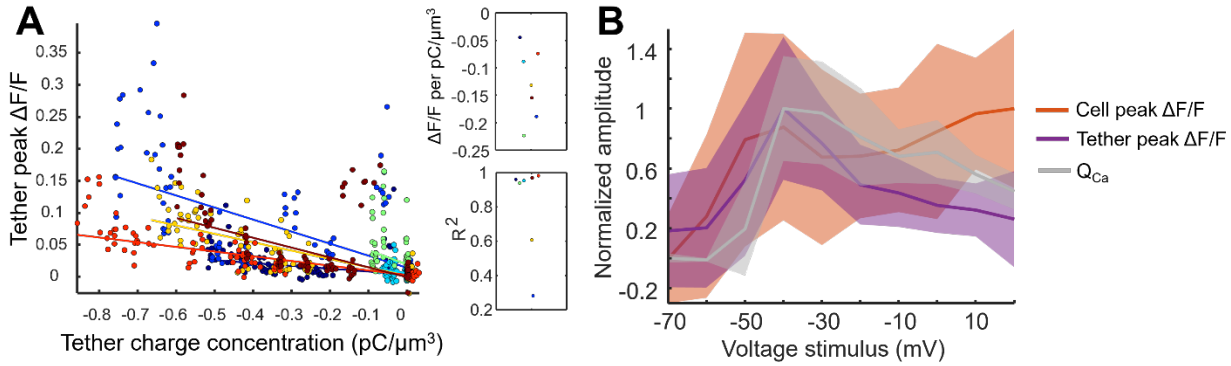

Figure A.3 Tether Ca^{2+}, reported by GCaMP6s-CAAX, correlates with ensemble charge transport. **A.** Peak $(\Delta F/F)^t$ amplitude of tether GCaMP6s-CAAX fluorescence transients as a function of predicted tether charge concentration, $[Q_{Ca}^t]$, and linear fits. Inset: slope (top) and R^2 (bottom) from linear fits of n = 7 tethers. **B.** Voltage dependence of stimulus-evoked charge transport (gray), tether (purple) and cell (orange) peak ΔF/F amplitudes averaged across n = 7 GCaMP6s-CAAX cell-tether pairs. Traces are normalized for each tether-cell pair before averaging and shaded to show std. dev.

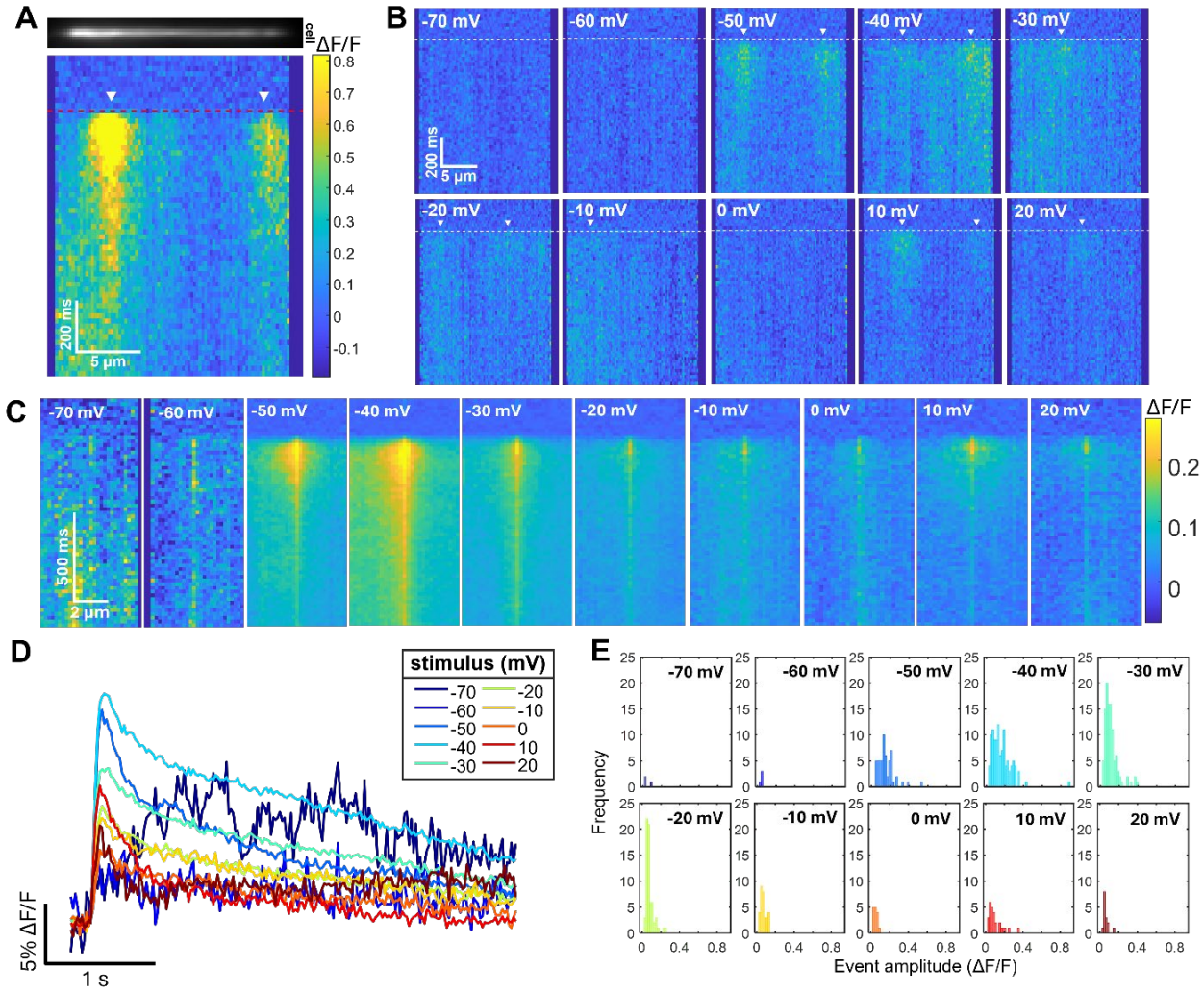

Figure A.4 Spatiotemporal structure and statistics of Ca^{2+} events reported by GCaMP6s-CAAX indicator.

A. Epifluorescence image of a tether above a kymograph for a 45 ms voltage step from -80 mV to -30 mV. Red dashed line indicates step onset. White arrowheads indicate discrete Ca^{2+} events. **B**. Kymographs of tether Ca^{2+}-dependent fluorescence in response to voltage steps from -80 mV to between -70 mV and +20 mV. White dashed lie indicates step onset. Data shown for single-trial responses of one tether. **C**. Stimulus-triggered average kymographs of spatially isolated tether Ca^{2+} events (n = 3-106 events per voltage, 7 tethers). **D**. Timecourse of events in (C), averaged over ±2.2 mm from the fluorescence peak. **E**. Histogram of Ca^{2+} event amplitudes at each stimulus voltage (n = 3-106 events per voltage, 7 tethers). Event amplitudes are taken from spatiotemporally filtered kymographs.

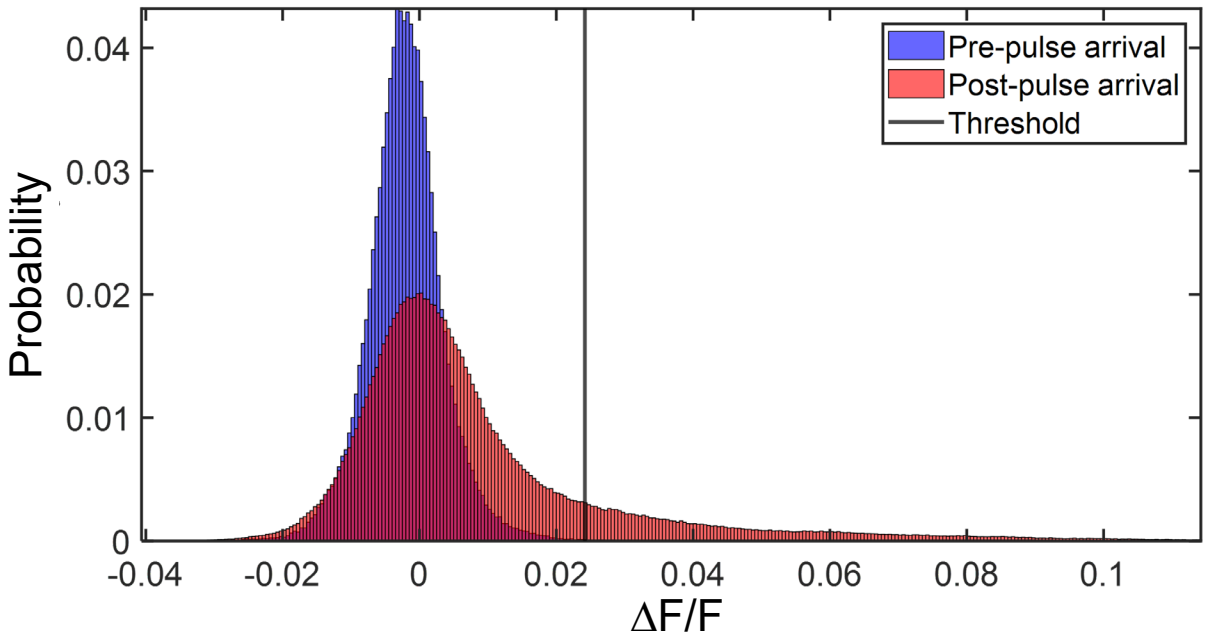

Figure A.5 Ca^{2+} event detection threshold in tethers from HEK cells expressing lck-jGCaMP8f. Distribution of pixel intensities within pre-stimulus window (V_m = -80 mV, blue) and all pixels within post-stimulus window (red, V_m = -70 to 20 mV, includes Ca^{2+} event and non-event pixels) for one lck-jGCaMP8f expressing tether. Black line indicates threshold used to segment Ca^{2+} events. Threshold calculation described in Section 2.5 Methods.

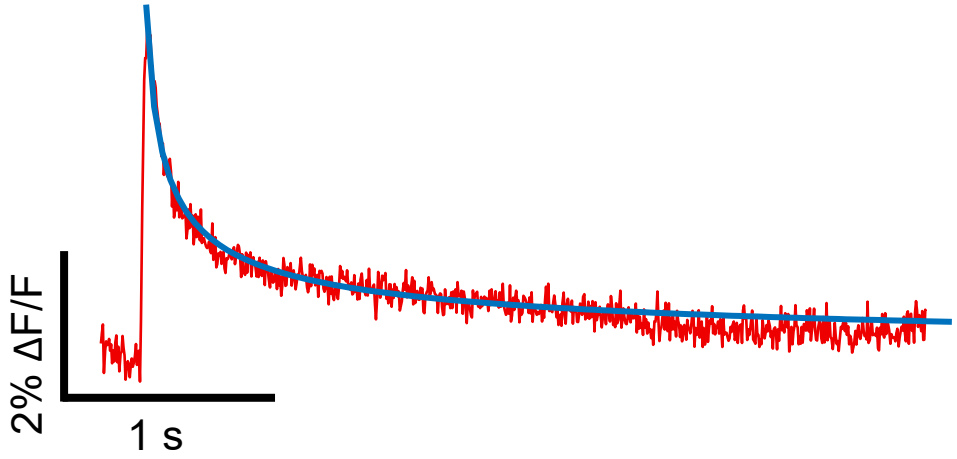

Figure A.6 Diffusion-based model fit to Ca^{2+} signal decay.
Time-dependent peak GCaMP8f signal from single-molecule gating events, for a voltage step from -80 mV to +10 mV (red; data from **Figure 2.4 D**). A fit to the predicted $t^{1/2}$ time dependence from the diffusion kernel is shown in blue.

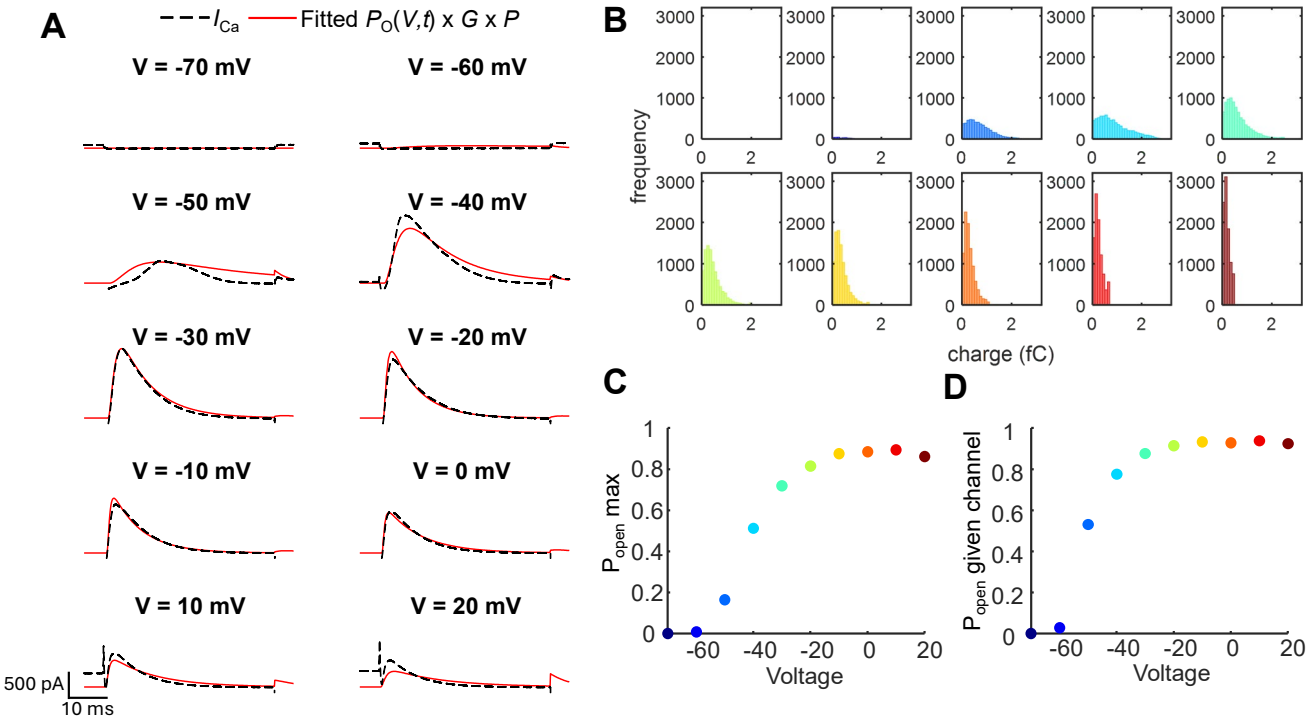

Figure A.7 Refinement of gating model and simulation of $Ca_V3.2$ channel trajectories.
A. Comparison of measured macroscopic currents (dashed black line, average of n = 17 cells) and I_{Ca} (Eq. A6) simulated using a nonlinear thermodynamic model of transition rates (Eq. A15-A18) with fitted parameters (red trace, **Table A.2**). **B.** Histogram of total charge conducted during simulated 45 ms single-channel trajectories (see Appendix A.3 for a description of the stochastic simulation). **C.** Peak open probability during 45 ms stimulation for an ensemble of simulated channels. **D.** Predicted probability of a given channel opening at least once during 45 ms stimulation. N = 10^4 channel trajectories simulated for B-D.

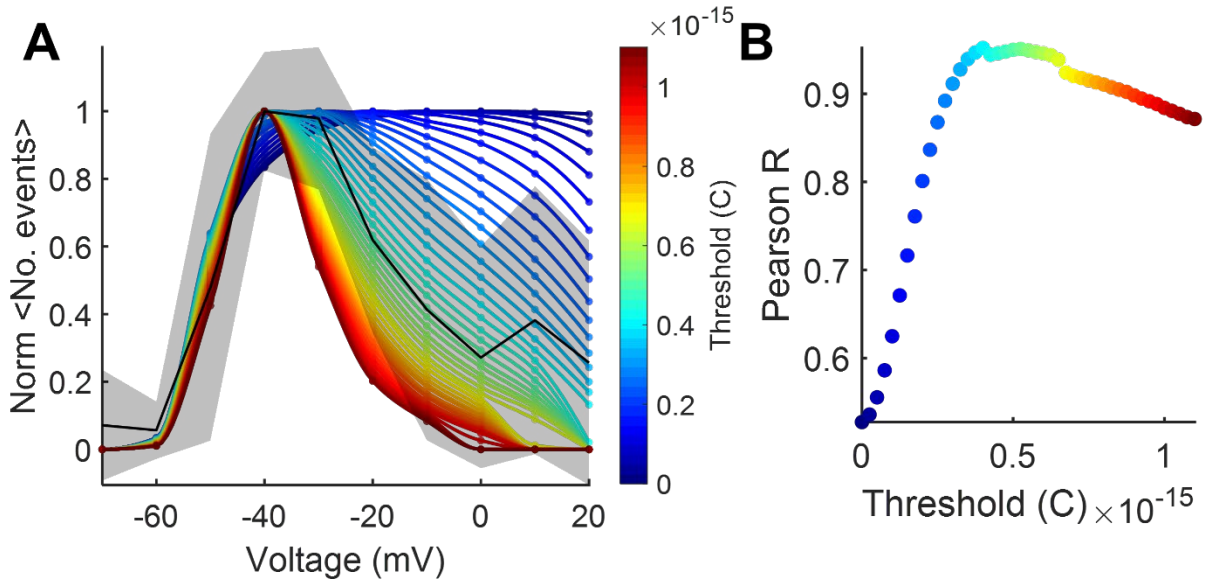

Figure A.8 Detection threshold for Ca^{2+} events reported by GCaMP6s-CAAX fluorescence.
A. Mean number of events vs. voltage (normalized, black, shading std. dev. of n = 7 tethers) and stochastic simulations of the probability of observing a single-channel event (colors). Color bar indicates simulated charge detection threshold. **B.** Pearson correlation between the frequency of observed events (A, black) and the predicted single-channel event probability (A, colors) as function of detection threshold (maximum R-value at 0.4 fC threshold).

Appendix B. Supplemental information for Chapter Three

B.1 Effect of single-channel gating on ion concentrations

For concreteness we consider a persistent Na^+ current, though the discussion applies to any persistent current. The membrane voltage, V_m, evolves according to:

$$\frac{dV_m}{dt} = -\frac{1}{C_M}\left(i_{Na}(t) + i_{Leak}(t)\right), \quad \text{B1}$$

Where $i_{Na}(t)$ is the inward Na^+ current, $i_{Leak}(t)$ is the outward leak current, and C_M is the membrane capacitance. The rate of change of concentration of Na^+ inside the vesicle is:

$$\frac{d[Na^+]_{in}}{dt} = -\frac{i_{Na}(t)}{M\,z\,F}, \quad \text{B2}$$

where M is the vesicle volume, z is the valence (1 for Na^+) and F is the Faraday constant. The Na^+ current is:

$$i_{Na}(t) = g_{Na}(V_m(t) - E_{Na}(t)). \quad \text{B3}$$

For clarity, we make the time-dependencies explicit and define g_x as the channel's open-state conductance and $E_x(t)$ as the channel's reversal potential; x = Na^+ or leak ion. We assume that the voltage is in a local equilibrium (i.e. voltage changes are fast compared to the concentrations). Solving Eq. B1 for the steady-state voltage, $V_{ss}(t)$:

$$V_{ss}(t) = \frac{g_{Na}E_{Na}(t) + g_{Leak}E_{Leak}(t)}{g_{Na} + g_{Leak}}. \quad \text{B4}$$

Setting $V_m(t) = V_{ss}(t)$ in Eq. B3 and combining Eqs. B2 and B3 gives:

$$\frac{d[Na^+]_{in}}{dt} = \left(\frac{g_{Na}g_{Leak}}{g_{Na} + g_{Leak}}\right)\frac{1}{MzF}\,(E_{Na}(t) - E_{Leak}(t)). \quad \text{B5}$$

Finally, the sodium reversal potential changes with time as the internal concentration changes:

$$E_{Na} = \frac{RT}{zF}\ln\frac{[Na^+]_{out}}{[Na^+]_{in}(t)}. \quad \text{B6}$$

Combining Eqs. B5 and B6 gives an expression for the dynamics of $[Na^+]_{in}$:

$$\frac{d[Na^+]_{in}}{dt} = \left(\frac{g_{Na}g_{Leak}}{g_{Na} + g_{Leak}}\right)\frac{1}{MzF}\left(\frac{RT}{zF}\ln\frac{[Na^+]_{out}}{[Na^+]_{in}(t)} - E_{Leak}(t)\right). \quad \text{B7}$$

In the case where $g_{Leak} \propto r^2$ and $M \propto r^3$ (i.e. a constant leak conductance per unit membrane area in a spherical vesicle), then $\frac{d[Na^+]_{in}}{dt} \propto -\frac{1}{r}$ for small vesicles ($g_{Na} \gg A\,G_0$) and $\frac{d[Na^+]_{in}}{dt} \propto -\frac{1}{r^3}$ for large vesicles ($g_{Na}^0 \ll A\,G_0$).

Equation A7 is nonlinear in $[\mathrm{Na}^+]_{\mathrm{in}}$ and does not have a closed-form analytical solution. Numerical integration yields the time-dependent trajectory of $[\mathrm{Na}^+]_{\mathrm{in}}$. An approximate timescale can be estimated by extrapolating the initial rate of change to the entire transition from $[\mathrm{Na}^+]_{\mathrm{in}}(0)$ to $[\mathrm{Na}^+]_{\mathrm{in}}(\infty)$, i.e.

$$\tau_{conc} \approx \left([\mathrm{Na}^+]_{\mathrm{in}}(\infty) - [\mathrm{Na}^+]_{\mathrm{in}}(0)\right) / \left.\frac{d[\mathrm{Na}^+]_{\mathrm{in}}}{dt}\right|_{t=0}, \quad \text{B8}$$

where

$$\left.\frac{d[\mathrm{Na}^+]_{\mathrm{in}}}{dt}\right|_{t=0} = \left(\frac{g_{\mathrm{Na}} g_{\mathrm{Leak}}}{g_{\mathrm{Na}} + g_{\mathrm{Leak}}}\right) \frac{1}{MzF} \left(E_{Na}(0) - E_{\mathrm{Leak}}(0)\right). \quad \text{B9}$$

Combining Eqs. B8 and B9 yields Eq. 3.19 in the main text.

B.2 Markov model of HH-type Na_V and K_V gating

Markov model of Na_V and K_V gating. Diagram adapted from [212]. Abbreviations: I – inactivated; C – closed; O – open.

Na_V:

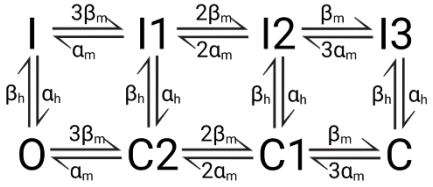

K_V:

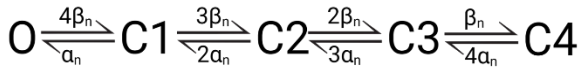

Transition rate functions for default Na_V model, adapted from [160], where all times are measured in milliseconds and all voltages in millivolts:

$$\alpha_{\mathrm{m}} = \frac{0.1(V + 30 + S_{\mathrm{m}})}{1 - \exp\left(-\frac{(V + 30 + S_{\mathrm{m}})}{10A_{\mathrm{m}}}\right)}$$

$$\beta_{\mathrm{m}} = 4\exp\left(-\frac{(V + 55 + S_{\mathrm{m}})}{18A_{\mathrm{m}}}\right)$$

$$\alpha_{\mathrm{h}} = 0.07\exp\left(-\frac{(V + 44 + S_{\mathrm{h}})}{20A_{\mathrm{h}}}\right)$$

$$\beta_{\mathrm{h}} = \frac{1}{1 + \exp\left(-\frac{(V + 14 + S_{\mathrm{h}})}{10A_{\mathrm{h}}}\right)}$$

$$\alpha_{\mathrm{n}} = \frac{0.01(V + 34)}{1 - \exp\left(-\frac{(V + 34)}{10}\right)}$$

$$\beta_{\mathrm{n}} = 0.125 \exp\left(-\frac{(V + 44)}{80}\right)$$

Default Na_V contains moderate window currents: $S_m = S_h = 0$; $A_m = A_h = 1$.

Na_V with large window currents (Na_V^+): $S_m = 10$; $S_h = -10$; $A_m = 0.55$; $A_h = 0.55$.

Na_V with small window currents (Na_V^-): $S_m = -10$; $S_h = 19$; $A_m = 0.95$; $A_h = 1$.

B.3 Markov model of $Na_V1.5$ gating

$Na_V1.5$ state diagram and transition rate functions from [213]. The unified model developed by Balbi *et al.* accounts for $Na_V1.1$-1.9 dynamics using fewer channel states than the Markov model of HH-type Na_V (Appendix B.2) and isoform-specific gating rates.

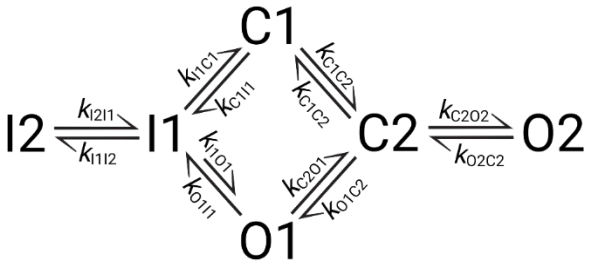

Abbreviations: I – inactivated; C – closed; O – open. All times are measured in milliseconds and all voltages in millivolts:

$$k_{\mathrm{C1C2}} = \frac{10}{1 + e^{\frac{V-(-13)}{-10}}}$$

$$k_{\mathrm{C2C1}} = \frac{1}{1 + e^{\frac{V-(-43)}{8}}} + \frac{10}{1 + e^{\frac{V-(-13)}{-10}}}$$

$$k_{\mathrm{C2O1}} = \frac{10}{1 + e^{\frac{V-(-23)}{-10}}}$$

$$k_{\mathrm{O1C2}} = \frac{1}{1 + e^{\frac{V-(-53)}{8}}} + \frac{10}{1 + e^{\frac{V-(-23)}{-10}}}$$

$$k_{\mathrm{C2O2}} = \frac{0.05}{1 + e^{\frac{V-(-10)}{-10}}}$$

$$k_{\mathrm{O2C2}} = \frac{2}{1 + e^{\frac{V-(-50)}{10}}} + \frac{0.08}{1 + e^{\frac{V-(-20)}{-10}}}$$

$$k_{\mathrm{O1I1}} = \frac{7}{1 + e^{\frac{V-(-44)}{13}}} + \frac{10}{1 + e^{\frac{V-(-19)}{-13}}}$$

$$k_{\mathrm{I1O1}} = \frac{1 \times 10^{-5}}{1 + e^{\frac{V-(-20)}{10}}}$$

$$k_{\mathrm{I1C1}} = \frac{0.19}{1 + e^{\frac{V-(-110)}{7}}}$$

$$k_{\mathrm{C1I1}} = \frac{0.016}{1 + e^{\frac{V-(-92)}{-6}}}$$

$$k_{\mathrm{I1I2}} = \frac{2.2 \times 10^{-4}}{1 + e^{\frac{V-(-50)}{-5}}}$$

$$k_{\mathrm{I2I1}} = \frac{1.8 \times 10^{-3}}{1 + e^{\frac{V-(-90)}{30}}}$$

Table B.1 Electrophysiological parameters and initial conditions of the HH neuron-type vesicle model.

Parameter	Value	Reference
Radius (μm)	0.02 - 10	
Na_V channel density (μm^{-2})	0.8 - 8000	
K_V channel density (μm^{-2})	0.2 - 2000	
Extravesicular volume (μm^{-3})	100000	
C_m, Membrane capacitance ($pF/\mu m^{-2}$)	0.01	[160]
g_{Na_V} , Na_V single-channel conductance (nS)	0.014	[214]
g_{K_V} , K_V single-channel conductance (nS)	0.020	[215]
$g_{Na^+,leak}$, Na^+ leakage conductance ($nS/\mu m^{-2}$)	0.000175	[160]
$g_{K^+,leak}$, K^+ leakage conductance ($nS/\mu m^{-2}$)	0.0005	[160]
$g_{Cl^-,leak}$, Cl^- leakage conductance ($nS/\mu m^{-2}$)	0.0005	[160]
$I_{pump,max}$, Maximum v-ATPase pump rate (pA)	0.0525	[160,184]
$[Na^+]_i$, Intravesicular Na^+ concentration (mM)	27	[160]
$[Na^+]_e$, Extravesicular Na^+ concentration (mM)	120	[160]
$[K^+]_i$, Intravesicular K^+ concentration (mM)	131	[160]
$[K^+]_e$, Extravesicular K^+ concentration (mM)	4	[160]
$[Cl^-]_i$, Intravesicular Cl^- concentration (mM)	9.66	[160]
$[Cl^-]_e$, Extravesicular Cl^- concentration (mM)	124	[160]
V_m , Initial membrane voltage (mV)	-68.0	
E_{Na^+}, Na^+ reversal potential (mV)	39.7	
E_{K^+}, K^+ reversal potential (mV)	-92.9	
E_{Cl^-} , Cl^- reversal potential (mV)	-68.0	

Table B.2 Electrophysiological parameters and initial conditions of the endosome model.

Parameter	Value	Reference
Radius (μm)	0.2	
$Na_V1.5$ channel density (μm^{-2})	0 - 6400	
v-ATPase pump density (μm^{-2})	700	[173]
ClC-7 channel density (μm^{-2})	300	[167]
Extravesicular volume (μm^{-3})	100000	
C_m, Membrane capacitance ($pF/\mu m^{-2}$)	0.01	[160]
$g_{Na_V 1.5}$, $Na_V1.5$ single-channel conductance (nS)	0.0173	[216]
$[Na^+]_i$, Luminal Na^+ concentration (mM)	100	[185]
$[Na^+]_e$, Intracellular Na^+ concentration (mM)	12	
$[Cl^-]_i$, Luminal Cl^- concentration (mM)	19	[185]
$[Cl^-]_e$, Intracellular Cl^- concentration (mM)	10	
pH_i , Luminal pH	6.2	[185]
pH_e , Intracellular pH in macrophages	7.5	[217]
Luminal H^+ buffering capacity ($\mathrm{mM/dpH}$)	40	[173]
V_m , Initial membrane voltage (mV)	19	[180]
E_{Na^+}, Na^+ reversal potential (mV)	-56.5	

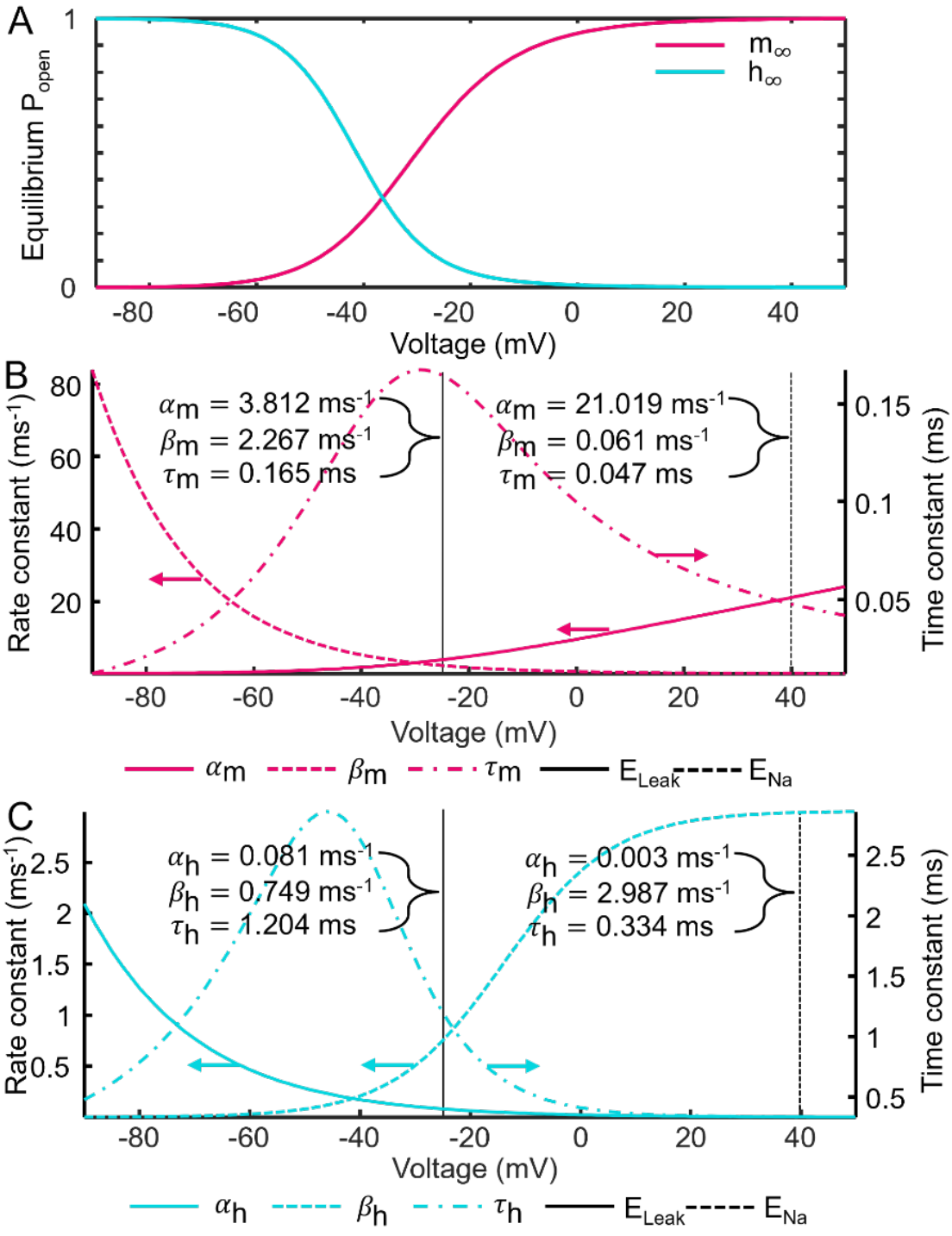

Figure B.1 Na_V model.
A. Steady-state activation (pink) and inactivation (cyan). **B**. Voltage-dependent kinetic parameters of the activation (m) gate. Activation rate, α_m (solid); deactivation rate, β_m (dash); time constant τ_m (dash dot). Vertical lines indicate parameter values at the leak reversal (E_{Leak}, solid black line) used in **Figure *3.2* B-E** and the Na^+ reversal potential (E_{Na}, dash black line). **C**. Same as B, for the inactivation (h) gate.

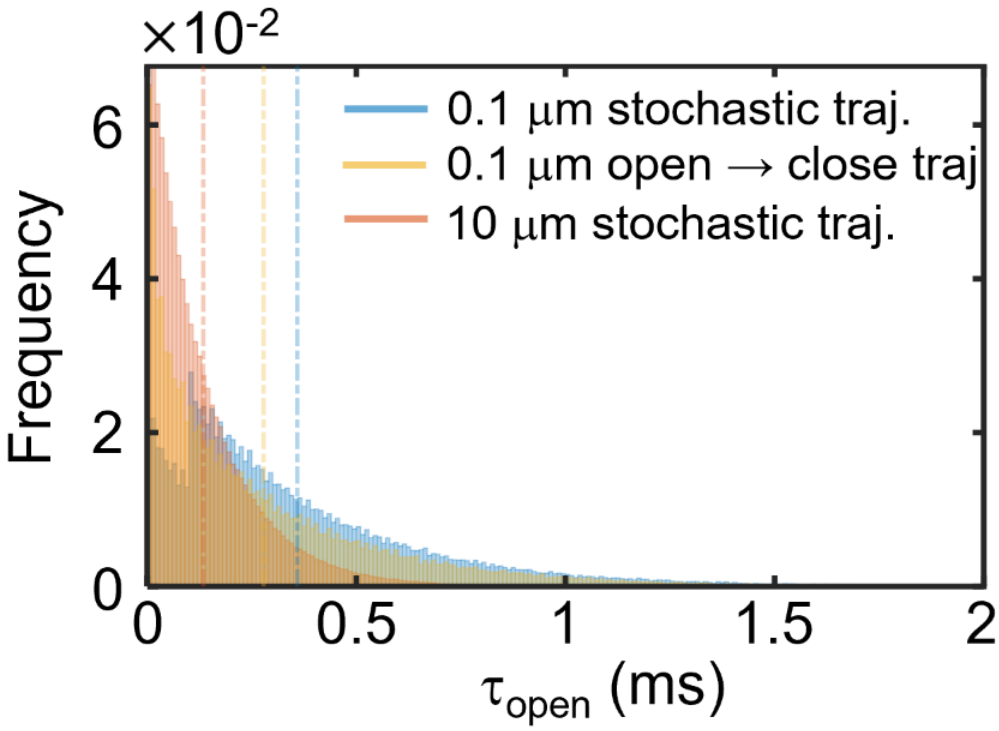

Figure B.2 Time-dependent open-state lifetime in single-channel Na$_V$ vesicles.
Open-state dwell time histograms for spontaneous gating trajectories of single Na$_V$ channels in vesicles of radius $r = 0.1\ \mu\text{m}$ (blue) and $r = 10\ \mu\text{m}$ (orange); simulations 5,000 s. Leak reversal potential, $E_{\text{Leak}} = -25\ \text{mV}$. Shown for comparison are the open-state lifetimes of Na$_V$ in single-channel $r = 0.1\ \mu\text{m}$ vesicles were the Na$_V$ channel is initialized in the open state at $V_{\text{m}} = E_{\text{Leak}}$ (yellow); 2×10^5 independent trials. Dashed vertical lines indicate the distribution means; $r = 0.1\ \mu\text{m}$ stochastic trajectory $\langle \tau_{\text{open}} \rangle = 0.36 \pm 0.33\ \text{ms}$ (blue); $r = 10\ \mu\text{m}$ stochastic trajectory $\langle \tau_{\text{open}} \rangle = 0.13 \pm 0.13\ \text{ms}$ (orange); and $r = 0.1\ \mu\text{m}$ open → closed lifetime $\langle \tau_{\text{open}} \rangle = 0.28 \pm 0.31\ \text{ms}$ (yellow); $(\text{mean} \pm \text{s.d})$.

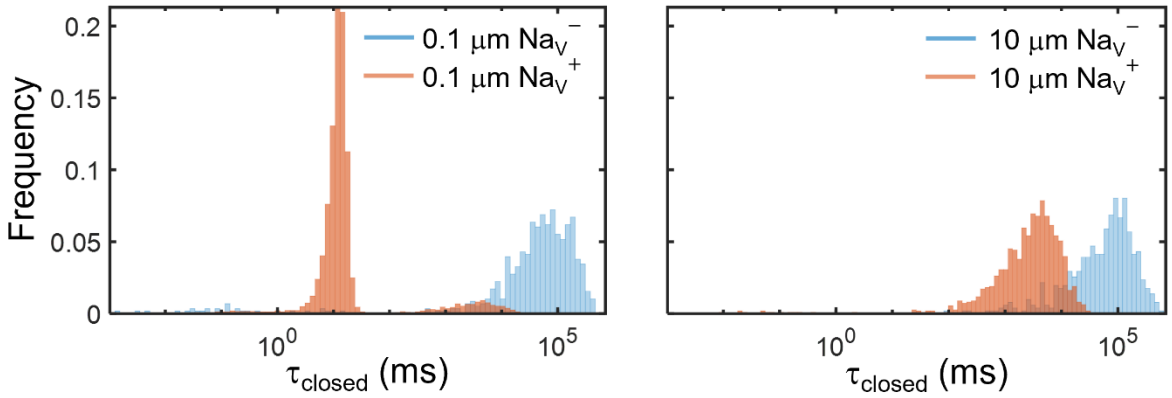

Figure B.3 Nanoscale vesicles support distinct patterns of channel gating.
Closed state dwell-time histograms of spontaneous channel gating in single $\mathrm{Na_V}$ channel vesicles of radii (left) $r = 0.1\ \mu\mathrm{m}$ and (right) $r = 10\ \mu\mathrm{m}$. HH-type $\mathrm{Na_V}$ gating parameters were adjusted to generate a model with substantial window current (denotated by $\mathrm{Na_V^+}$, orange) and a model with negligible window ($\mathrm{Na_V^-}$, blue). $\mathrm{Na_V^+}$ simulations 5,000 s; $\mathrm{Na_V^-}$ results are aggregated from five independent trials of 5,000 s simulations. $E_{\mathrm{leak}} = -60\ \mathrm{mV}$. Modified gating model parameters are described in Appendix B.2

Appendix C. Supplemental Information for Chapter Four

C.1 Passive electrical properties of tethers

In Chapter 2.3.2 we estimate the electrotonic length, λ of tethers as $\lambda \approx 110\ \mu m$. This estimate comes from a cable model of passive electrical coupling between the cell body (assumed isopotential and well-clamped by the patch pipette) and the tether. The cable model describes how voltage (e.g. from a voltage clamped cell body, or injected current) evolves as a function of time and position within an ~1D cable (e.g. dendrite, axon or tether). We assume uniform axial resistance r_i and membrane resistance r_m and cable radius, a<< λ such that $V \approx V(x,t)$:

$$\lambda^2 \frac{\partial^2 V}{\partial x^2} = \tau \frac{\partial V}{\partial t} + V \qquad \text{C1}$$

Where

$$\lambda = \sqrt{\frac{r_m}{r_i}} = \sqrt{\frac{aR_m}{2R_i}} \text{ and } \tau = r_m c_m.$$

The specific resistance of the membrane is R_m (Ω m^2) and of the cytosol is R_i (Ω m). The membrane capacitance is c_m (F). For values of $R_\mathrm{m} = 1.5 \times 10^6\ \mathrm{M\Omega\ \mu m^2}$ and $R_i = 3.0\ \mathrm{M\Omega\ \mu m}$ based on estimates from ref[95] and radius $a = 50\ \mathrm{nm}$, $\lambda \approx 110\ \mathrm{\mu m}$.

The steady-state solution $\frac{\partial V}{\partial t} = 0$ for a semi-infinite tether $x \in (0, \infty)$ shows that the length constant λ, corresponds to the distance at which the voltage decays e-fold from its value, $V_{x=0}$ at the proximal end of the tether

$$V(x) = V_{x=0} e^{-x/\lambda}. \qquad \text{C2}$$

The steady-state solution for a finite tether[95,218], $x \in (0, l)$ yields a quantitative estimate of the voltage drop along the tether:

$$V(x) = V_{x=0} \frac{\cosh\left(\frac{l-x}{\lambda}\right)}{\cosh\left(\frac{l}{\lambda}\right)}. \qquad \text{C3}$$

For a tether with $\lambda \approx 110\ \mathrm{\mu m}$ and $l = 10\ \mathrm{\mu m}$ the steady-state voltage decay is ~0.5% of its initial value at the end of the tether. Importantly, these estimates depend on the magnitude of R_i and R_m – which we have not measured – as well as tether radius, which we found varies widely (**Figure A.1**). Nonetheless, the voltage dependence of $Ca_V3.2$ channel gating which we observed in tethers corresponded well to the voltage clamped at the cell body, suggesting that space-clamp errors were minimal.

C.2 Mechanisms of voltage compartmentalization in tether-like structures

Under what conditions can tether-like protrusions, with similar passive properties, remain electrically compartmentalized from the cell body? Experiments in dendritic spines[187] and primary cilia[210] suggest that voltage in these protrusions are not clamped by the larger compartments to which they are attached. To understand this, we must first calculate the input resistance of a tether-like protrusion by solving Eq. C1 at steady-state for $x \in (0, l)$ and current injection at x = 0:[218]

$$V(x) = \frac{\sqrt{r_i r_m} I_0 \cosh\left(\frac{(l-x)}{\lambda}\right)}{\sinh\left(\frac{l}{\lambda}\right)}. \quad \text{C4}$$

Where

$V(0) = \frac{\sqrt{r_i r_m} I_0}{\tanh\left(\frac{l}{\lambda}\right)}$ and $R_{in} = \frac{\sqrt{r_i r_m}}{\tanh\left(\frac{l}{\lambda}\right)}$

For $r_i = \frac{R_i}{\pi a^2} \approx 380\ \mathrm{M\Omega\ \mu m^{-1}}$, and $r_m = \frac{R_m}{2\pi a} \approx 4471\ \mathrm{G\Omega\ \mu m}$ this gives a tether input resistance of $\sim 460\ G\Omega$. For a primary cilium with $a = 100\ \mu\mathrm{m}$ and $l = 5\ \mu\mathrm{m}$, this gives an input resistance of $\sim 490\ G\Omega$. Input resistance increases for shorter protrusions because membrane leak is lower.

Suppose that a narrow constriction or obstruction exists at the junction between the protrusion and cell body (e.g. the narrow neck of a dendritic spine or the selectivity filter of a primary cilium). We can treat the junction as a resistance in series with the protrusion input resistance. Then, the steady-state voltage "seen" by the protrusion is given by the voltage divider equation:

$$V_{div} = \frac{V_{x=0} R_j}{R_j + R_{in}} \quad \text{C5}$$

Where R_j is the junction resistance.

What happens to protrusion voltage in the absence of voltage clamp at the cell body? The prior section shows that tethers (also cilia, etc.) are typically short compared to their electrotonic length $l \ll \lambda$ such that:

$$R_{in} \approx \frac{\sqrt{r_i r_m}}{l/\lambda} = \frac{r_m}{l} = \frac{R_m}{2\pi a l}\ . \quad \text{C6}$$

We treat the tether as an isopotential compartment with a capacitance C_t, membrane leak resistance $R_t = R_{in}$ and reversal potential E_t connected to the cell body through tether axial resistance $R_a = \frac{R_i l}{\pi a^2}$. We also

model the cell body as an isopotential compartment with capacitance C_c, membrane leak resistance R_c and reversal potential E_c (**Figure C.1 A**).

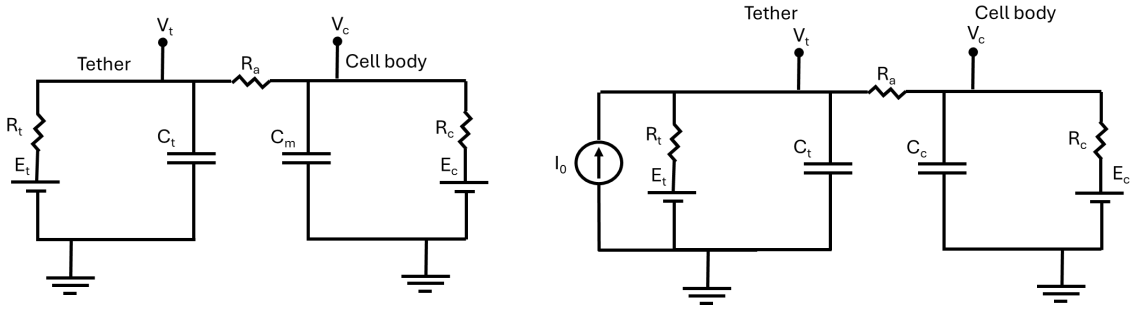

Figure C.1. Equivalent circuit of a cell and tether (**A)** without current injection into the tether and (**B**) with current injection.

Circuit analysis at steady-state yields the following relationships:

Current flow through the tether:

$$\frac{1}{R_t}(V_t - E_t) = \frac{1}{R_a}(V_c - V_t)$$

Current flow through the cell body:

$$\frac{1}{R_c}(V_c - E_c) = \frac{1}{R_a}(V_t - V_c)$$

Solving for the steady-state voltage difference between the tether and cell body yields:

$$V_t - V_c = \frac{R_a}{R_c+R_t+R_a}(E_t - E_c) \qquad \text{C7}$$

Including a constant current injected into the tether (**Figure C.1 B**) such that

$$\frac{1}{R_t}(V_t - E_t) + I_0 = \frac{1}{R_a}(V_c - V_t)$$

Yields the following expression for steady-state voltage difference between the tether and cell body.

$$V_t - V_c = \frac{R_a}{R_c+R_t+R_a}\big((E_t - E_c) + R_t I_0\big) \qquad \text{C8}$$

Eq. C8 shows that without a steady-state potential difference (first term) or constant current injection into the tether (second term), there will be no steady-state voltage difference. For $R_c \ll R_t$ and R_a, this reduces to:

$$V_t - V_c = \frac{R_a}{R_t+R_a}(E_t - E_c) + \frac{R_a R_t}{R_t+R_a} I_0 \qquad \text{C9}$$

Which shows that for $R_t \gg R_a$ the steady-state voltage difference due to $E_t - E_c \neq 0$ scales as the inverse of tether membrane resistance (i.e. in the limit of a very small area tether, $V_t - V_c \to 0$). In the large-area

limit, the compartment voltages do not equalize. Furthermore, if the injected current is nonzero, $I_0 \neq 0$ and $R_t \gg R_a, V_t - V_c \approx R_a I_0$.

These estimates suggest that a constant 0.2 pA current flowing through the tether would generate an ~1 mV steady-state voltage difference between compartments. These calculations help to illustrate the conditions under which protrusions cilia and spines might have different voltages than their parent compartment, that is for large axial resistances and steady-state protrusion currents and/or differing reversal potentials.